이학박사 학위논문

# Forward-Angle Exclusive $K^{*0}\Sigma^{+}$ Photoproduction from the Proton at $E_\gamma$ = 1.85 - 3.0 GeV

2012년 2월

부산대학교 대학원

물리학과

황상훈

이학박사 학위논문

# Forward-Angle Exclusive $K^{*0}\Sigma^+$ Photoproduction from the Proton at $E_\gamma$ = 1.85 - 3.0 GeV

지도교수 안 정 근

2012년 2월

부산대학교 대학원

물리학과

황 상 훈

# 황상훈의 이학박사 학위논문을 인준함

2011년 12월 일

| | | |
|---|---|---|
| 위원장 | Kenneth H. Hicks | (인) |
| 위원 | Takashi Nakano | (인) |
| 위원 | Wen-Chen Chang | (인) |
| 위원 | 오용석 | (인) |
| 위원 | 안정근 | (인) |

To My Family

# Forward-Angle Exclusive $K^{*0}\Sigma^{+}$ Photoproduction from the Proton at $E_\gamma$ = 1.85 - 3.0 GeV

Sanghoon Hwang

Department of Physics, Pusan National University, Korea

## Abstract

It is well known in the quark model of hadrons that mesons are found in groups of 8+1(an octet plus a singlet). For the lightest meson octet, 4 mesons are have no strange quark and 4 mesons contain either a strange quark or strange antiquark. However, for the higher-mass mesons, the assignments are not as clear. For example, the Particle Data Group(PDG) states that the identification of the scalar mesons is ”a long-standing puzzle”. In particular, the $\kappa$-meson with resonance pole at about 800 MeV is seen in many phenomenological analyses, yet its existence is still controversial.

Recently, the CLAS collaboration and CBELSA/TAPS collaboration reported the total cross section data and differential cross section data for $K^{*0}\Sigma^{+}$ photoproduction, and found that the $t$-channel exchange dominates the production amplitudes at small scattering angles. The available exchange particle are the scalar $\kappa$-meson, positive parity exchange, and the pseudoscalar kaon-meson, negative parity exchange. In the theoretical model supports that the parity spin asymmetry, given in terms of the spin density matrix elements by , is particularly sensitive to the role of $\kappa$-exchange, especially at forward angles. In the case of scalar $\kappa$ exchange, the parity spin asymmetry is positive, whereas calculations with only the pseudoscalar kaon has negative parity spin asymmetry.

The experiment done here measured the linear polarization observables for $K^{*0}$ photoproduction off the proton from threshold to 3 GeV at SPring-8/LEPS facility. We measured spin-density matrix elements at very forward angle and the present data provide the first-ever reported parity spin asymmetry for $K^{*0}$ photoproduction.

The parity spin asymmetry ($P_\sigma = 2\rho^1_{1-1} - \rho^1_{00}$) is estimated to be $0.784 \pm 0.154$ in the GJ frame and $0.758 \pm 0.123$ in the helicity frame. The large positive asymmetry shows that natural parity exchange is the dominant process at forward angles.

This supports that a natural-parity exchange is dominant in foward angles for $K^{*0}\Sigma^{+}$ photoproduction. A natural explanation for the natural-parity exchange would be $t$-channel of a scalar meson with strangeness, which is consistent with the $\kappa$ meson. The results of this experiment support the existence of this meson, which would complete the lowest-mass scalar meson octet.

# Contents

# Chapter 1

# Physics Motivation

Strange meson and baryon photoproduction is a very nice tool to study on the properties of strange hadrons and the structure of non-strange baryon state. $K^+$ photoproduction has been extensively studied in theoretically and experimentally [1, 2]. Recently, the strange vector meson, $K^*(892)$, photoproduction has been reported [3, 4, 6]. They reported the total and the differential cross sections which suggest that amplitude of $K^*$ photoproduction is smaller than $K^+$ photoproduction, but still sizeable.

## 1.1 Scalar meson in Quark Model

It is well known in the quark model of hadrons that mesons are found in groups of 8+1 (an octet plus a singlet). In the simplest quark model [7], the lightest meson octet has 3 mesons with no strange quark, 4 mesons containing either a strange quark ($s$) or a strange anti-quark ($\bar{s}$), and one meson with a dominant $s\bar{s}$ content as shown in Figure 1.1.

The ground-state pseudoscalar meson octet is well-established, and consists of three pions, four kaons, and an eta-meson. However, for the higher-mass mesons, the assignments are not as clear. For example, in Ref. [8] the Particle Data Group (PDG) states that the identification of the scalar mesons is ”a long-standing puzzle”. They are large decay widths which cause a strong overlap between resonances and background. And also, they decay several channels open up within a short mass interval. In additional, one theoretical expects non-q$\bar{q}$ state. Experimentally well established scalar resonances below 1 GeV are $a_0$(980) and $f_0$(980). Hence, the nature of the low-lying nonet scalar mesons is not understood yet.

The $\sigma$ meson has a width almost equal to its mass, and certainly cannot be described as a typical Breit-Wigner resonance. There is a strong experimental evidence for a light sigma meson, whose pole was extracted with a small uncertainty from modern analyses in $\pi$-$\pi$ scattering [9, 10]. The significant contributions of the sigma pole were identified in the D meson decay; $D^+ \rightarrow$

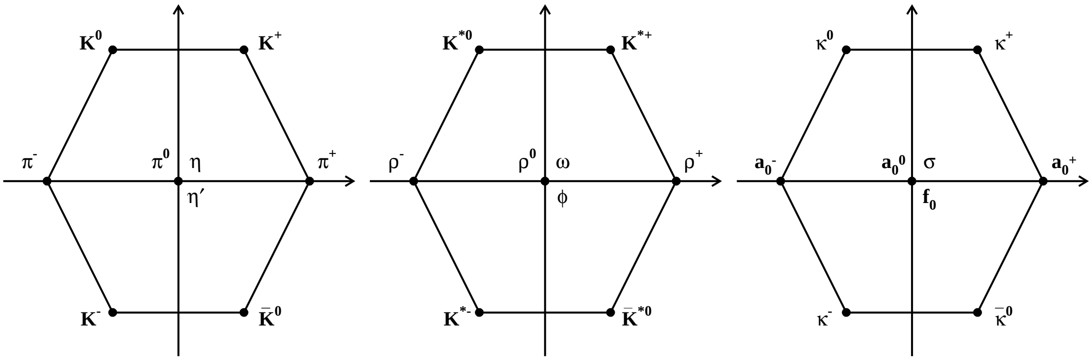

(a) pseudoscalar meson (b) vector meson (c) scalar meson

**Figure 1.1:** Three diagrams for $\gamma p \to K^{*0}\Sigma^+$ photoproduction, which include (a) $t$-channel exchanges, (b) $s$-channel $N^*\Delta$, (c) $u$-channel hyeprons and (d) contact diagrams.

$\pi^-\pi^+\pi^+$ [11] and $D^0 \to K^0_S\pi^+\pi^-$ [12]. The $\kappa$ is thought to be similar, actually worse than $\sigma$, with a pole mass of about 800 MeV and a width about half as big ($\sim 400$ MeV). The $\kappa$-meson (presumed to be part of the lowest-mass scalar meson octet) with a resonance pole at about 800 MeV, yet its existence is still controversial.

As mentioned above, the light scalar mesons are difficult to accommodate. The assignments for $J^{PC} = 0^{++}$ are filled by the higher-mass $a_0$(1450) and $f_0$(1370) plus $f_0$(1710) mesons, along with the $K^*$(1430). In contrast, the light scalar mesons, consisting of the $a_0$(980) and $f_0$(980) plus the $\sigma$ are thought to be meson-meson (or 4-quark) states [13, 14], and so are not included in the classical quark model picture. The $a_0$(980) and $f_0$(980) are firmly established, but their interpretation as exotic 4-quark states is still in question. More information on the structure of these scalar mesons is desired [15].

Definitive evidence for the $\sigma$ or $\kappa$ mesons would provide a significant advance in establishing the existence of multi-quark states.

## 1.2 $\kappa$(800) meson

The quantum numbers of the $\kappa$-meson are $J^P = 0^+$ and $I = 1/2$. The $\kappa$ is considered to be the scalar partner to the kaon in a similar way as the $\sigma$-meson (also called the $f_0$(600)) is the scalar partner to the $\eta$-meson. The difficulty to establish whether the $\sigma$ or the $\kappa$ mesons exist is, in part, because their resonance widths are very broad (about 400 MeV or even higher).

Table 1.1 was summarized of the $\kappa$ meson resonance parameters in the recent literature by Particle Data Group (PDG) [8]. The average value of $\kappa$ mass is 676 $\pm$ 40 MeV/$c^2$ and its width is 548 $\pm$ 24 MeV/$c^2$ by using top four results in the Table 1.1.

Evidence of the $\kappa$-meson has been shown in phenomenological analysis of $K\pi$ scattering phase shift data [29, 30, 31, 32], in the analysis of D meson decay; $D^+ \to K^-\pi^+\pi^-$ [19, 24, 21,

| Mass(MeV/$c^2$) | Width (MeV/$c^2$) | References | Reaction |
|---|---|---|---|
| $849 \pm 77\ ^{+18}_{-14}$ | $512 \pm 80\ ^{+92}_{-44}$ | M. Ablikim et al. (BES Collaboration), 2010 [16] | $J/\psi \to K^{\pm}K^0_S\pi^{\mp}\pi^0$ |
| $841 \pm 30\ ^{+81}_{-73}$ | $618 \pm 90\ ^{+96}_{-144}$ | M. Ablikim et al. (BES Collaboration), 2006 [17] | $J/\psi \to \bar{K}^{*0}K^+\pi^-$ |
| 658 ± 13 | 557 ± 24 | S. Descotes-Genon and B. Moussallam, 2008 [18] | $\pi K \to \pi K$ |
| 797 ± 19 ± 43 | 410 ± 43 ± 87 | E. M. Aitala et al. (Fermilab E791 Collaboration), 2002 [19] | $D^+ \to K^-\pi^+pi^+$ |
| 663 ± 8 ± 34 | 658 ± 10 ± 44 | D.V. Bugg, 2010 [20] | S-matrix pole |
| 706.0 ± 1.8 ± 22.8 | 638.8 ± 4.4 ± 40.4 | G. Bonvicini et al. (CELO Collaboration), 2008 [21] | $D^+ \to K^-\pi^+\pi^+$ |
| 856 ± 17 ± 13 | 464 ± 28 ± 22 | J. M. Link et al. (FOCUS Collaboration), 2007 [22] | $D^+ \to K^-\pi^+\pi^+$ |
| $750^{+30}_{-55}$ | 684 ± 120 | D.V. Bugg, 2006 [23] | |
| 855 ± 15 | 251 ± 48 | C. Cawlfield et al. (CELO Collaboration) 2006 [24] | $D \to K\pi\pi$ |
| 694 ± 53 | 606 ± 59 | Z. Y. Zhou and H. Q. Zheng, 2006 [25] | $Kp \to K^-\pi^+n$ |
| 753 ± 52 | 470 ± 66 | J. R. Pelaez, 2004 [26] | $K\pi \to K\pi$ |
| 594 ± 79 | 724 ± 332 | H. Q. Zheng et al., 2004 [32] | $K^-p \to K^-\pi^+n$ |
| 722 ± 60 ± 34 | 772 ± 100 | D.V. Bugg, 2003 [31] | $K^-p \to K^-\pi^+n$ |
| $905^{+65}_{-30}$ | $545\ ^{+235}_{-110}$ | S. Ishida et al., 1997 [27] | $K^-p \to K^-\pi^+n$ |

**Table 1.1:** The summary of present status for the $\kappa$ meson by PDG.

22], and also in the $J/\psi \to \bar{K}^{*0}K^+\pi^-$ [16] and $J/\psi \to K^{\pm}K^0_S\pi^{\mp}\pi^0$ [17]. However, no evidence for the $\kappa$ was found in $D^0 \to K^-\pi^+\pi^0$ [33], and also some theorists are not convinced by the evidence [34].Hence, they are difficult to see in partial wave analyses of meson scattering data. In the case of $D$-meson decay and $J/\psi$ decay, there is a need in the decay amplitude of $D^+ \to K^-\pi^+\pi^+$ and $J/\psi \to K^{\pm}K^0_S\pi^{\mp}\pi^0$ for an additional $K\pi$ resonance with the quantum numbers of the $\kappa$. However, additional evidence is needed before the $\kappa$ meson can be firmly established.

## 1.3 Photoproduction of $K^{*0}\Sigma$

We report on the linear polarization observables for $K^*$ photoproduction measured using a proton target. When a photon interacts with the proton an intermediate excited state of the proton can be produced and then decays, within a very short period of time, into final state of a kaon and a hyperon. The kind of the exchanged particle between the photon and the proton depends on the production mechanism of the final states. There are four possible mechanisms for the $K^{*0}$ production reaction: $t$-channel, $s$-channel, $u$-channel, and contact diagrams as shown in Fig. 1.2. The $t$ channel exchanged meson with strangeness and $s$ channel through $N^*$. The hyperons and hyperon resonances are exchanged in the $u$ channel.

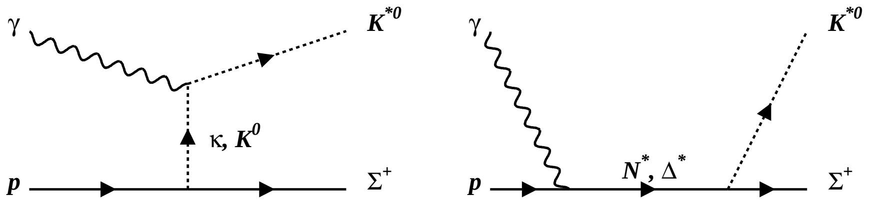

(a) $t$-channel (b) $s$-channel

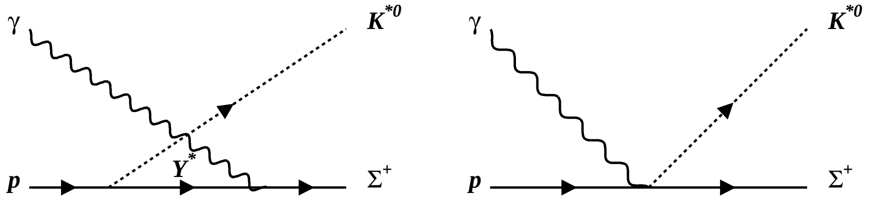

(c) $u$-channel (d) contact

**Figure 1.2:** Tree diagrams for $\gamma p \rightarrow K^{*0}\Sigma^+$ photoproduction, which include (a) $t$-channel exchanges, (b) $s$-channel $N^*\Delta$, (c) $u$-channel hyeprons and (d) contact diagrams.

The CLAS Collaboration at Thomas Jefferson National Accelerator Facility and the CBELSA/TAPS Collaboration at the 3.5 GeV electron stretcher facility ELSA reported the differential cross section data for $K^{*0}\Sigma^+$ photoproduction as a function of the center-of-mass angle $\theta_{K^{*0}}$ as shown in Figure 1.3 [5, 6]. They found a forward peaking that the $t$-channel exchange dominates the production amplitudes at small scattering angles. However, the backward angle production was described different. For the CLAS data, the curves are from the model of Zhao [36] using vector

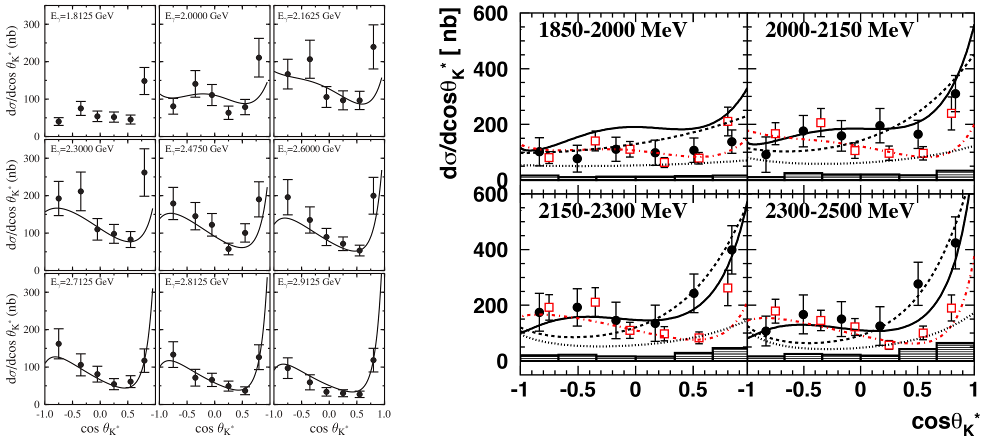

(a) CLAS Collaboration (b) CBELSA/TAPS

**Figure 1.3:** Differential cross section data for $\gamma p \rightarrow K^{*0}\Sigma^+$ photoproduction as a function of the center-of-mass angle $\theta_{K^{*0}}$ for the CLAS Collaboration(a) and the CBELSA/TAPS Collaboration(b, full circles).

and tensor couplings adjusted to give the best fit to the data. This model shows good agreement with the data, except at forward angles. The $t$-channel coupling in the Zhao model is completely determined by a single diagram with $K^0$ exchange. They suggested the role of scalar $\kappa$ meson exchanges should be investigated. The data from the TAPS Collaboration has been compared with the updated calculations from the model of Zhao(solid curves) [36, 37], the calculation in Ref. [38] model I(dotted curves) and model II(dashed curves), respectively. The dashed-dotted curve represents calculation in the model of Zhao [37] with free parameters. It is not yet possible to make an explicit conclusion about exchanged particle due to the significant contribution to the $K^0\pi^0\Sigma^+$ channel from the $\Sigma^{*+}$ production. They suggested that polarization experiments will be need to clarify exchange particles of the strangeness production process. Note that no polarization measurement for this reaction has been previously reported in the literature.

## 1.4 Theoretical model of the $K^{*0}\Sigma^{+}$

In general, $K^*$ photoproduction is different from other vector mesons in that Pomeron exchange is absent in the photoproduction of strange mesons. Hence, the reaction mechanism for $K^{*0}$ photoproduction is different from the case of the neutral nonstrange mesons ($\rho^0$, $\omega$ and $\phi$) where the $t$-channel has a strong contribution from Pomeron exchange. At low energies, meson exchange also contributes to the $t$-channel $\rho$ and $\omega$ photoproduction, but Pomeron exchange quickly becomes dominant as the photon energy increases.

For $K^{*0}$ photoproduction, the ambiguities in the theoretical modes at forward angles are rather limited. A single diagram dominates the $t$-channel, where a $K^0$ is exchanged and absorbs the photon through the $M1$ multipolarity. The hadronic coupling of the $K^0$ to the proton, $g_{KN\Sigma}$, is already constrained from kaon scattering data [35]. Exchange of a $K^{*0}$ in the $t$-channel is suppressed, since only higher (non-spin-flip) multipolarities can contribute to this diagram. Also, the contact term is proportional to the vector meson change, and vanishes for the neutral $K^{*0}$ production. However, a scalar meson can contribute to the $t$-channel for $K^{*0}$ photoproduction whereas it is forbidden by C-parity for kaon photoproduction.

The $K^{*0}\Sigma^+$ photoproduction has requared careful explain compare with $K^{*+}\Lambda$ photoproduction. The two preliminary results of CLAS Collaboration for $K^{*0}\Sigma^+$ and $K^{*+}\Lambda$ photoproduction show a very similar cross sections distribution at forward scattering angle [4]. In the Ref. [39], they have studied the $K^{*+}\Lambda$ photoproduction using CLAS data, and found that $t$-channel $K$ exchange dominates the production amplitudes at small scattering angles. However, by employing the $K$ exchange process for $K^{*0}\Sigma^+$ photoproduction, the predicts the cross section for $K^{*0}\Sigma^+$ would be smaller that $K^{*+}\Lambda$ photoproduction. The relative scattering amplitude determined from

$$\left(\frac{g^c_{K^*K\gamma}g_{KN\Lambda}}{\sqrt{2}g^c_{K^*K\gamma}g_{KN\Sigma}}\right)^2 \simeq 1.7^2,$$

where $\sqrt{2}$ is the isospin factor. We can expect to have other $t$-channel exchange, such as a scalar meson with strangeness which is consistent with the $\kappa$ meson, that contribute to $K^{*0}\Sigma^{+}$ photoproduction.

One theoretical model [38] predicted sizeable forward-angle polarization effects. In particular, Ref. [38] predicts that the $\kappa$(800) contributes to $K^{*}$ photoproduction through $t$-channel exchange, which dominates at forward scattering angles. Also, the contribution of the $\kappa$(800) for $K^{*0}\Sigma^{+}$ photoproduction is predicted to be relatively larger than that for $K^{*+}\Lambda$ photoproduction.

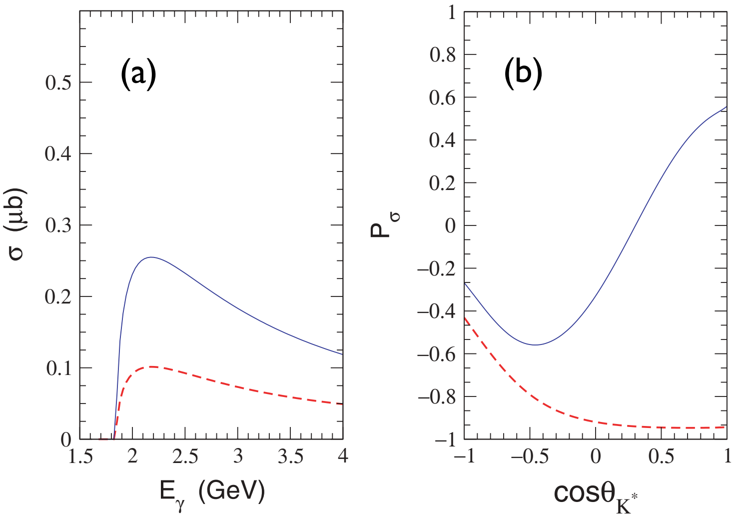

**Figure 1.4:** Total cross section (a) and parity spin asymmetry $P_\sigma$ (b) for $\gamma p \to K^{*0}\Sigma^{+}$ photoproduction. The dashed and solid lines are the results for the standard (no $\kappa$-exchange) model and the extended (with $\kappa$-exchange) model, respectively.

Figure 1.4 shows theoretical prediction of total cross section and parity spin asymmetry for $\gamma p \to K^{*0}\Sigma^{+}$ photoproduction. The dashed and solid lines are the results for the standard (no $\kappa$-exchange) model and the extended (with $\kappa$-exchange) model, respectively. The total cross section for $K^{*0}\Sigma^{+}$ shows a substantial difference between the standard model and extended model. However, the prediction required a precise measurement of the total cross section.

The parity spin asymmetry [40], given in terms of the spin density matrix elements by $P_\sigma = 2\rho^{1}_{1-1} - \rho^{1}_{00}$, have been shown to be particularly sensitive to $\kappa$-meson exchange, especially at forward angles. In the case of scalar $\kappa$ (natural parity) exchange, the parity spin asymmetry is positive, whereas calculations without the $\kappa$ (with pseudoscalar $K$ (unnatural parity) exchange only) have negative parity spin asymmetry. Note that no polarization measurement for this reaction has been previously reported in the literature. By comparing the data measured here with the standard (no $\kappa$-exchange) model and the extended (with $\kappa$-exchange) model, we can test for the existence of the $\kappa$(800).

## 1.5 Spin-density matrix elements

The decay angular distribution of the vector mesons is parameterized by the spin-density matrix elements and polarization of the photon beam energy [40]. For the common decay reaction from the vector meson, we can be explained the decay angular distribution by using 12 of spin-density matrix elements and the range of their values is not unlimited but restricted by a set of inequalities. In particular, its measurable values were limited for the various photon polarizations. With linearly polarized photons, 9 out of 12 measurable spin-density matrix can be separated in to contributions from natural and unnatural parity exchange in the $t$-channel. However, circularly polarized photons can not give any information on the natural or unnatural of the $t$-channel exchange. For the unpolarized photons, we only can measure the helicity conservation($\rho^0_{00}$).

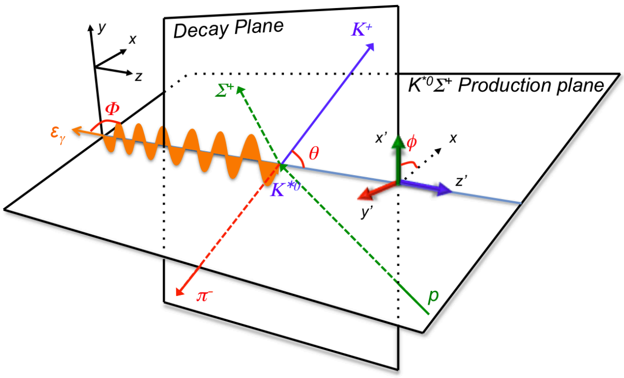

(a) Gottfried-Jackson frame

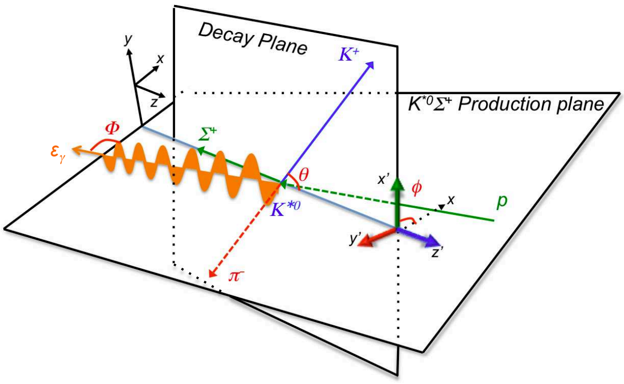

(b) helicity frame

**Figure 1.5:** Decay angles for the reaction $\gamma p \rightarrow K^{*0}\Sigma^+ \rightarrow K^+\pi^-\Sigma^+$ in the Gottfried-Jackson frame(a) and helicity frame(b). $x, y, z$ are the axes of the production plan in the $K^{*0}$ rest frame, and $x', y', z'$ are the axes of the decay plane. $\varepsilon_\gamma$ represents the direction of photon polarization.

Figure 1.5 shows two decay angle diagrams for the Gottfried Jackson(GJ) frame and helicity frame [42, 43, 44]. In the GJ-frame, production plane($x, y, z$) is defined as the plane on which momentum vectors of the incoming photon and produced $K^{*0}$ lie. $z-$axis is equal to photon beam direction. While, in the helicity frame, $z-$axis is equal to and a opposite to the outgoing $\Sigma^+$ and produced $K^{*0}$ directions, respectively. The $y-$axis is defined as a direction normal to the production plane, the $x-$axis is defined as a direction of outer product $\hat{y} \times \hat{z}$.

We defined $\theta, \phi, \Phi$ angles, such that $\theta$ and $\phi$ are the polar and the azimuthal angles between the $K^+$ and the $K^{*0}$ production planes in the $K^{*0}$ rest frame, respectively. $\Phi$ is the azimuthal angle between the photon polarization vector, $\varepsilon_\gamma$, and the $K^{*0}$ production plane in the center-of-mass of the $\gamma p \to K^{*0}\Sigma^+$ reaction.

The decay angular distribution with linear polarization are expressed as:

$$\begin{aligned}
W(\theta,\phi,\Phi;\hat{\rho}) &= W^0(\theta,\phi,\Phi;\hat{\rho}) - P_\gamma \cos(2\Phi) W^1(\theta,\phi,\Phi;\hat{\rho}) \\
&\quad - P_\gamma \sin(2\Phi) W^2(\theta,\phi,\Phi;\hat{\rho}) \\
W^0 &= \frac{3}{4\pi}(\frac{1}{2}(1-\rho^0_{00}) + (3\rho^0_{00}-1)\cos^2\theta \\
&\quad - \sqrt{2}\mathrm{Re}(\rho^0_{10})\sin(2\theta)\cos\phi - \rho^0_{1-1}\sin^2\theta\cos(2\phi)), \\
W^1 &= \frac{3}{4\pi}(\rho^1_{11}\sin^2\theta + \rho^1_{00}\cos^2\theta \\
&\quad - \sqrt{2}\mathrm{Re}(\rho^1_{10})\sin(2\theta)\cos\phi - \rho^1_{1-1}\sin^2\theta\cos(2\phi)), \\
W^2 &= \frac{3}{4\pi}(\sqrt{2}\mathrm{Im}(\rho^2_{10})\sin(2\theta)\sin\phi + \mathrm{Im}(\rho^2_{1-1})\sin^2\theta\sin(2\phi))
\end{aligned}$$

where, $P_\gamma$ is degree of linear polarization of the incident photon. The spin-density matrix elements, $\rho^i_{jk}$($i$ = 0,1,2), are bilinear combinations of scattering amplitude.

The above angular distribution contains three different angle variables. It can be rewritten as a distribution with only a single variable if it is integrated over the other two angles. The new forms of the decay angular distribution are as follows:

$$\begin{aligned}
W(\cos\theta) &= \frac{3}{2}(\frac{1}{2}(1-\rho^0_{00})\sin^2\theta + \rho^0_{00}\cos^2\theta) \\
W(\phi) &= \frac{1}{2\pi}(1 - 2\mathrm{Re}\rho^0_{1-1}\cos(2\phi)) \\
W(\phi-\Phi) &= \frac{1}{2\pi}(1 + P_\gamma(\rho^1_{1-1} - \mathrm{Im}\rho^2_{1-1})\cos 2(\phi-\Phi)) \\
W(\phi+\Phi) &= \frac{1}{2\pi}(1 + P_\gamma(\rho^1_{1-1} + \mathrm{Im}\rho^2_{1-1})\cos 2(\phi+\Phi)) \\
W(\Phi) &= \frac{1}{2\pi}(1 - P_\gamma(2\rho^1_{11} + \rho^1_{00})\cos(2\Phi))
\end{aligned}$$

In the case of helicity conservation, the decay asymmetry $\rho^1_{1-1}$ reflects the relative contributions of natural parity ($\rho^1_{1-1}$ = -0.5) and unnatural parity ($\rho^1_{1-1}$ = 0.5) processes. The parity spin asymmetry $P_\sigma$ in the contributions $\sigma^N$ and $\sigma^U$ are as follows:

$$P_\sigma = \frac{\sigma^N - \sigma^U}{\sigma^N + \sigma^U} = 2\rho^1_{1-1} - \rho^1_{00}$$

In this thesis, we report on the linear polarization observables for $K^*$ photoproduction measured using a proton target. Theses observables, parity spin asymmetry, have been shown to be sensitive to $\kappa$-meson exchange.

In Chapter 2, the SPring-8 and LEPS facility are described. Calibrations and data reduction are presented in Chapter 3. The absolute value of the spin-density matrix elements and the differential cross section are described in Chapter 4. Finally, we will conclude this work in Chapter 5.

## Chapter 2

# Experiment

Our experiment, $K^{*0}\Sigma^{+}$ photoproduction, has been carried out at the Laser-Electron-Photon beam line (LEPS) at Super Photon ring-8 GeV (SPring-8), the world's largest third-generation synchrotron radiation facility, in Japan. Figure 2.1 shows a bird's eye view of SPring-8. A linearly polarized photon beam was produced by the backward Compton scattering of the deep UV laser (257 nm) from 8 GeV electrons in the storage ring at SPring-8 BL33LEP beamline (LEPS facility). The LEPS facility consists of a laser injection system, tagger system for photon energy, a liquid hydrogen target and a charged particle spectrometer. In this chapter, we will discuss in detail the LEPS beam line and LEPS spectrometer which played key roles during the $K^{*0}$ experiment run.

**Figure 2.1:** A bird's eye view of SPring-8 taken on September 2011.

## 2.1 SPring-8

SPring-8 facility is a large synchrotron radiation facility which delivers the most powerful synchrotron radiation currently available. Consisting of narrow, powerful beams of electromagnetic radiation, synchrotron radiation is produced when electron beams, accelerated to nearly the speed of light, are forced to travel in a curved path by a magnetic field. The research conducted at SPring-8, located in Harima Science Park City, Hyogo Prefecture, Japan, includes nanotechnology, biotechnology and industrial applications. SPring-8 was opened in 1997 to industrial, academic and government users, domestic and international.

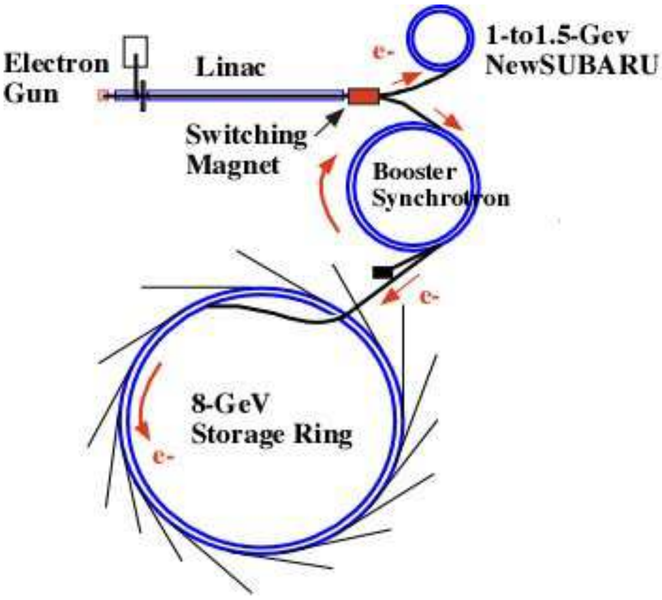

**Figure 2.2:** Schematic view of the accelerator complex of SPring-8.

Figure 2.2 shows the schematic view of the accelerator complex of SPring-8. The accelerator complex of SPring-8 is composed of an injector linac, a booster synchrotron, and a low-emittance and high-brightness storage ring. Electrons are generated at an electron gun and accelerated to an energy of 1 GeV in the injector linac with a length of 140 m. A 1 GeV electron beam is transported to the booster synchrotron with a 396 m circumference, and accelerated up to 8 GeV. The 8 GeV electron beam is injected from the synchrotron into the storage ring with a 1436 m circumference and stored.

Electrons with an energy of 8 GeV circulated in the storage ring. The time interval of the successive bunches for electrons in 1.966 nsec. Electrons are filled in some bunches with various filling patterns. The maximum current is 100 mA and top-up operation allows SPring-8 provide highly stable X-ray beam with arbitrary filling patterns.

The stored electron beam is used to generate synchrotron radiation photons at bending magnets, undulators and wigglers. The radiation photons are provided to various beam lines with the experimental hutches in the experimental hall. The photons with a high-brightness and low emittance are commonly used mainly for researches in material and life sciences. There are 57 beam line ,53 lines are used, and 4 lines are under construction. One of the beam lines calles BL33LEP is used by the LEPS group. In the LEPS beam line, the high energy photon beam produced by the backward-Compton-Scattering process in used in the experiments for photo-nuclear and nucleon reactions instead of of radiation photons.

## 2.2 LEPS beam line

Leaser-Electron-Photon facility at SPring-8 (LEPS) produced GeV photon beams by the backward Compton scattering of ultraviolet laser photons off 8 GeV electrons circulating in the SPring-8 synchrotron radiation ring. The beams are used for nuclear and hadron physics experiments by international collaborations. The first LEPS beam was produced in 1999 and the first physics run started in 2000. A multi-GeV photon beam is produced by the backward-Compton-scattering process of laser photons from the circulating 8 GeV electrons at the LEPS beam line.

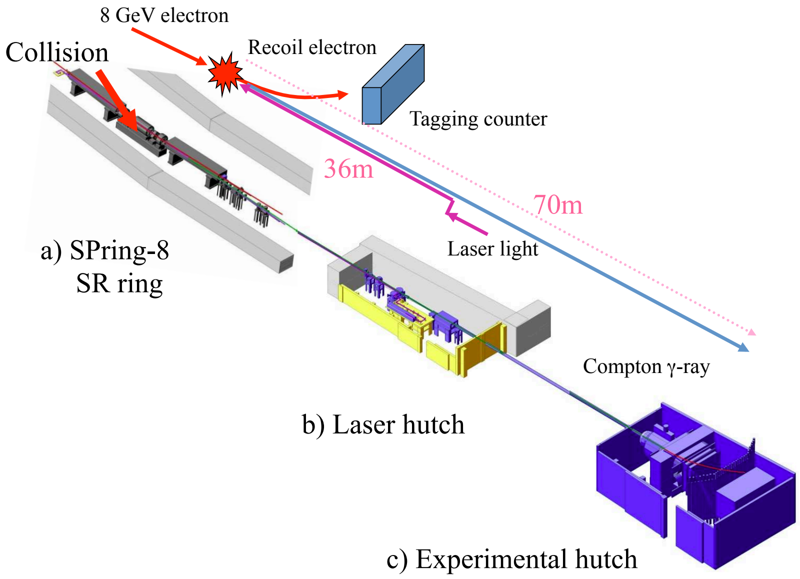

**Figure 2.3:** Schematic view of LEPS beam line at SPring-8. LEPS beam line consisted three parts; (a) Laser-electron collision part in the storage ring, (b) Laser hutch for laser injection, and (c) Experimental hutch where a spectrometer is placed.

LEPS beam line consisted three parts as shown in Figure 2.3; (a) Laser-electron collision part in the storage ring, (b) Laser hutch for laser injection, and (c) Experimental hutch where a spectrometer is placed. In this section, we will discuss about beam line system.

### Backward-Compton scattering photon beam

We have a multi-GeV linear polarized photon beam for Backward-Compton scattering (BCS). A Compton scattering of photons by electrons is an one of the most simple process in quantum electrodynamic. In 1963, Milburn and Tumanian pointed out that high energy polarized photons are produced by collisions of polarized laser photons with relativistic electrons. This process is generally called as Backward Compton scattering. Figure 2.4 shows the kinematical values of the BCS process in the laboratory frame. , where $E_e$ is the incident electron energy, $K_1$ is the laser photon energy, $E_\gamma$ is the energy of a scattered photon. $\theta_1(\theta_2)$ is the polar angle between incident electron direction and laser photon (outgoing scattered photon) direction. A laser photon interects with an electron with $\theta_1 \simeq 180°$. In the case of $E_e \gg k_1$, the scattered photon is headed out strongly in backward direction for the Lorentz boost. The energy of a scattered photon, $E_\gamma$, is written follow:

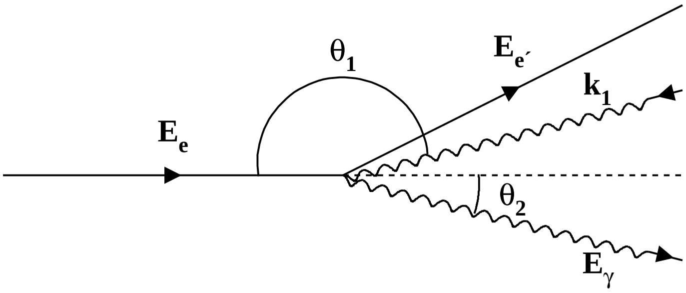

**Figure 2.4:** Kinematical values of the backward-Compton scattering process in the laboratory frame.

$$E_\gamma = k_1 \frac{1-\beta\cos\theta_1}{1-\beta\cos\theta_2 + \frac{k_1(1-\cos(\theta_2-\theta_1))}{E_e}},$$

where $E_e$ (7.975 ± 0.003 GeV [46]), is electron energy, $\beta$ is an incident electron velocity in unit of the speed of light. By assuming $\gamma = E_e/m_e \gg 1$, $\beta \simeq 1$, $\theta_1 \simeq 180°$ and $\theta_2 \simeq 0°$, a term in the denominator, $\beta\cos\theta_2$, can be evaluated $\beta\cos\theta_2 \simeq (1-\frac{1}{2}\gamma^{-2})(1-\frac{1}{2}\theta_2^2)$. Then, we can re-write above equation as follow:

$$E_\gamma \cong \frac{4E_e^2 k_1}{m_e^2 + 4E_e k_1 + \theta_2^2 E_e^2},$$

where $m_e$ (0.511 MeV) is the mass of the electrons in the storage ring. The maximum photon energy is obtained at $\theta_2 = 0°$ as follow:

$$E_\gamma^{max} \cong \frac{4E_e^2 k_1}{m_e^2 + 4E_e k_1}.$$

The maximum photon energy for the 257 nm deep UV laser is 2.96 GeV.

The linearly polarized BCS photons produced by linear polarized laser photons. The degree of polarization ($P_\gamma$) of a BCS photon is given by

$$\begin{aligned} P_\gamma &= P_{Laser}\frac{(1-\cos\alpha)^2}{2(\chi+1+\cos^2\alpha)} \\ \chi &= \frac{\rho^2(1-a)^2}{1-\rho(1-a)} \\ \cos\alpha &= \frac{1-\rho(1+a)}{1-\rho(1-a)}, \end{aligned}$$

where $P_{Laser}$ is a degree of polarization of an incident laser light which is almost 100% polarized. $\rho$ is a photon energy ratio of a maximum photon energy ($\rho = \frac{E_\gamma}{E_\gamma^{max}}$) and $a$ is $\frac{m_e^2}{m_e^2+4E_e k_1}$.

Figure 2.5 shows a degree of polarization as a function of the produced BCS photon with different laser system. The maximum polarization is 90% (94%) for deep UV laser (Ar laser), respectively. In this experiment, deep UV laser was used to produce a high energy BCS photon.

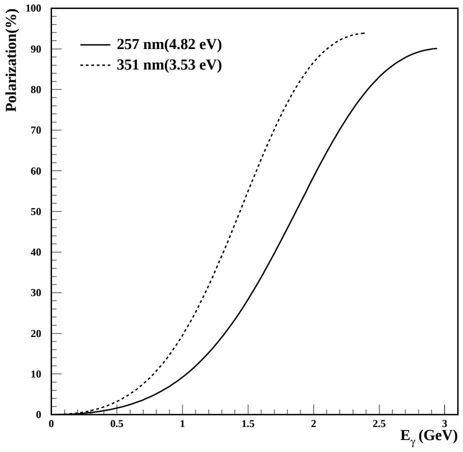

**Figure 2.5:** Polarization of the BCS photon as a function of produced photon, $E_\gamma$ when the laser photon is 100% polarized for Ar laser and deep UV laser, respectively.

### Deep UV laser

The deep UV laser (257 nm, $k_{laser}$ = 4.82 eV), which is 'Sabre MotoFreD' produced by COHERENT[47], was operated in the experiment to get high energy photon beam. A 20 W Ar laser pumped up the UV output of 1.0 - 1.5 W. The spot of the BBO crystal from which UV light was emitted was damaged in several days at the maximum power, and the crystal was mechanically shifted to different positions. The maximum laser power was maintained with the power tracking system. At the operating the laser system, dry nitrogen flowed in the laser system because of the hygroscopic nature of the BBO frequency bubbling crystal.

### Laser optics

The polarization of laser photons is controlled by a half-wave-length ($\lambda/2$) plate for changing the direction from vertical to horizontal. Figure 2.6 shows schematic view of the laser optics system. The $\lambda/2$ plate is located after the Deep UV laser for linearly polarized photon beam.

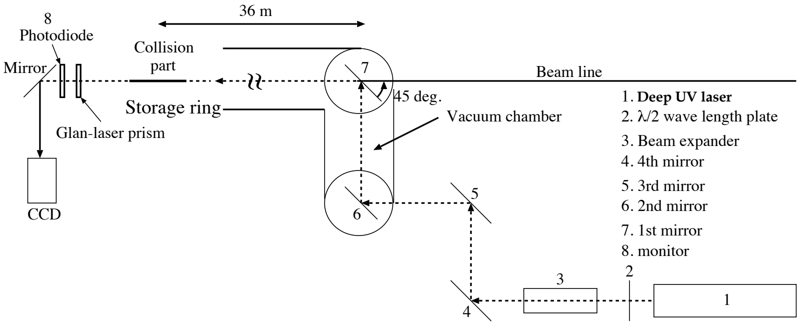

**Figure 2.6:** Schematic view of the laser optics system.

Four optical mirrors were used to guide the laser to the storage ring. At the end of the straight section, we put the polarization measuring system. The laser polarization was decided by a angle of the $\lambda/2$ plate. For the horizontally polarized laser, the direction of $\lambda/2$ plate set horizontal, on the other hand vertical polarization was got by rotating the $\lambda/2$ plate. The polarized laser size was enlarged by a expander, produced by SURUGA, which consisted of a coupled of optical lens to focus at the straight section of the storage ring where the electron beam circulated. We measured the polarization direction (angle) and degree by polarization measuring system at the end of the straight section in the storage ring, which consisted with a Glan-laser prism and photodiode. The Glan-laser prism was rotated and the intensity of the laser was measured behind the prism with a photodiode as a function of rotation angle of the polarizer. Figure 2.7 shows intensitiy distribution of the laser at the photodiode for vertically polarized laser (a) and horizonally polarized laser (b). Normally, the direction of polarization was changed 2 times in a day.

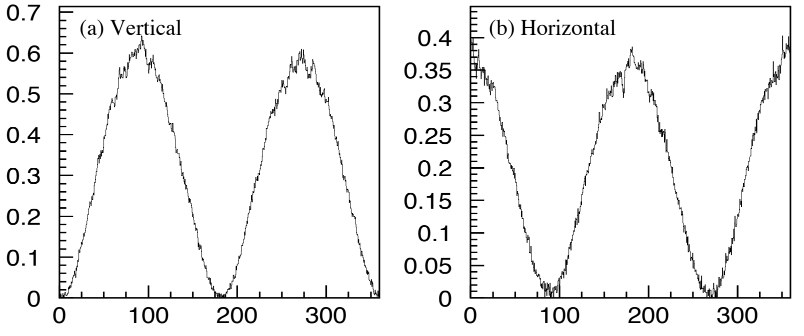

**Figure 2.7:** Intensity distribution of the laser at the photodiode for vertically polarizzed laser (a) and horizontally polarized laser (b).

### Tagger

The energy of photons was determined by measuring the energy of the recoiled electron energy, $E_{e'}$, for the Backward-Compton scattering. The energy conservation of the electron and photon leads the energy of photons as $E_\gamma = E_e - E_{e'}$, where $E_e$ is the electron energy of circulated in the storage ring, $E_\gamma$ is the produced photon beam energy. The recoiled electrons were detected with the tagging counter which was installed at the downstream of the bending magnet in the storage ring. The recoiled electrons passed through the bending magnet which bent the recoiled electron trajectory. The trajectory of the recolied electrons is strongly bent from the 8 GeV electron.

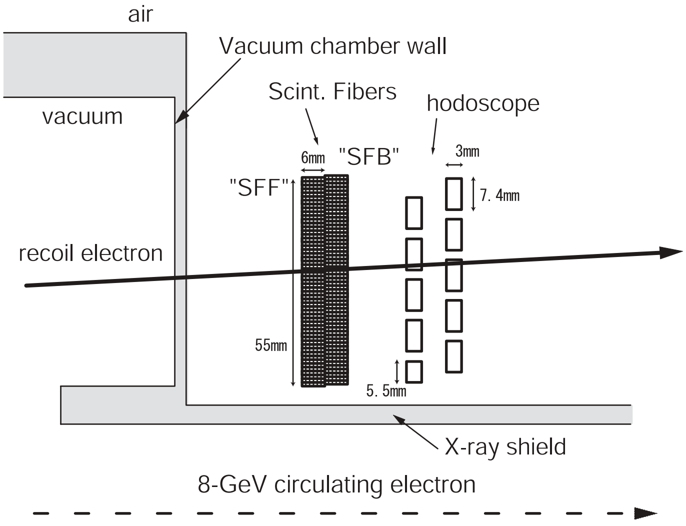

**Figure 2.8:** Schematic view of the tagger counter.

Figure 2.8 shows schematic view of the tagger counter. Tagger counter is placed at the outside of the vacuum chamber for the 8 GeV electron circulating. Tagger counter consisted of the plastic scintillator hodoscope and the two layers of scintillating fiber detectors. The plastic scintillator hodoscope consists of 5 segments with 2 layers plastic scintillator counters, which is 3.0 mm thick plastic scintillator with 10 mm high and 7.4 mm wide. At the closed part of the storage ring, we used the width of the scintillator 5.5 mm. Each scintillator is overlapped with adjacent bars by 2.7 mm. The fiber detectors was placed upstream of the plastic scintillator hodoscope, and consisted the front fiber (xsf fiber) and rear fiber (xsb fiber) layers with 55 fiber bundles. The fiber bundles were assembled six scintillating fibers with $1 \times 1$ mm$^2$ size. The front fiber and rear fiber provided a position information for the recoiled electron trajectory, which provided a timing signal of the recoiled electron signal by PMT read out. The measurable energy region corresponds to the range of 1.5 - 3.5 GeV for the $\gamma$-ray photons.

### Target

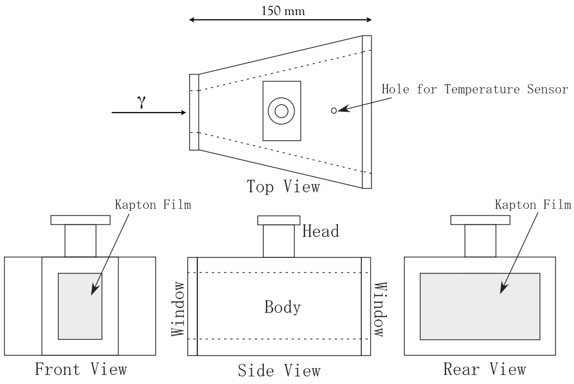

**Figure 2.9:** Schematic view of the liquid hydrogen target.

A 150 mm liquid hydrogen target was used in this experiment. Figure 2.9 shows schematic view of the target system. The target cell was made of copper with a thickness of 8 mm. The entrance and exit windows of the target cell were made of Alamid films with a thickness of 0.125 mm. The temperature and pressure of the target was kept at ?? $\sim$ 20.5 K and 1.0 $\sim$ 1.05 atm. The target was located at the 953 mm upstream of the center of the dipole magnet, dipole magnet will be discussed in next Section.

## 2.3 LEPS spectrometer

The LEPS spectrometer consisted of upstream veto counter, start count, vertex detector, dipole magnet, three drift chambers, downstream $e^+e^-$ veto counter and time-of-flight (TOF) wall. The schematic view of the LEPS spectrometer was shown in Figures 2.10 and 2.11.

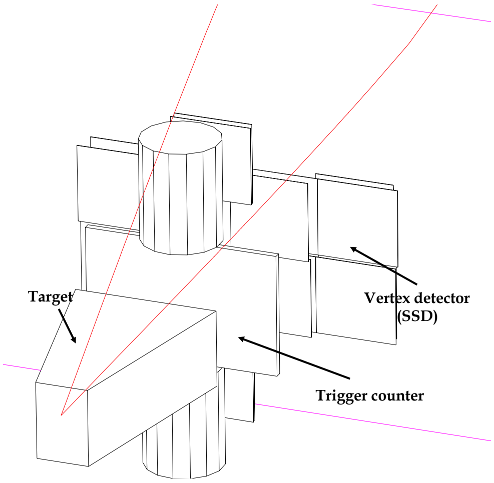

**Figure 2.10:** Schematic view of the LEPS spectrometer at the target parts.

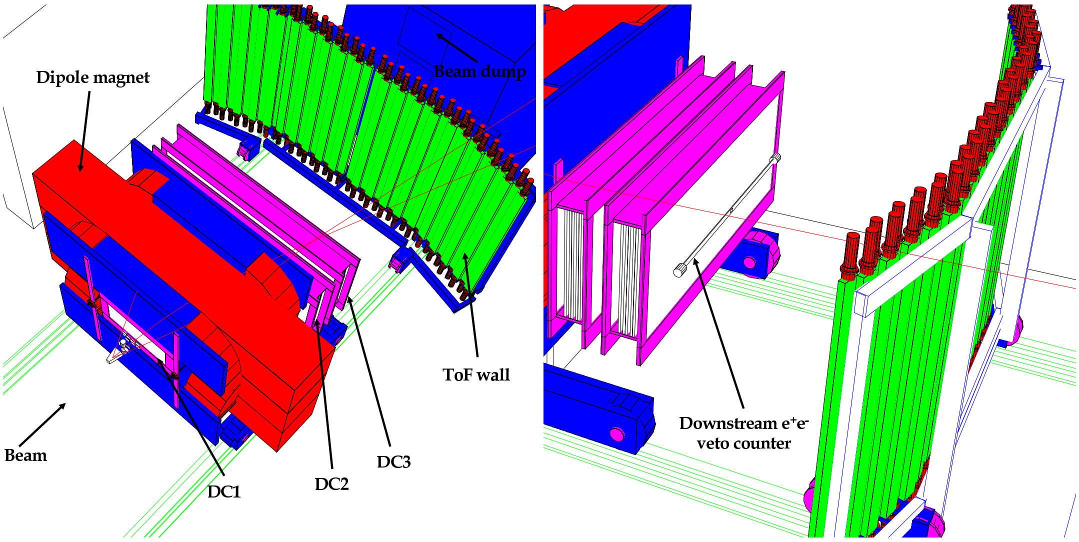

(a) Front-top view (b) Rear-top view

**Figure 2.11:** Schematic view of the LEPS spectrometer for front view (a) and rear view (b).

### Upstream veto counter

At the end of the beam pipe in the experimental hutch, we used upstream veto counter (UPveto) to eliminate the $e^+e^-$ background events, which size is 5 × 200 × 190 mm$^3$ made by plastic sciltillator.

### Trigger counter

A Photon beam injected to 150 mm liquid hydrogen target and produced particles by photoproduction. The charged particles from the target were measured using the trigger counter (TRG). The TRG provided a start timing of the trigger of data tacking, which is 5 mm thick plastic scintillator with 95 mm high and 150 mm wide. The TRG was located at the -801.6 mm upstream of the center of the dipol magnet.

### Vertex detector

The vertex silicon strip detector (SVTX) was used the vertex detector to measuring very precise position for an interaction point. The charged particle passed through the silicon and deposits ionization energy and liberate electrons. The electrons and holes by the ionization energy were separated due to the electric field inside the silicon strip detector (SSD). SSD collects at the electrode, giving a signal proportional to the deposited ionization energy. The SVTX consists of x and y plans of whth a thickness of 300 $\mu$m and 120 $\mu$m pitch. The SVTX was located -681.1 mm at the upstream of the center of the dipol magnet.

### Dipole magnet and $e^+e^-$ blocker

The dipole magnet provided the magnetic field for momentum analysis. Aperture of the dipole magnet was 550 mm high and 1350 mm wide. The length of the pole along the photon beam was 600 mm. The maximum field strength was 0.7 T at center of the dipole magnet. A current provided to the magnet was 800 A. A magnet field map was calculated by using OPERA-3D TOSCA package which provided the 3-dimensional magnetic field distribution. Figure 2.12 shows the strength of the y-direction magnetic field, $B_y$, as a function of z-position at x = 0 mm and y = 0 mm. Results of the calculation by TOSCA agree well with the measurements by hole probes. Inside of the magnet, a pair of $e^+e^-$ blocker (EBAR) with 100 mm thick, 40 mm high and 440 mm wide were installed in the horizontal plane at the 200 mm downstream of the center of the dipole magnet in order to block the $e^+e^-$ pair production from upstream. The gap distance between two $e^+e^-$ blocker is 155 mm, it is can be trough the gap for the above 1 GeV/$c$ momentum of $e^+e^-$ particles.

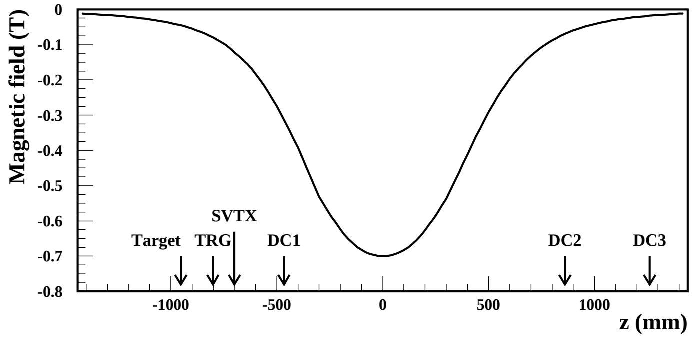

**Figure 2.12:** The distribution of the y direction magnetic field, $B_y$, as a function of z-position at x = 0 mm and y = 0 mm.

### Drift chambers

We used three multi-wire drift chambers (DC1, DC2 and DC3) for the charged particle tracking. DC1 was located at the upstream of the dipole magnet and DC2 and DC3 were located at the downstream of the dipole magnet.

Figure 2.13 shows the schematic drawing of field, shield and sense wires configuration in the multi-wire drift chambers. The DC1 consists of 6 planes which are x, x’, u, u’, v, x”. Planes for x, x’ and x” were lain 0°. The planes for u and u’ were inclined by 45° and direction of the plane for v was 135°. The wire spacing of sense wires was 6 mm for x, x’, u and u plane and 12 mm for v and x” planes. The active area for DC1 was 600 $\times$ 300 mm$^2$ which is located at -466.0 mm. The DC2 and DC3 have same design. They have 5 planes for x, x’, u, u’ and v. The direction for x and x’ planes lay 0°, u and u’ planes are 120° and v planes inclines 60°. The wire spacing of sense wires was 10 mm for x, x’, u and u’ plane and 20 mm for v plane. They have the active area of 2000 $\times$ 800 mm$^2$. DC2 and DC3 were placed at +860.5 mm and +1260.5 mm, respectively.

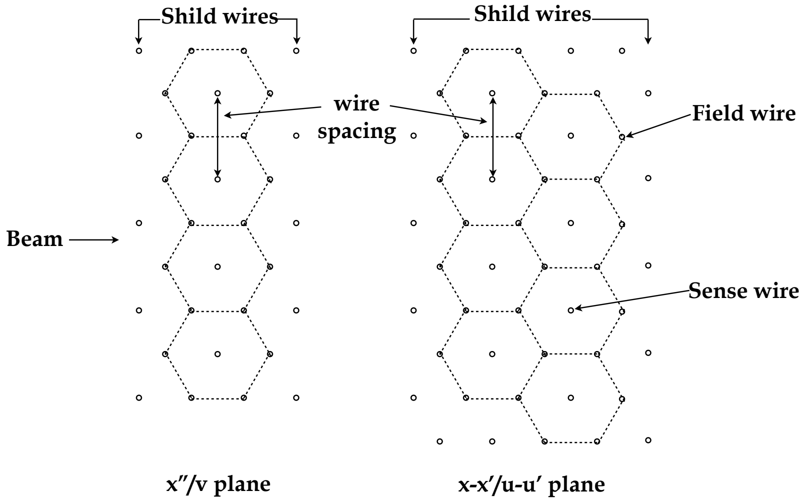

**Figure 2.13:** Schematic drawing of wires configuration in the multi-wire drift chambers.

The gas was mixed with 70 % argon and % 30 isobutane. Typical resolution is 200 $\mu$m and the efficiency is 97 $\sim$ 100 %.

### Downstream $e^+e^-$ veto counter

For the this experiment, we newly set up downstream $e^+e^-$ veto counter (EEveto) downstream of the DC3.

EEveto was performed the rejection of $e^+e^-$ background instead of Cherenkov detector, Cherenkov detector was used a standard run. Figure 2.14 shows schematic view of the downstream $e^+e^-$ veto counter. The detector fabricated a 20 mm thick plastic scintillator with 40 mm high and 185 mm wide. In the center of the EEveto, we made hole, the size is 20 mm high and 50 mm wide, for the photon beam.

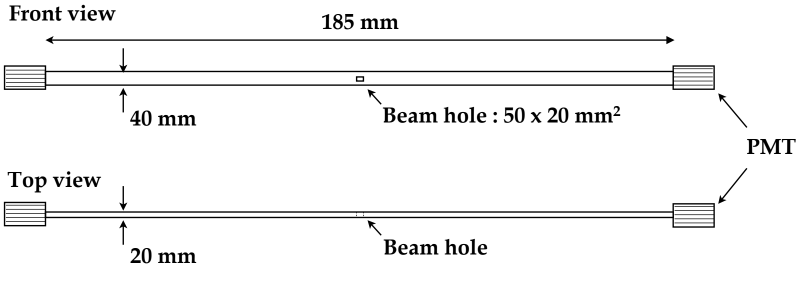

**Figure 2.14:** Schematic view of the downstream $e^+e^-$ veto counter.

### Time-of-flight wall

Time-of-flight of charged particle was measured by using the RF signal of the accelerator and the time-of-flight (TOF) wall. The start signal was given by TRG signal or RF signal, hence we used the TOF wall to give us a stop signal. Figure 2.15 shows the schematic view of the TOF wall.

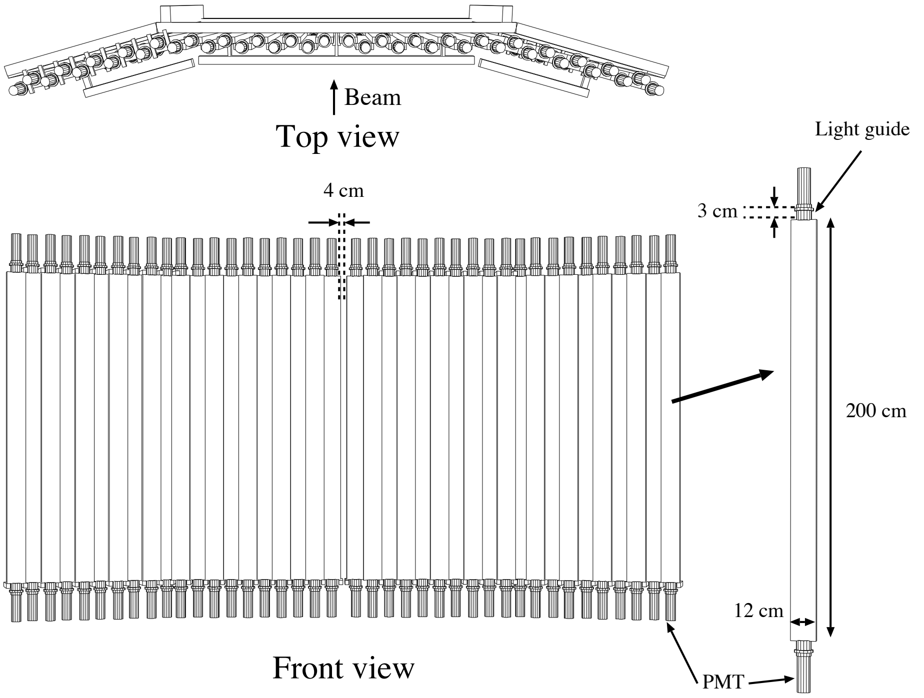

**Figure 2.15:** Schematic view of the TOF wall.

The size of a plastic scintillator bar (TOF bar) is $2000 \times 120 \times 40$ mm$^3$. The TOF wall consisted 40 slats, 20 TOF bars are left side and 20 TOF bars are right side. Each TOF bar is overlapped with adjacent bars by 10 mm. The both side of twelve flank bars were tilted by $\pm 15°$. In the middle of the TOF wall has 40 mm gap for beam hole which photon beam pass through. The TOF wall was placed at 3151.5 mm from the center of the dipole magnet.

### RF signal

We used RF signal from the 8 GeV storage ring to determine a start timing for the time-of-flight. The frequency of RF signal is 508 MHz which a time interval of the bunches of the electrons is 1.966 nsec.

## 2.4 Trigger

The trigger for the data taking consisted of a tagger signal (TAG), a signal from UPveto, a signal from TRG, a signal from EEveto and a signal from TOF. Diagram of the readout logic for trigger was shown in Figure 2.16. Data were taken with hadron trigger, which was defined as following :

$$(TAG \otimes \overline{UPveto}) \otimes (TRG \otimes \overline{EEveto}) \otimes TOF$$

Typical trigger rate for the $K^*$ experiment is 100 cps.

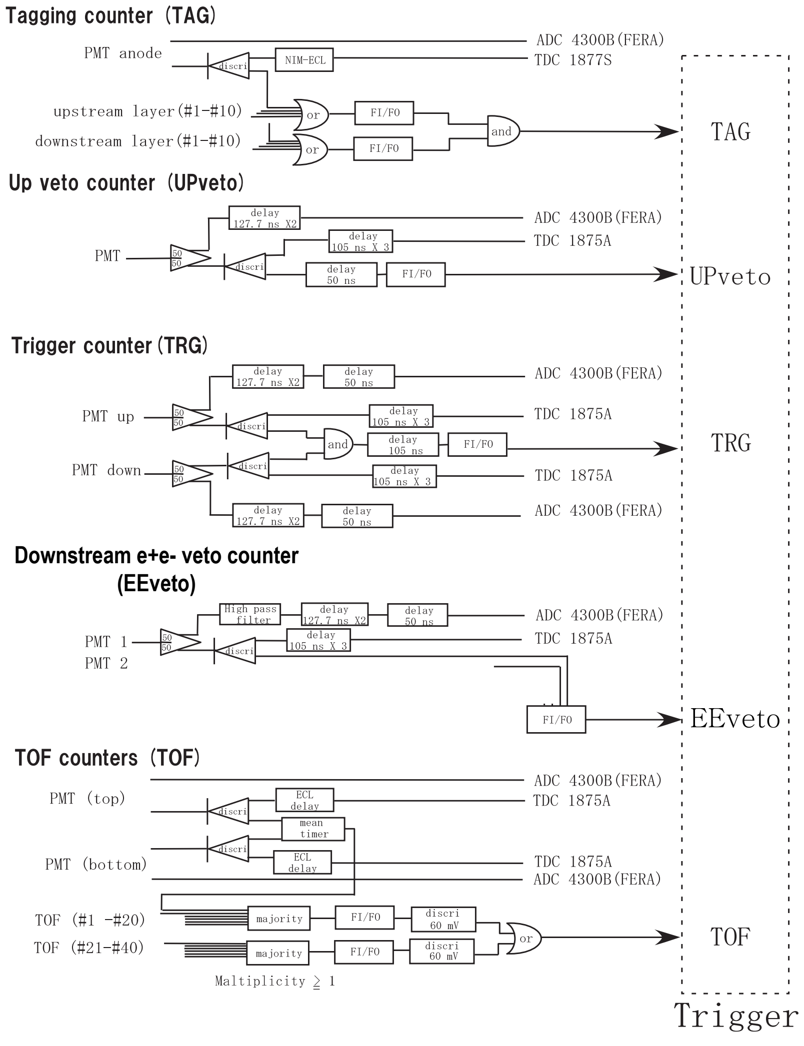

**Figure 2.16:** Diagram of the read out logic.

## 2.5 Run summary

We have taken a total of 485 M online triggers for $K^*$ photoproduction in the from October 6 to 18 and November 8 to December 17, 2007.

The number of physics runs is 488 out of a total of 547 runs. Electron filling patterns were changed during the $K^*$ runs, as listed in Table 2.1.

| Run number | Filling pattern |
|---|---|
| r37768 − r37808 | 4/58-filling+53 bunches |
| r37809 − r37912 | 160 bunch-train × 12 |
| r37922 − r38022 | 1/14-filling + 12 bunches |
| r38023 − r38068 | 160 bunch-train × 12 |
| r38069 − r38314 | 203 bunches |

**Table 2.1:** Electron filling patterns with run numbers

The total number of photons integrating the full energy range is $4.048 \times 10^{11}$, horizontal polarization is $2.038 \times 10^{11}$ and vertical polarization is $2.010 \times 10^{11}$, respectively.[53].

# Chapter 3

# Calibration and Data Reduction

The reconstruction of physical quantities from the various detector system were used off-line analysis program, which is called LEPSana. This is developed by the LEPS collaboration. During data reconstruction, each detector system(TOF, drift chamber, and tagger counter) was calibrated. This chapter deals with a calibration of each detector system and data reduction.

## 3.1 DC calibration

The momentum of charged particles were reconstructed from SVTX, DC1, DC2, and DC3/TOF wall. To get a hit position of three drift chamber, we have calibrated $T_0$ calibration and x-t curve calibration.

We collected the edge timings of signals for each wire of the drift chamgers, and each recorded timing has a flag whether it is leading or trailing. A drift time $t_{drift}$ is determined from a difference between a timing offset $T_0$ and a timing of an leading edge as given by

$$t_{drift} = -(T - T_0) \times 0.5\mathrm{nsec/channel}.$$

At the charged particle passed trough very close region, the signal was distributed right edge of the timing $T$ distribution. $T_0$ is determined by fitting the right edge of the timing $T$ distribution with a Gaussian convoluted step function since the charged particles come with a uniform distribution in a local region. Figure 3.1 shows $T$ distributions and an overlaid fit line shows Gaussian convoluted step function at $T_0$.

The drift length was evaluated from the drift time and parameters ($c_1$, $c_2$, and $c_3$) for x-t curve as given by

$$x_{drift} = c_1 t_{drift} + c_2 t_{drift}^2 + c_3 t_{drift}^3.$$

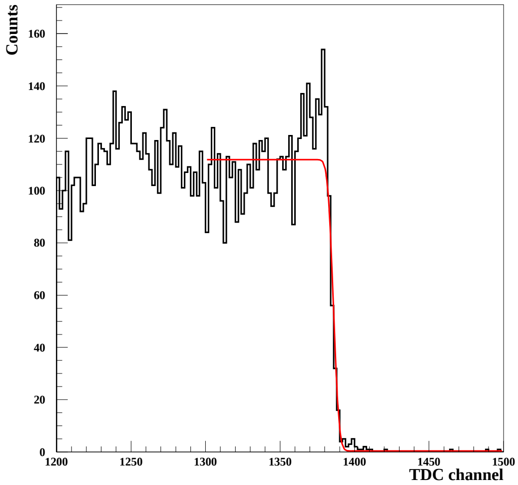

**Figure 3.1:** The timing distribution for DC1X 16 wire. $T_0$ is determined by fit with a Gaussian convoluted stpe function.

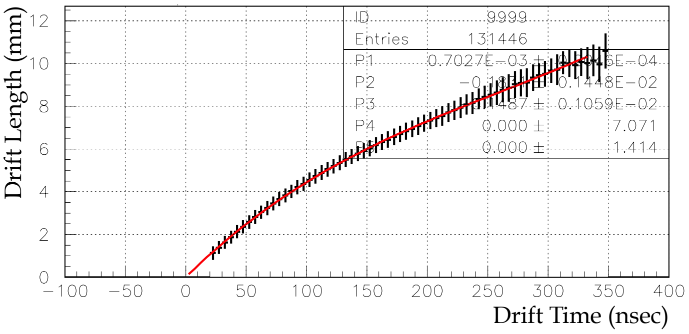

**Figure 3.2:** Relation between the drift length and the drift time for a DC1X plane. The line indicates x-t curve fit.

Figure 3.2 shows a sample of x-t curve fit for DC1X plane. The parameters for x-t curve are determined by each plane. Table 3.1 shows the resolution of the residual from x-t curve.

| Plane | x | x’ | u | u’ | v | x” |
|---|---|---|---|---|---|---|
| DC1 | 0.207 mm | 0.208 mm | 0.233 mm | 0.224 mm | 0.265 mm | 0.219 mm |
| DC2 | 0.205 mm | 0.198 mm | 0.186 mm | 0.279 mm | 0.262 mm | |
| DC3 | 0.229 mm | 0.223 mm | 0.214 mm | 0.269 mm | 0.255 mm | |

**Table 3.1:** Resolution of Drift chamber

A trajectory of a charged particle is determined by hit positions at the SVTX, three drift chambers(DC1, DC2, and DC3), and the TOF wall. Normally, we used DC3 hit information, however the DC3 didn't cover all detecting area. In the case of there is no hit in the DC3, we use a hit information from TOF wall instead of DC3. We used four step of the tracking analysis to obtain the momentum vector, sign of the change, the path length and vertex point.

First, we searched the clusters in the SVTX, DC1, DC2, and DC3. A cluster in the SVTX is made by comparision of a hit position in the $x$ layer and $y$ layer. DC1 consisted with six planes and the cluster required a hit more then 4 wires. And also each plane of DC1 required more than one hit. DC2 and DC3 have 5 five planes and the cluster is made by combining more than three wires in the DC2 and DC3. DC2 and DC3 required one hit in each plane. Each cluster in DC's does not include more than two hits in the same plane.

Second, straight line fit in a three dimensional space is performed upstream of the dipole magnet (SVTX and DC1) and downstream of the dipole magnet (DC2 and DC3/TOF). DC's only gives a information about distance from the wires, and has an ambiguity for the changed particle passed to right or left side of the wires. This ambiguity can be solved the straigh line fit from upstream and downstream. However, the low momentum particles can not solve correctly due to the track of low momentum particles is not straight line. Therefore, the right-left ambugity is not solved correctly, these hits are removed as outliers in the track fitting with the Kalman filter method [51].

Third, initial values for the Kalman filter method are determined. The best 30 combinations of clusters are selected in each stream in terms of $\chi^2$. Then, the consistency of the upstream and downstream checks with track cross in x-z plane in center region, and that the slope in y-z plane are not big different between the upstream and downstream tracks. In this step, we can obtaine not only initial values of the positions x, y and directions dx/dz, dy/dz at the first polane in the SVTX are obtained from the upstream straight line fit, but also initial values of the momentum vector and sign of the charge are estimated by the bending radius at the cross point of the upstream and downstream tracks.

Finally, a trajectory of a charged particle is reconstructed by applying the Kalman filter method that performs a least square fit to the measured hit positions including the effect of multiple scattering and energy loss. Now, we obtaine the sign of the charge, the absolute momentum, the momentum vector, the path length from the target to TOF wall, and vertex points from tracking analysis. And also, we obtaine goodness of a fit from the Kalman filter. The $\chi^2$ probability is defined as below,

$$prob(\chi^2, ndf) = \int_{\chi^2}^{\infty} f(\chi'^2, ndf) d\chi'^2$$

where $f$ is the standard $\chi^2$ distribution with number of degree of freedom $ndf$. In the case of a charged particle decays to douther particle, then the $\chi^2$ has a large value along with a small $\chi^2$ probability.

## 3.2 TOF calibration

The Time-of-Flight(TOF) of charged particles were reconstructed from Trigger counter, TOF wall and RF signal from the storage ring. The mass of charged particle ($M^2 = p^2 \cdot (\frac{1}{\beta^2} - 1)$) can be evaluated from momentum ($p$) and velocity ($\beta = \frac{v}{c} = \frac{Length_{Flight}}{TOF \cdot c}$).

The TOF is given by $TOF = T_{stop} - T_{start}$. In the LEPS spectrometer, the $T_{start}$ time can be used from Trigger counter and RF signal from storage ring. $T_{stop}$ was determed by TDC signal of TOF wall. The time resolution is good for RF signal due to the narrow width of the RF signal[51]. We used RF signal for $T_{start}$.

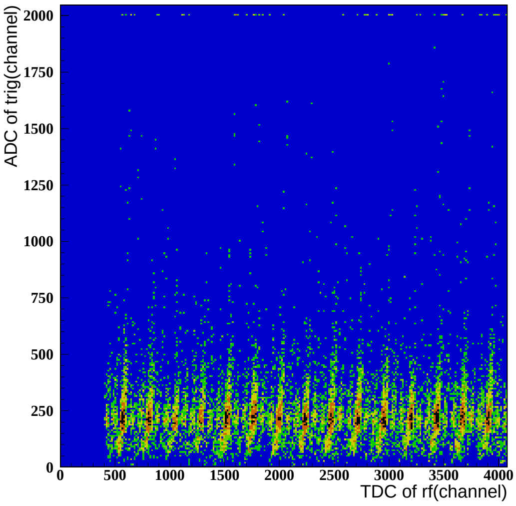

**Figure 3.3:** Scatter plot of ADC for Trigger counter and TDC for RF signal.

The circulating electrons are bunched according to a RF signal, and the arrival time of a BCS photon at the target position is synchronized with the RF signal. First, we corrected RF signal due to the DAQ trigger time is opened by the TDC signal from the Trigger counter and its TDC signal has a time-walk. The time-walk often happens the TDC signal is distorted the height of ADC signal. Figure 3.3 shows the scatter plot of ADC for Trigger counter and TDC for RF signal. We can see clearly 2 ns structure of RF signal and bend for the lower ADC channel of Trigger counter. The corrected RF signal ,$T_{RF_{corr}}$, was calibrated by using the time-work correction by given by

$$\begin{aligned} T_{RF_{corr}} = T_{RF_{raw}} & \\ & - \left(\frac{TDC_{trg1}}{2} - \frac{P_1}{2\sqrt{ADC_{trg1}}} + \frac{P_2}{2ADC_{trg1}}\right) \\ & - \left(\frac{TDC_{trg2}}{2} - \frac{P_3}{2\sqrt{ADC_{trg2}}} + \frac{P_4}{2ADC_{trg2}}\right) - P_5, \end{aligned}$$

where $T_{RF_{raw}}$ is raw TDC signal of $RF$, $TDC_{trig1}$ and $TDC_{trig2}$ ($ADC_{trig1}$ and $ADC_{trig2}$) indicate TDC (ADC) signal of Trigger counters. Figure 3.4 shows the comparison of before time-walk correction and after time-walk correction. We now can see clearly 2 ns structure in the TDC distribution. Each peak denote the relative time of the RF signal. Therefore, we measured the mean

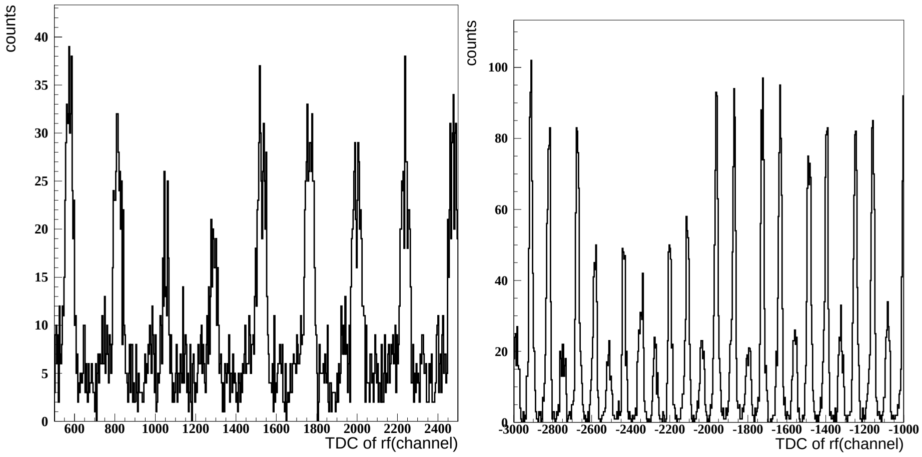

**Figure 3.4:** RF before after

position of the each peak with Gaussian form and synchronized RF signal with trigger time.

TOF wall is performed the measurement of time-of-flight and hit position of charged particles. TOF wall were fablicated with plastic scintillator and also calibrated Time-walk correction to got good resolution. The equation of time-walk for TOF is given by

$$T_{TOF_{corr}} = \frac{(TDC_{Top} + TDC_{Bot})}{2} - (P_1 + \frac{P_2}{\sqrt{ADC_{Top}}} + \frac{P_2}{\sqrt{ADC_{Bot}}}) + P_4,$$

where $TDC_{Top}$ and $TDC_{Bot}$ indicate $TDC_{Top,Bot} = TDC_{Top\,raw,Bot\,raw} - RF_{cor}$.

The effective velocity of light in the scintillator measured by using the result of tracking analysis and TDC difference from top to botom PMT of the TOF bar. The y-hit position was reconstructed by

$$y_{tdc} = v_{eff} \cdot (TDC_{Top} - TDC_{Bot}) + T_{Off},$$

where $v_{eff}$ is effect velocity in the TOF bar. $v_{eff}$ was estimated by comparing with the y-hit position from tracking analysis results, $y_{trk}$, and $TDC_{Top} - TDC_{Bot}$. Figure 3.5(a) shows the scatter plot of the y-position $y_{trk}$ and TDC difference of $T_{Top} - T_{Bot}$. We fit the distribution and the slope is $v_{eff}$. $T_{off}$ is the time difference when the $y_{trk}$ is 0 mm. From the effective velocity, y-hit position from TDC, $y_{tdc}$ was reconstructed. Figure 3.5(b) shows a difference of $y_{trk} - y_{tdc}$. We fitted the distribution with Gaussian function and the resolution is about 18 mm. The distribution is not perfactly a Gaussian distribution due to each TOF bar has a little difference resolution, but the resolution is less than 23 mm.

Mass reconstruction can be measured with the momentum and velocity, $\beta$, of the particles. The $\beta$ was calculated by $\beta = \frac{v}{c} = \frac{Length_{Flight}}{Time_{Flight} \cdot c}$, where $Length_{Flight}$ were calculated by tracking

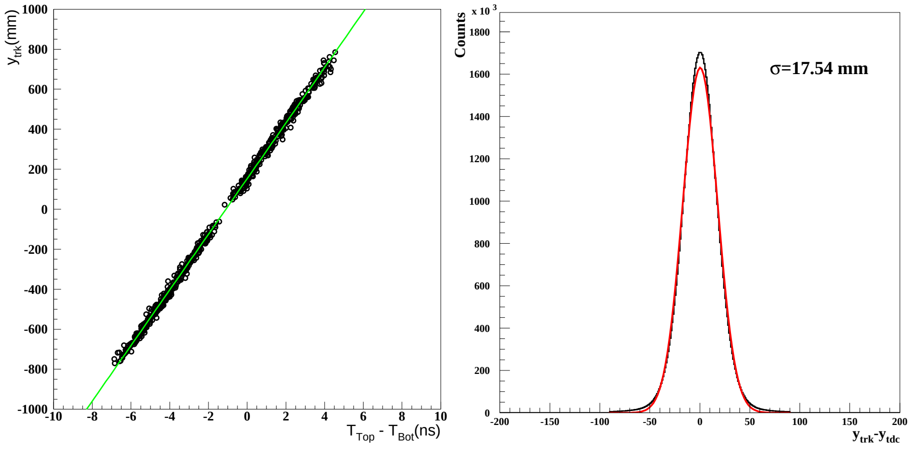

(a) (b)

**Figure 3.5:** Scatter plot of the y-position $y_{trk}$ and TDC difference of $T_{Top} - T_{Bot}$ (a). (b) is distribution of $y_{trk} - y_{tdc}$. An overlaid line denotes fit results by the Gaussian function.

analysis. The $TOF$ was determed by

$$\begin{aligned} TOF &= \frac{(TDC_{rawTop} - RF_{cor} + TDC_{rawBot} - RF_{cor})}{2} \\ &- (P_1 + \frac{P_2}{\sqrt{ADC_{Top}}} + \frac{P_2}{\sqrt{ADC_{Bot}}}) + P_4 \times 0.025 + T_{Glob} + T_0, \end{aligned}$$

where $T_{Glob}$ is globel offset of the TOF bars. $T_0$ is offset of the each TOF bars. 0.025 is the time in one channel of TDC module (1 ch = 0.025 ns). We tuned the $T_0$ values to get same mass resconstruction for each bar.

Figure 3.6 shows events selection of the $T_0$ calibration for TOF. Each cut critia indicate proton, $K^+$, $\pi^+$, and $\pi^-$ as shown in Figure 3.6. Then, we got $T_0$ values by using following equation.

$$T_0 = \sqrt{\frac{M_{PID}^2}{P_{Momentum}^2} + 1} - (T_{TOF_{cor}} \times 0.025 + T_{Glob})$$

$M_{PID}$ : Mass of the selected particles
$P_{Momentum}$ : Momentum of the selected particles

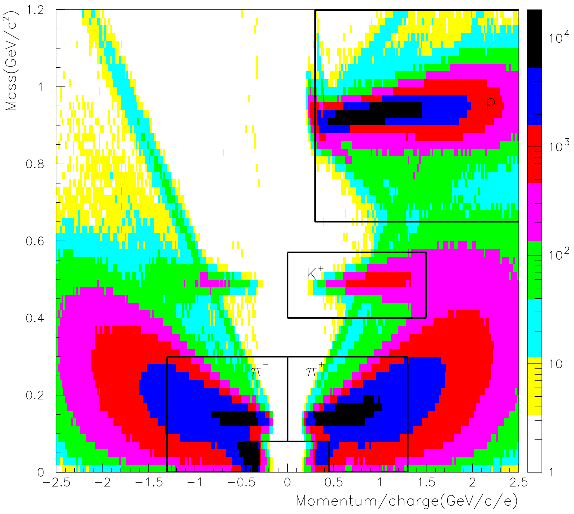

**Figure 3.6:** PID of $T_0$ calibration for TOF.

## 3.3 Photon beam energy and VTX alignment

Photon energy was determined by Tagger counter. The recoiled electrons for BCS photon passed trough two fiber layers and hodoscope. The hit position of the each layer strongly related with BCS photon energy due to the recoiled electrons for lose a lot of energy are strognly bent from the magnetic field in the storage ring. Therefore, we used missing mass distribution for the calibration of the photon energy.

We selected $K^+$ single-track events and $\Lambda$ events to calibrate photon beam energy. We can be calculated the required photon energy from the energy-momentum balance for $p(\gamma, K^+)\Lambda$ when detected $\Lambda$ events in the spectrometer and its mass has PDG value(1115.683 MeV) as given by

$$E_\gamma^{calc} = \frac{m_\Lambda^2 - m_p^2 - m_{K^+}^2 + 2m_p E_{K^+}}{2(m_p - E_{K^+} + p_{K^+}^z)}$$

, where $m_\Lambda$, $m_p$, and $m_{K^+}$ represent the mass of $\Lambda$, proton and kaon, respectively. $E_{K^+}$ denotes a energy of $K^+$. We measured the required photon energy for only a hit exists one front fiber layer or rear fiber as shown in Appendix C. The $\Lambda$ events were shown the fiber layers channel from 1 to 53. We obtained centroids of the required photon energy for $\Lambda$ and $\Sigma^0$ by fitting with two Gaussian functions plus a straight line as shown in Appendix C. Now, we fitted the relation between the

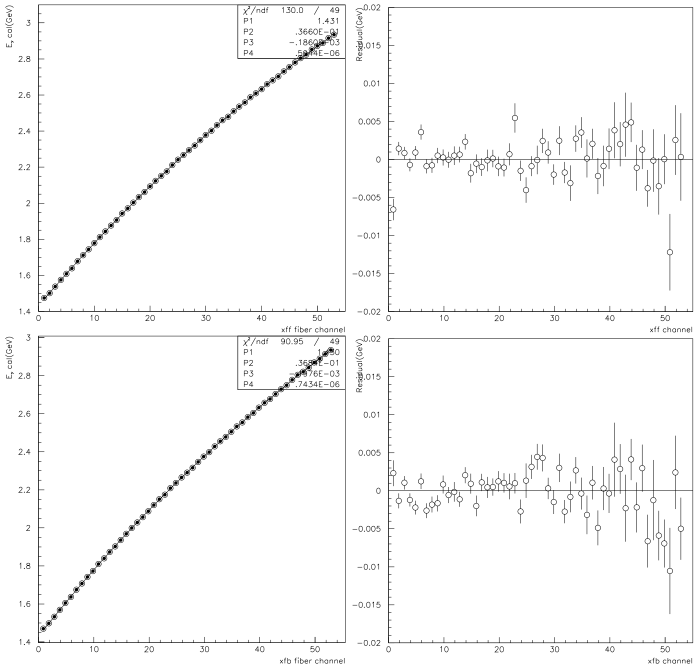

**Figure 3.7:** Photon energies calculated from the energy-momentum balance for $p(\gamma,K^+)\Lambda$ reaction in terms of their respective fiber channels in the tagger(left). Residuals from the fit function are plotted in terms of the fiber channels (right). Top figures denote front fiber distributions and bottom figures indicate rear fiber distributions, respectively.

calculated photon energies and the fiber channel numbers with the 3rd-order polynomial for front fibers(left top) and rear fibers(left bottom) as shown in 3.7. In the right pannel of Figure 3.7, residuals from the fit function are plotted in terms of the fiber channels for front fibers(right top) and rear fibers(right bottom), respectively. Commonly, the residual is less then 10 MeV, which 10 MeV is the resolution of the photon energy for standard energy resolution [52].

The photon-energy functions were obtained as

$$\begin{aligned} E_{\gamma,\mathrm{F.Fiber}} &= 1.43067 + 3.66348 \times 10^2 \cdot x \\ &\quad -1.90912 \times 10^4 \cdot x^2 + 7.05713 \times 10^7 \cdot x^3 \\ E_{\gamma,\mathrm{B.Fiber}} &= 1.43059 + 3.67213 \times 10^2 \cdot x \\ &\quad -1.93408 \times 10^4 \cdot x^2 + 7.10902 \times 10^7 \cdot x^3 \end{aligned}$$

Figure 3.8 shows $p(\gamma, K^+)X$ reaction by using photon-energy function. The peaks are $\Lambda$, $\Sigma^0$, $\Sigma(1385)^0/\Lambda(1405)$ and $\Lambda(1520)$. The peaks were satistified PDG values within 3 MeV.

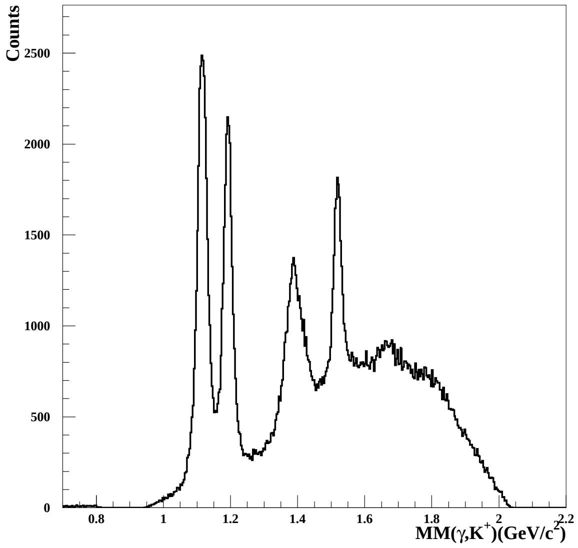

**Figure 3.8:** The missing mass spectrum of $p(\gamma, K^+)X$ reaction with good track selection. The peaks are $\Lambda$, $\Sigma^0$, $\Sigma(1385)^0/\Lambda(1405)$ and $\Lambda(1520)$.

Figure 3.9 shows the reconstructed photon-energy distribution for events with a proton track found. The reconstructed photon-energy distribution has a fluctuation due to some fiber has a bad efficiency.

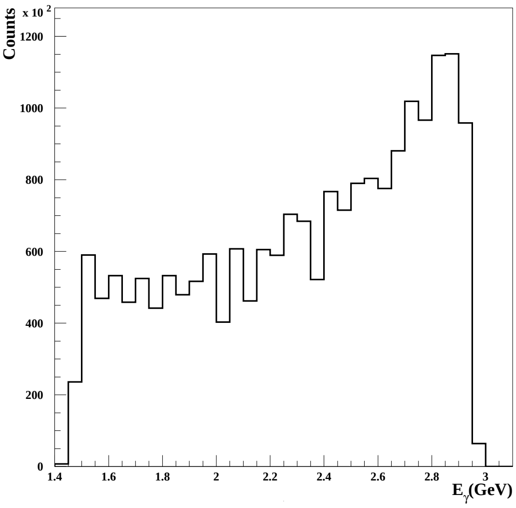

**Figure 3.9:** Photon energy distribution with a proton track found.

## 3.4 PID of $K^+\pi^-$

We want to select of the $\gamma p \to K^{*0}\sigma^+$ reaction from the large dataset. The $K^{*0}$ decays strongly to $K^+\pi^-$ mode with ~100 % fraction ratio. We selected $K^+\pi^-$ events out of two-track events. Figure 3.10(left figure) shows a distribution of reconstructed mass versus momentum/charge for charged particles. The boundary of particle identification(PID) used standard PID cut [51]. We used following parametrization for the mass resolution:

$$\sigma_{M^2}^2 = 4M^4\left(1+\left(\frac{M}{p}\right)^2\right)a_1^2 + 4M^4p^2a_2^2 + rp^2(p^2+M^2)\left(\frac{c}{L}a_3\right)^2$$

, where $M$ is mass of charged particle in the PDG value and $p$ is its momentum. $c$ is the speed of light and $L$ is path length. The $a_1$ is the contribution from the multiple scattering. The $a_2$ and $a_3$ are the contribution from the resolution of spectrometer and the resolution of TOF, respectively. $a_1$ and $a_2$ were estimated by Monte-Carlo simulation. The average resolution of the TOF counter, which is $a_3$, was measured to be 175 psec in real data [51].

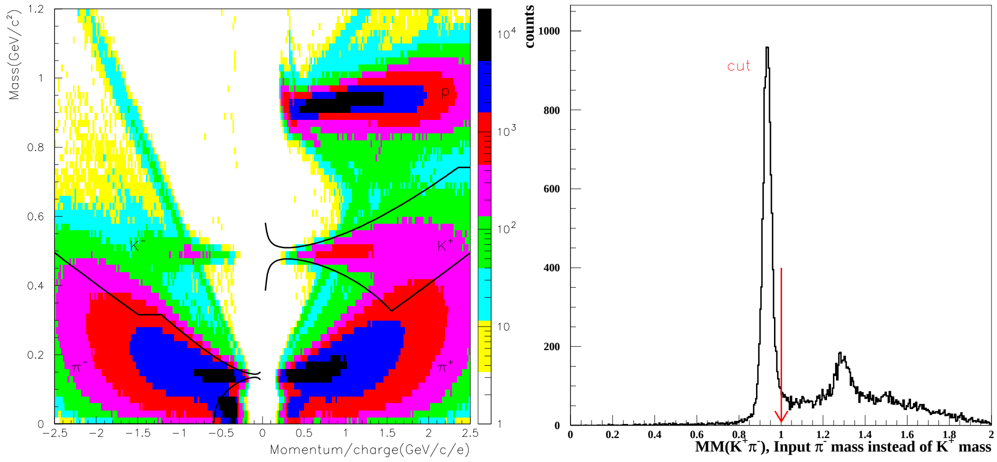

**Figure 3.10:** Left figure shows a two-dimensional scatter plot for of reconstructed mass and momentum/charge. Overlaid lines indicate the event selection for $K^+$ and $\pi^-$ track. Right figure shows a missing-mass spectrum for $p(\gamma,\pi^+\pi^-)X$ reaction assuming $K^+$ as $\pi^+$.

We required that a reconstructed mass should be within $3\sigma$ tolerance window. At high momentum the mass windows for $\pi$ and $K$ are overlapped. Hence, we imposed a further constraint on the mass such that it should not be in the $2\sigma$ mass region of the other. As seen in Figure 3.10, there still remain $\pi^+$ tracks in the $K^+$ mass region. Such misidentified $K^+$ tracks were rejected by requiring that a missing mass for $p(\gamma,\pi^+\pi^-)X$ reaction be above 1.002 GeV/$c^2$ assuming $K^+$ as $\pi^+$(replacing $m_{K^+}$ with $m_{\pi^+}$), as shown in the right panel of Figure 3.10.

Figure 3.11 shows the vtz distribution for $K^+\pi^-$ events. We can see clear structures of the target, the start count and the SSD detector. The red spectrum indicates events selected with the range from $-1042$ mm to $-860$ mm.

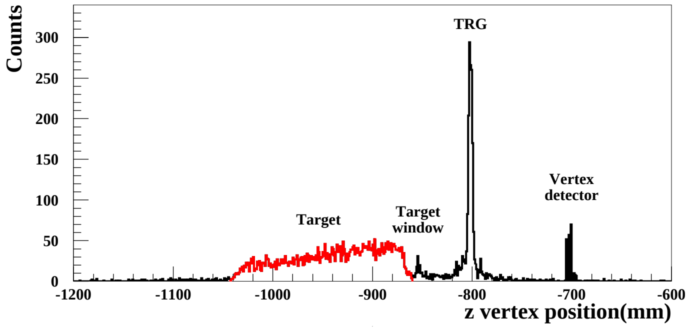

**Figure 3.11:** Vertex-z distribution for $K^+\pi^-$ events.

For the selection of good track events, the following selection criteria were imposed :

### Tagger hit

We used a cut of number of tracks in tagger counter(fntag) due to selection of the good track of the recoil electron for the BCS process in the storage ring. The recoil electrons for high energy which is corresponding to low photon energy can be produced a shower at the shielding material. The event were made a track in the tagging system. Therefore, we required to following cut condition to reject background event from tagger counter :

$$\mathrm{fntag} = 1$$

### $\chi^2$ probility

The $\chi^2$ probability cut was used to reject decay in flight events. We required the event selection for the $\chi^2$ probability of reconstructed track was required to be greater then 0.02 as following criteria :

$$\mathrm{prbchi2} > 0.02$$

### Consistency of TOF hit

The number of hits in TOF bar were It is required that a hit is required by TOF counter. To select events for more then one hit by TOF counter, we selected in the analysis as following criteria:

$$\mathrm{ithtofhit} > 0.$$

### Number of outlier

If hit of tracking chambers were deviated from the expected trajectories more than the resolution, the hit was judged as a background hit (outlier) and removed from the tracking. Decay-in-flight event had a track with a large number of outliers when it decayed in the middle of tracking volume. When the number of outliers were less then 7, the tracks were selected in the analysis as following criteria:

$$\mathrm{noutl} < 7$$

### Consistency of TOF hit

We make cuts on the difference of x and y positions between reconstructed hit position using tracking system at the TOF counter and the measured positions by the TOF counter itself. We required the cut condition for the difference of the TOF slat number, |itof-tofid|, and the difference of Y coordinate, |ytof-tofdiff|, using following criteria :

$$\begin{aligned} |\mathrm{itof} - \mathrm{tofid}| &< 2 \\ |\mathrm{ytof} - \mathrm{tofdiff}| &< 80\mathrm{mm} \end{aligned}$$

### Rejection of $e^+e^-$ background events

The $e^+e^-$ particles of below 1 GeV/c momenta were blocked by the lead blocker in the dipole magnet. High momenta $e^+e^-$ particles were rejected by veto signal from the $e^+e^-$ veto bar downstream of the DC3. However there is a possibility that the $e^+e^-$ events were accepted accidental event in the hadron trigger. The greater part of accidental $e^+e^-$ events are rejected by the standard PID cut. We applied the additional cut condition using the reconstructed virtual plane of y position for lead blocker, which is ybar, and $e^+e^-$ veto bar, which is yebar. We rejected accidental $e^+e^-$ events using the following criteria :

$$\begin{aligned} -30\mathrm{mm} < \ & \mathrm{ybar} < 16\mathrm{mm} \\ -30\mathrm{mm} < \ & \mathrm{yebar} < 16\mathrm{mm} \end{aligned}$$

Figure 3.12 shows the distributions of key parameters for primary event selection for $K^+\pi^-$ particles. Black histograms shows the distributions of key ntuple variables for $K^+\pi^-$ skimmed events, while red ones shows the distributions for selected $K^+\pi^-$ events.

The survived event numbers are listed in Table 3.2 for each cut condition. Figure 3.13 shows reconstructed mass distributions before(a) and after(b) the MM($\pi^+\pi^-$) cut. There still remain some $\pi^+$-like tracks in the $K^+$ mass region, which might originate from multi-pion production processes.

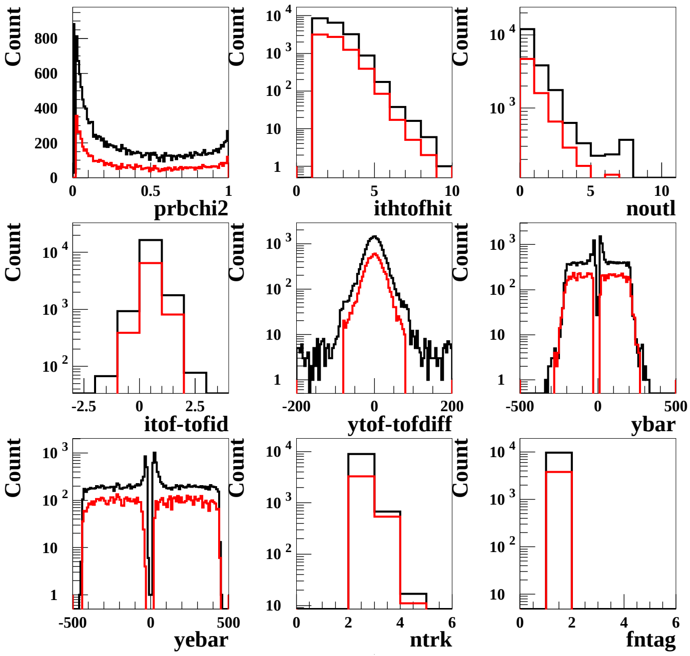

**Figure 3.12:** Black histograms shows the distributions of key ntuple variables for $K^+\pi^-$ skimmed events, while red ones shows the distributions for selected $K^+\pi^-$ events.

| Cuts | Vert | Hori | Counts | Ratio |
|---|---|---|---|---|
| All event | 95,772,464 | 109,557,736 | 205,330,253 | — |
| fntag=1 | 63,911,891 | 72,908,803 | 136,820,694 | — |
| ntrk>1 | 2,103,644 | 2,548,750 | 4,652,394 | — |
| PID of $K^+$ and $\pi^-$ | 9,659 | 13,219 | 22,878 | 1.000 |
| pm2cor>0 | 8,415 | 11,709 | 20,124 | 0.880 |
| MM($\pi^+\pi^-$)>1.002 GeV | 5,017 | 5,828 | 10,845 | 0.474 |
| vtz cut | 3,050 | 3,546 | 6,596 | 0.288 |
| Decay in flight | 2,647 | 3,075 | 5,722 | 0.250 |
| $e^+e^-$ blocker cut | 2,533 | 2,931 | 5,464 | 0.239 |
| $e^+e^-$ bar cut | 2,533 | 2,931 | 5,464 | 0.239 |
| $E_\gamma > 1.85$ GeV | 2,478 | 2,849 | 5,327 | 0.233 |

**Table 3.2:** Cut conditions and the number of survived events for $K^+\pi^-$ selection.

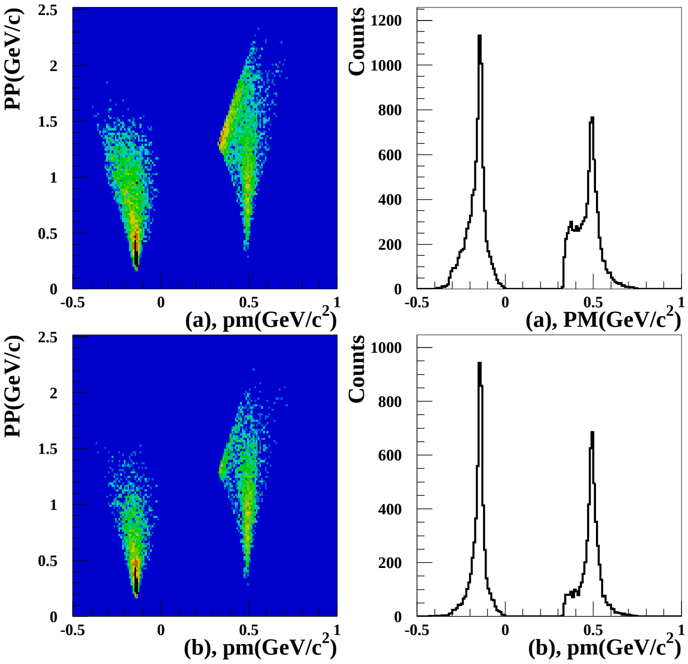

**Figure 3.13:** Reconstructed mass distributions before(a) and after(b) the MM($\pi^+\pi^-$) cut.

# Chapter 4

# Results

## 4.1 Event selection

Of 22878 $K^+\pi^-$-track events only 5327 events survived with good track criteria. The events of $K^{*0}\Sigma^+$ photoproduction were identified using the invariant mass and the missing mass for the $K^+\pi^-$ system. The invariant mass ($M_{K^+\pi^-}$) and the missing mass ($MM_{K^+\pi^-}$) were calculated as follows :

$$\begin{aligned} M^2_{K^+\pi^-} &= \left(\sqrt{m^2_{K^+}+p^2_{K^+}}+\sqrt{m^2_{\pi^-}+p^2_{\pi^-}}\right)^2 - |p_{K^+}+p_{\pi^-}|^2 \\ MM^2_{K^+\pi^-} &= \left[E_\gamma + m_p - \left(\sqrt{p^2_{K^+}+m^2_{K^+}}+\sqrt{p^2_{\pi^+}+m^2_{\pi^+}}\right)\right]^2 \\ &\quad -\left[(p^x_{K^+}+p^x_{\pi^-})^2+(p^y_{K^+}+p^y_{\pi^-})^2+\left(E^z_\gamma-(p^z_{K^+}+p^z_{\pi^-})\right)^2\right], \end{aligned}$$

where $p_{K^+}$ and $p_{\pi^-}$ are the measured $K^+$ and $\pi^-$ momenta, and $E_\gamma$ is the tagged photon energy by tagging counter.

Figure 4.1(a) shows a two-dimensional plot of a missing mass for $p(\gamma, K^+\pi^-)X$ versus an invariant mass for the $K^+\pi^-$ system. We can see a clear spot distribution, which spot shows a $K^{*0}$ production associated with $\Sigma^+$ production. An overlaid red box indicates the $K^{*0}$-event selection region with $3\sigma$ mass tolerance. Bottom figures of Figure 4.1 show the projected spectra for missing mass (b) and invariant mass (c) distributions, respectively. The missing mass and invariant mass distribution show clear peaks of $\Sigma^+$ and $K^{*0}$, respectively. Of course, we can see the background below peaks cause from 3-body decay, non-resonant processes and hyperons production. We imposed a constraint on the missing mass for $p(\gamma, K^+\pi^-)X$ reaction such that $|m_X - m_{\Sigma^+}| < 0.033$

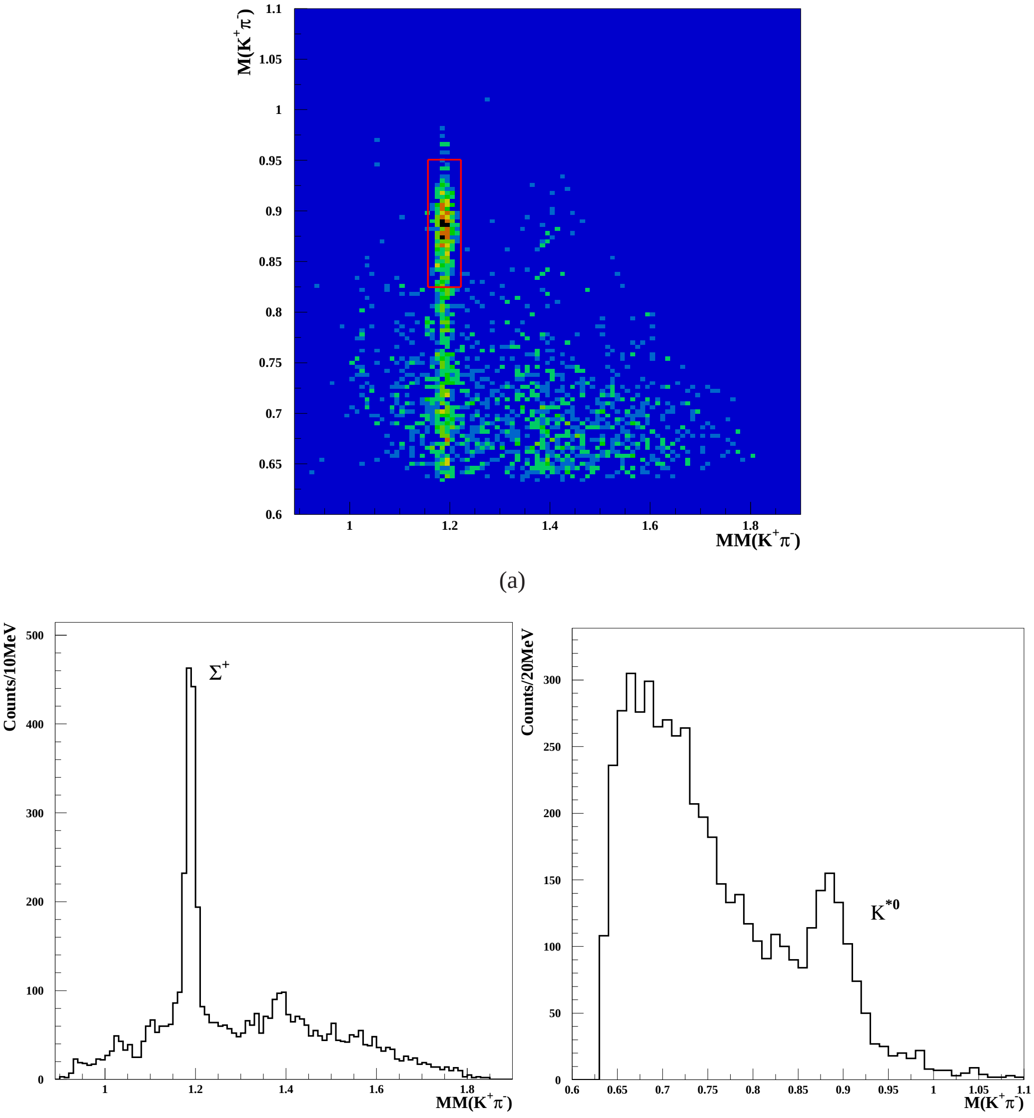

(a)

(b)

(c)

**Figure 4.1:** Scatter plot of missing mass for $p(\gamma, K^+\pi^-)X$ in terms of invariant masses of the $K^+\pi^-$ system (a). Bottom figures are the projected spectra for missing mass (b) and invariant mass (c) distributions, respectively.

(MM($K^+\pi^-$) cut). The $K^+\pi^-$ invariant mass spectrum after the MM($K^+\pi^-$) cut is shown in the left panel of Figure 4.2. The $K^{*0}$ peak was clearly seen in the spectrum with small background. On the other hand, we imposed the $K^+\pi^-$ invariant mass constraint before the MM($K^+\pi^-$) cut. We required that $|m_{K^+\pi^-} - m_{K^{*0}}| <$ 0.063 MeV, where $m_{K^{*0}}$ denotes a fit value of $K^{*0}$ mass (0.8877 MeV) (IM cut). The missing mass distribution for $p(\gamma, K^+\pi^-)X$ reaction after the IM cut is shown in the right panel of Figure 4.2. The spectrum shows not only $\Sigma^+$ peak, but also small amount of $\Sigma(1385)^+$ peak. Below $\Sigma^+$ peak, only few background remains after IM cut and the background distribution is almost flat. The technique of sideband subtraction can be used to remove the remaining background.

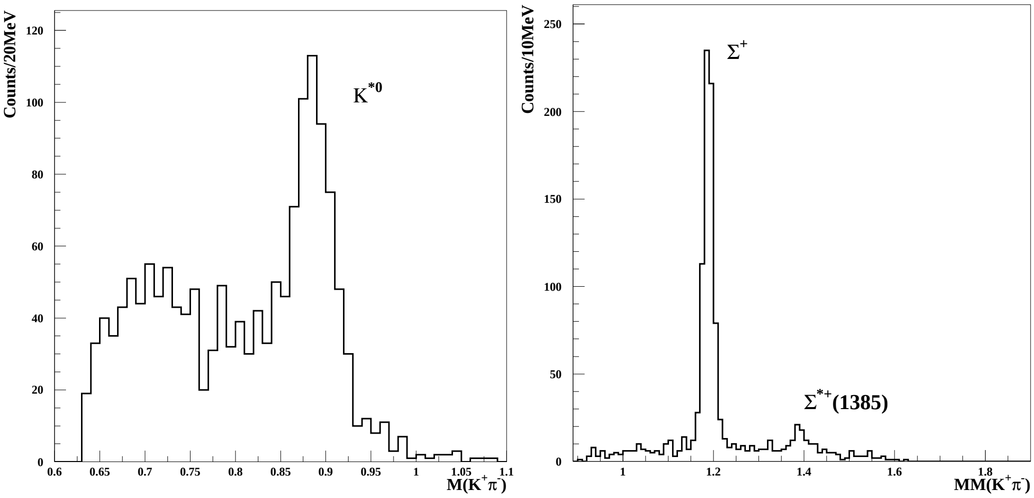

**Figure 4.2:** Invariant mass (left) and missing mass (right) for $K^+\pi^-$ system by the $3\sigma$ of $\Sigma^+$ peak and $K^{*0}$ peak, respectively.

We selected the $\Sigma^+$ events region by a cut on the mass from 1.156 to 1.222 as shown by two vertical arrows in middle of spectrum in the left pannel of Figure 4.3. The left and right side-band regions selected by a same width on either side of the $\Sigma^+$ region, which indicate $BG1$ and $BG2$ in the left pannel of Figure 4.3. Right pannel of Figure 4.3 shows the the $K^+\pi^-$ invariant mass distribution with $\Sigma^+$ events selection. The side-band events indicated by a red histogram. Signal is defined as follows:

$$Signal = (Signal + BG) - \frac{BG1 + BG2}{2}$$

The $K^+\pi^-$ invariant mass spectrum after the side-band subtraction is shown in Figure 4.4. It should be noted that the $K^{*0}$ peak still sits on some background events which largely populate at a low mass tail of the $K^{*0}$. These backgrounds were though to be hyperon background and non-resonant processes production, it will be discussed below.

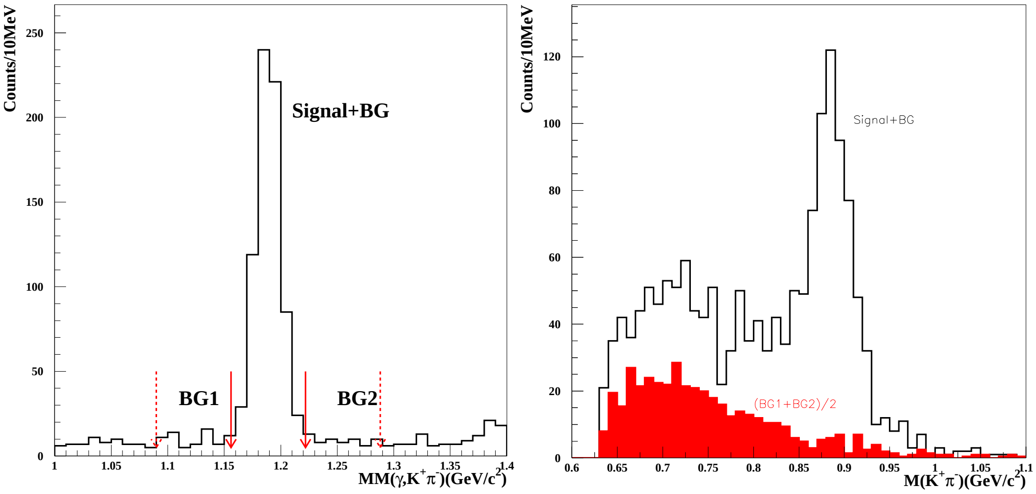

**Figure 4.3:** Selection of background region for missing mass distribution of the $(\gamma, K^+\pi^-)$ and the $K^+\pi^-$ invariant mass distribution for side-band events.

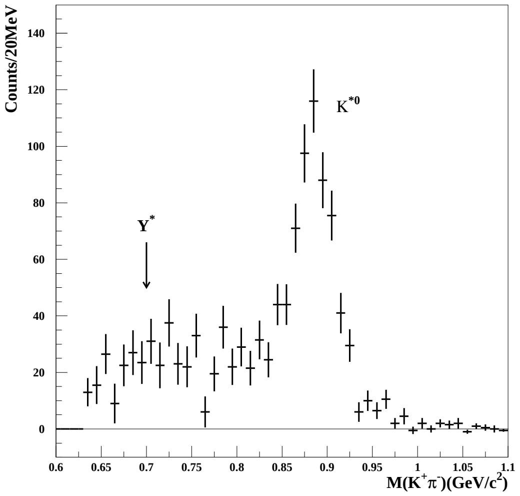

**Figure 4.4:** The $K^+\pi^-$ invariant mass distribution with side-band background subtraction.

## 4.2 Mass and width of $K^{*0}$

We estimated the mass and width of $K^{*0}$ because of measurable $K^{*0}$ peak is a little different compared with PDG [8]. Figure 4.5 shows the invariant mass of $K^+\pi^-$ system with $\Sigma^+$ selection and the subtracted side-band background. The background of low mass region was though to be hyperons production and non-resonant processes. The overlaid red line shows the estimated background structure with hyperons and non-resonant processes described below, as shown in Figure 4.5(a). Figure 4.5(b) shows the fit result a Breit-Wigner form without acceptance correction. The mean value is estimated to be 883.7 ± 1.3 MeV, however its value is smaller than PDG value(896.00 ± 0.26 MeV) and we can not reproduce the distribution of real data by using Monte-Carlo simulation. This problem solved by employing the acceptance as a function of invariant mass. Figure 4.5(c) shows the acceptance for detecting $K^{*0}$ as a function of the $K^+\pi^-$ invariant mass. The acceptance was continuingly decreased when invariant mass was increased, and also we

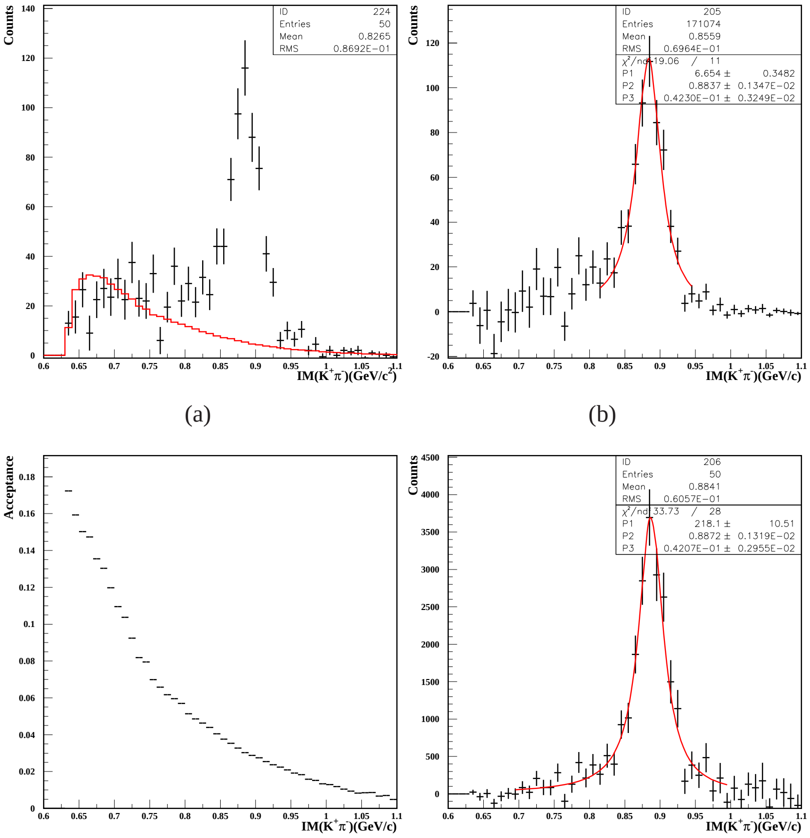

(a) (b)

(c) (d)

**Figure 4.5:** The $K^+\pi^-$ invariant mass distribution without background subtraction (a) and with background subtraction (b). (c) is acceptance for detecting $K^{*0}$ as a function of the $K^+\pi^-$ invariant mass. (d) shows fit result with Breit-Wigner form after acceptance correction.

found the acceptance didn't depend on $K^{*0}$ peak position. Figure 4.5(d) shows the invariant mass distribution with acceptance correction. The red line represents the fit result with a Breit-Wigner form. The $K^{*0}$ mass is estimated to be 887.23 ± 1.32 MeV and its full width to be 42.05 ± 3.25 MeV. We used this parameter to produce the Monte-Carlo data.

## 4.3 Monte-Carlo simulation

The acceptance of the $K^{*0}$ photoproduction for the LEPS spectrometer was studied by a Monte-Carlo simulation, using the GEANT3 software [45]. The Monte-Carlo simulation code, called g3leps, has been developed by LEPS collaboration [49]. To assume the realistic values, we simulated g3leps with the resolutions of the SVTX, DCs, photon energy and the time-of-flight.

We generated $K^{*0}\Sigma^+$ reaction and processed during passage of the particles through the experimental apparatus which also including particle decay, energy loss, multiple scattering of particles. The decay angular distribution from the $K^{*0}$ particle was produced by arbitrary spin density matrices values in the GJ frame and helicity frame.

We implemented the best fit values for the mass and width with Breit-Wigner form from previous section for the $K^{*0}$ peak, mass is 887.23 MeV and width is 42.05 MeV, in the Monte-Carlo simulation and the mass of $\Sigma^+$ carried out with PDG value, which is 1.18937 GeV as shown in Figure 4.6. In the right pannel of Figure 4.6, the overlaid red line shows the fit result of the generated $K^{*0}$ distrigution with Breit-Wigner form.

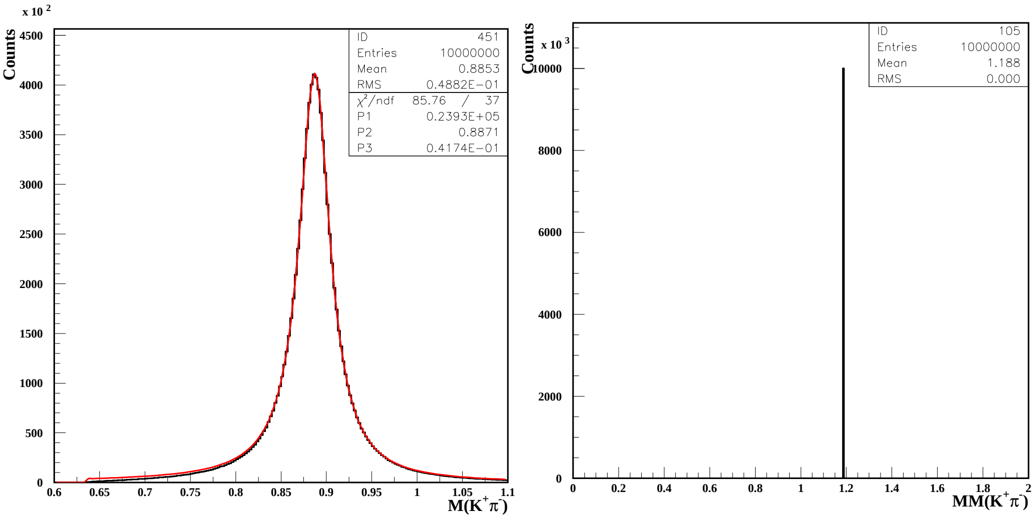

**Figure 4.6:** Generated distribution for $K^{*0}$ and $\Sigma^+$.

We used a corrected photon-energy spectrum as reported in Ref. [53] as shown in Figure 4.7. The number of photons were estimated by using The fraction ratio for each photon energy was listed in the Appendix A.

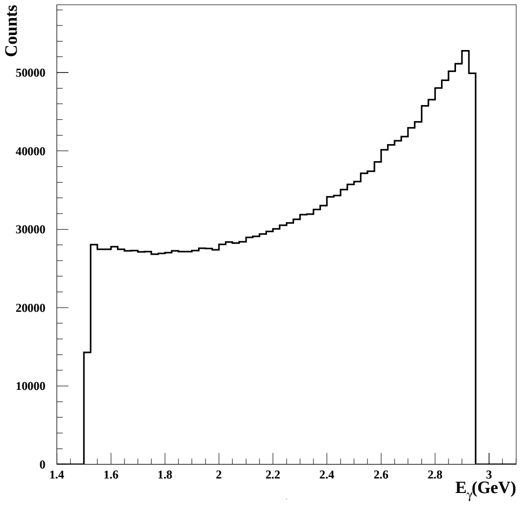

**Figure 4.7:** Generated distribution for photon beam energy.

## 4.4 Slope parameter of $\tilde{t}$ distribution

At forward angles $t$-channel exchange is known to be dominant in the $K^{*0}$ photoproduction. The experimental acceptance for the $K^{*0}$ decay depends on how many $K^{*0}$ populates at forward production angles. We are now in a position to measure the slope parameter $b$ of differential cross sections $d\sigma/dt$ which can be parametrized as

$$\begin{aligned} \frac{d\sigma}{dt} &= n_0 \cdot exp(b\tilde{t}) \\ \tilde{t} &= -|t - t_{min}| \end{aligned}$$

, where $n_0$ is a constant factor, $t$ is the Mandelstam invariant[48] that gives the 4-momentum squared of the exchange particles. The momentum transfer is limited by kinematics from $t_{min}$ to $t_{max}$. $t_{min,max}$ is given as follows:

$$\begin{aligned} t_{min,max} &= \left[\frac{m_{K^{*0}}^2}{2\sqrt{s}}\right]^2 \\ &\quad - \left[\frac{s-m_p^2}{2\sqrt{s}} \mp \sqrt{\frac{(s+m_{K^{*0}}{}^2-m_p^2)^2}{4s} - m_{K^{*0}}^2}\right]^2 \end{aligned}$$

, where $s$ is Mandelstam invariant that given as $s = \sqrt{(E_\gamma + m_p)^2 - E_\gamma^2}$. Figure 4.8 shows $\tilde{t}(-|t - t_{min}|)$ distribution for all energy bin and four energy bins.

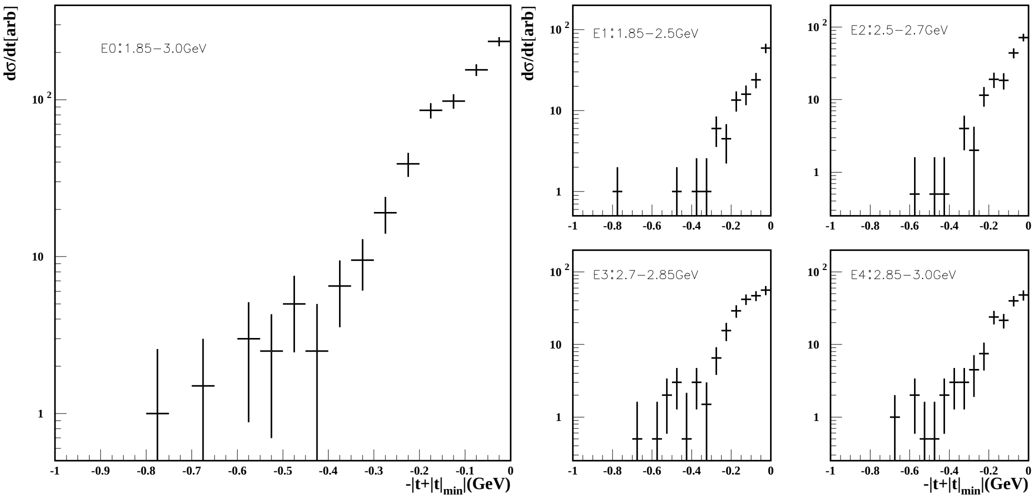

**Figure 4.8:** $\tilde{t}$ distribution for all energy bin and four energy bin.

First, we calculated the acceptance for $\tilde{t}(-|t - t_{min}|)$ distributions based on a Monte-Carlo simulation as shown in Figure 4.9. We generated $K^{*0}\Sigma^+$ photoproduction events with zero spin-density matrix elements. We then fit the acceptance-corrected data with the above equation. Figure

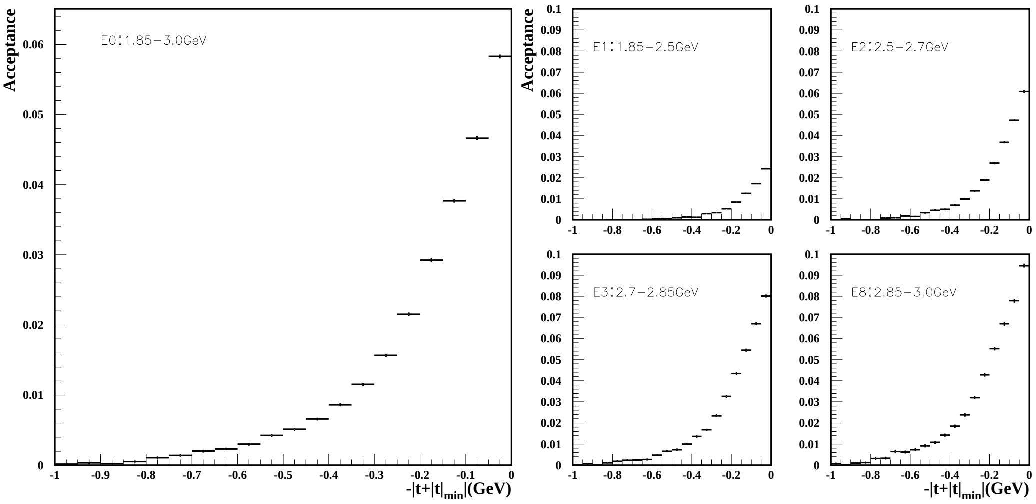

**Figure 4.9:** Acceptance for the LEPS spectrometer as a function of $\tilde{t}$, in 4 energy bin.

4.9 shows the acceptance as a function of $\tilde{t}$ for the $K^{*0}$ photoproduction. Left panel represents the acceptance for a whole energy region, while the right panel figures are the acceptance for each energy bin. The fit results are shown in Figure 4.10. We iterated the slope parameter measurements to study if the slope parameter converged. Table 4.1 lists the slope parameters obtained for each measurement. In 5 iterations the fit results for the slope parameter are staggered within errors, which proves that no further iterations are necessary. We take the average value of the fit results as the slope parameter $b$=4.206 ± 0.231 as shown in Figure 4.11. The slope parameter was used the generator of $K^{*0}\Sigma^{+}$ in Monte-Carlo, which performed realistic-looking Monte-Carlo distribution.

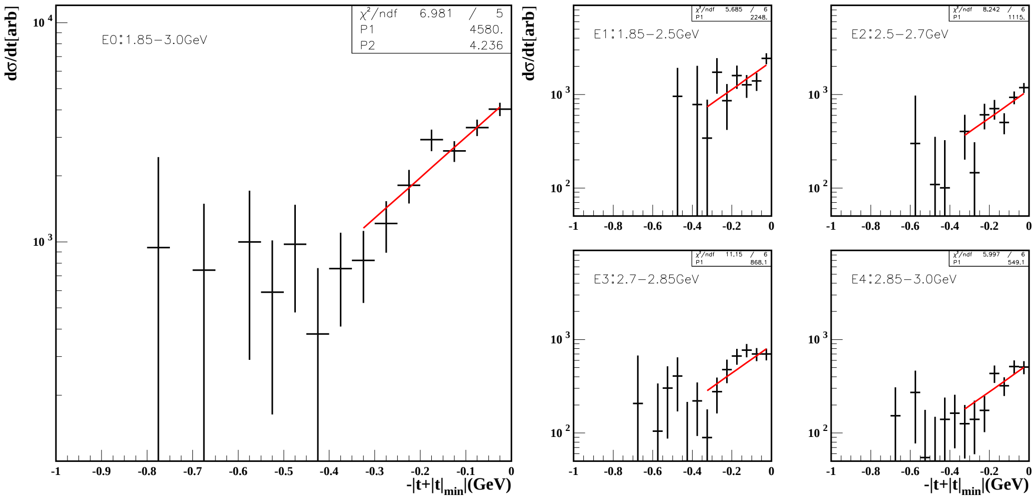

**Figure 4.10:** Acceptance for the LEPS spectrometer as a function of $\tilde{t}$, in 4 energy bin.

| Try | $1^{st}$ | $2^{nd}$ | $3^{rd}$ | $4^{th}$ | $5^{th}$ |
|---|---|---|---|---|---|
| E0 slope ($b$) | 4.224<br>± 0.517 | 4.154<br>± 0.519 | 4.236<br>± 0.517 | 4.187<br>± 0.515 | 4.228<br>± 0.518 |
| E0 $\chi^2/ndf$ | 7.02/5 | 7.15/5 | 6.98/5 | 7.06/5 | 7.01/5 |
| E1 $\chi^2/ndf$ | 5.35/6 | 5.31/6 | 5.41/6 | 5.25/6 | 5.07/6 |
| E2 $\chi^2/ndf$ | 6.56/6 | 7.11/6 | 6.68/6 | 6.68/6 | 6.27/6 |
| E3 $\chi^2/ndf$ | 12.34/6 | 11.55/6 | 11.36/6 | 12.72/6 | 12.15/6 |
| E4 $\chi^2/ndf$ | 4.95/6 | 5.02/6 | 4.85/6 | 4.87/6 | 4.75/6 |

**Table 4.1:** Fitting result for slope parameter as function $\tilde{t}$.

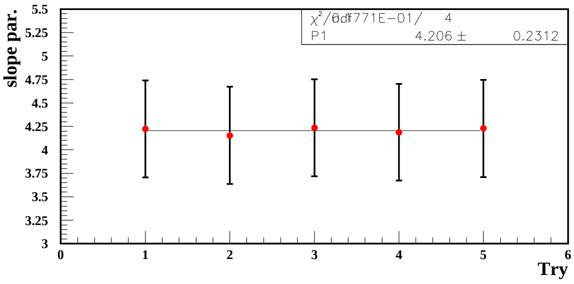

**Figure 4.11:** Fit of slope parameter using five slope parameter.

## 4.5 Hyperon Background

We studied if such a background originates largely from hyperon resonance photoproduction by looking at the $p(\gamma, K^{+})X$ missing mass distribution.

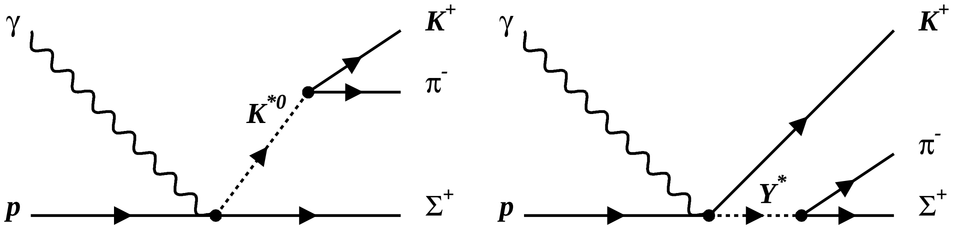

(a) $K^{*0}$ photoproduction (b) hyperon photoproduction

**Figure 4.12:** Tree diagrams for $K^{*0}$ photoproduction (a) and hyperon photoproduction (b).

Figure 4.12 shows tree diagrams for $K^{*0}$ photoproduction and hyperon photoproduction. The $K^{+}\pi^{-}\Sigma^{+}$ final state were involved hyperon ($Y^{*}$) production since the hyperon decays to $\pi^{-}\Sigma^{+}$. Therefore, the $Y^{*}$ peaks are clearly seen in Figure 4.13, which is missing mass distribution of $p(\gamma, K^{+})X$ for the $K^{+}\pi^{-}$ track found. Lower overlaid red histogram indicates the final event selection within 3$\sigma$ of the $\Sigma^{+}$ peak. Very little $Y^{*}$ background remains after a final event cut, their values are non-negligible. In the black solid histogram of the Figure 4.13, we can see not only peaks for $\Lambda$ and $\Sigma$ but also $Y^{*}$ peaks, however type of $Y^{*}$ peaks are not clear.

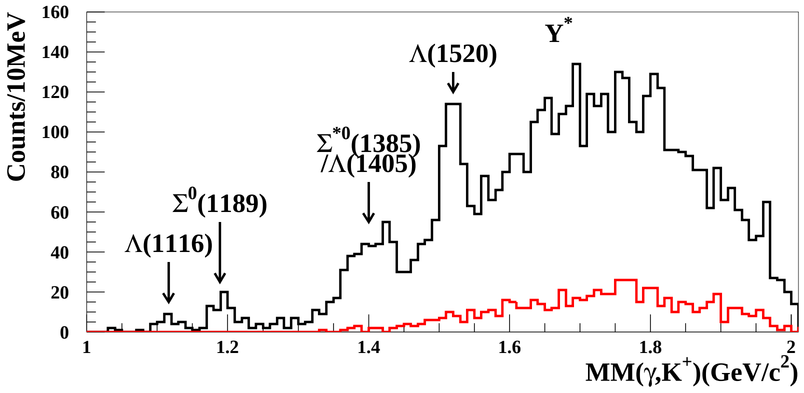

**Figure 4.13:** Missing mass distribution of $p(\gamma, K^{+})X$ for the $K^{+}\pi^{-}$ track found. Overlaid red histogram indicates the final event selection within 3$\sigma$ of the $\Sigma^{+}$ peak.

The $\pi^{-}\Sigma^{+}$ decay is kinematically available from the mass of the parent hyperon above 1.33 GeV. There are 8 hyperon resonances with more the 3-stars rating by Ref. [8] by Particle Data Group, as listed in in Table 4.2.

We first looked at the $\gamma p \to K^{+}\pi^{+}\Sigma^{-}$ reaction, which is free from the $K^{*0}$ production, while for $Y^{*} \to \pi\Sigma$ decays, it shares almost equally with $\gamma p \to K^{+}\pi^{-}\Sigma^{+}$ reaction.

| | rating | mass (MeV) | $\Gamma$ (MeV) | Br ($\pi\Sigma$) |
|---|---|---|---|---|
| $\Lambda(1405)S_{01}$ | **** | $1405.1^{+1.3}_{-1.0}$ | $50 \pm 2$ | 100% |
| $\Lambda(1520)D_{03}$ | **** | $1519.5 \pm 1.0$ | $15.6 \pm 1.0$ | $42 \pm 1$% |
| $\Lambda(1600)P_{01}$ | *** | 1560 to 1700 ($\approx$ 1600) | 50 to 250 ($\approx$ 150) | 10$-$60% |
| $\Lambda(1670)S_{01}$ | **** | 1660 to 1680 ($\approx$ 1670) | 25 to 50 ($\approx$ 35) | 25$-$55% |
| $\Sigma(1660)P_{11}$ | *** | 1630 to 1690 ($\approx$ 1660) | 40 to 200 ($\approx$ 100) | seen |
| $\Sigma(1670)D_{13}$ | **** | 1665 to 1685 ($\approx$ 1670) | 40 to 80 ($\approx$ 60) | 30$-$60% |
| $\Sigma(1750)S_{11}$ | *** | 1730 to 1800 ($\approx$ 1750) | 60 to 160 ($\approx$ 90) | $<$ 8% |
| $\Sigma(1775)D_{15}$ | **** | 1770 to 1780 ($\approx$ 1775) | 105 to 135 ($\approx$ 120) | 2$-$5% |

**Table 4.2:** Properties of the hyperons in the mass from 1.4 to 1.8 GeV.

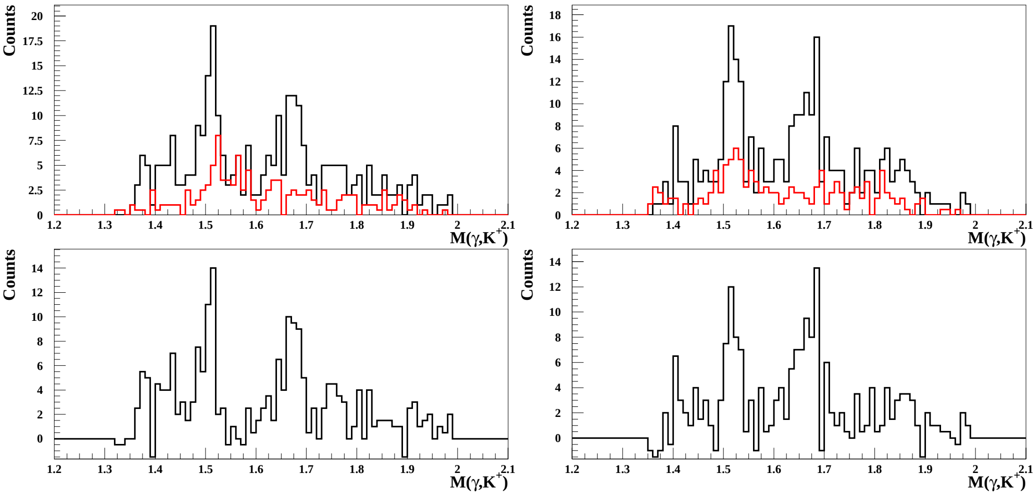

**Figure 4.14:** Missing mass distributions of the vertical and the horizontal polarization data for $p(\gamma, K^+)X$ reaction, where $X$ decay to $\pi^+\Sigma^-$. Red histograms represent the distributions for side-band events. Bottom figures show side-band subtracted distributions.

Figure 4.14 shows the missing mass distributions for $p(\gamma, K^+)X$ reaction, where $X$ decay to $\pi^+\Sigma^-$. It should be noted that both the vertical and the horizontal polarization spectra contain almost equal number of events. We clearly see three peak structures from $\Lambda$(1405), $\Lambda$(1520) and $\Lambda/\Sigma^0$(1670). For the $\Lambda/\Sigma^0$(1670) peak, the Breit-Wigner fit results in the width of 50 MeV as shown in Figure 4.15. We then included these three resonances as well as $K^{*0}$ and non-resonant $K^+\pi^-$ production process in the event generator, hypreso.f, implemented in a Monte-Carlo simulation.

Figure 4.16 shows scatter plots of missing mass for $p(\gamma, K^+)X$ versus the $K^+\pi^-$ invariant mass. Events for $p(\gamma, K^+\pi^-)\Sigma^+$ reaction are displayed in (a), whereas side-band background events are shown in (b). Monte-Carlo simulation data are also shown in (c) $\sim$ (g). Generated $K^{*0}$

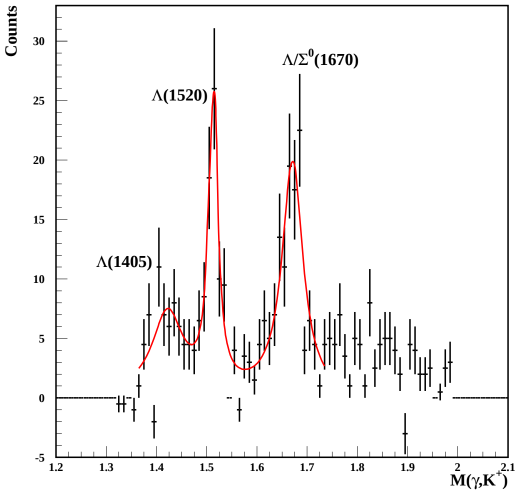

**Figure 4.15:** Missing mass distribution for $p(\gamma, K^+)X$ reaction, where $X$ decay to $\pi^+\Sigma^-$.

events are shown in (c), Λ(1405) in (d), Λ(1520) in (e), Λ(1670) in (f), and non-resonant $K^+\pi^-$ production events in (g), respectively.

We made a template fit to the side-band subtracted distribution with shape functions for $K^{*0}$ production and four background processes discussed above.

$$\sum_{j=1,k=1}^{n,m} N_{j,k} - NSB_{j,k} = \sum_{i=1}^{5} \sum_{j=1,k=1}^{n,m} a_i NMC(i)_{j,k}$$

where $n$ and $m$ are the number of bins for the $K^+\pi^-$ invariant mass and missing mass for $p(\gamma, K^+)X$ reaction, respectively. $j$ and $k$ denote $j^{th}$ and $k^{th}$ bin, respectively. $N_{i,j}$ is the number of events for each bin. The number of events for each bin of side-band represents $NSB_{i,j}$. $a_i$ represents a yield coefficient for each process. $N_{j,k}$ denotes the number of events for $j^{th}$ bin of the invariant mass and $k^{th}$ bin of missing mass for $p(\gamma, K^+)X$. $i$ represented each reaction for the generated Monte-Carlo simulation data, such as generated $K^{*0}$ events, $\Lambda(1405)$ events, $\Lambda(1520)$ events, $\Lambda(1670)$ events and non-resonant $K^+\pi^-$ production events. $NMC(i)_{j,k}$ denotes number of events for Monte-Carlo data. The $\chi^2$ is

$$\chi^2 = \sum_{j=1,k=1}^{n,m} \frac{[N_{j,k} - NSB_{j,k} - \sum_{i=1}^{5}(a_i)NMC(i)_{j,k}]^2}{\sigma_{j,k}^2}$$

where, $\sigma_{j,k}$ is statistical error of $(N_{j,k} - NSB_{j,k})$ for each bin. $MC$ is the estimated Monte-Carlo yield. We used the MINUIT package to obtain yield parameters for background by minimizing $\chi^2$.

Figure 4.17 shows the template fit results for the invariant mass distribution (top) and the missing mass distribution (bottom). Left figures are the distributions for vertical polarization and right figures are those for horizontal polarization. Each contributions is represented by a different

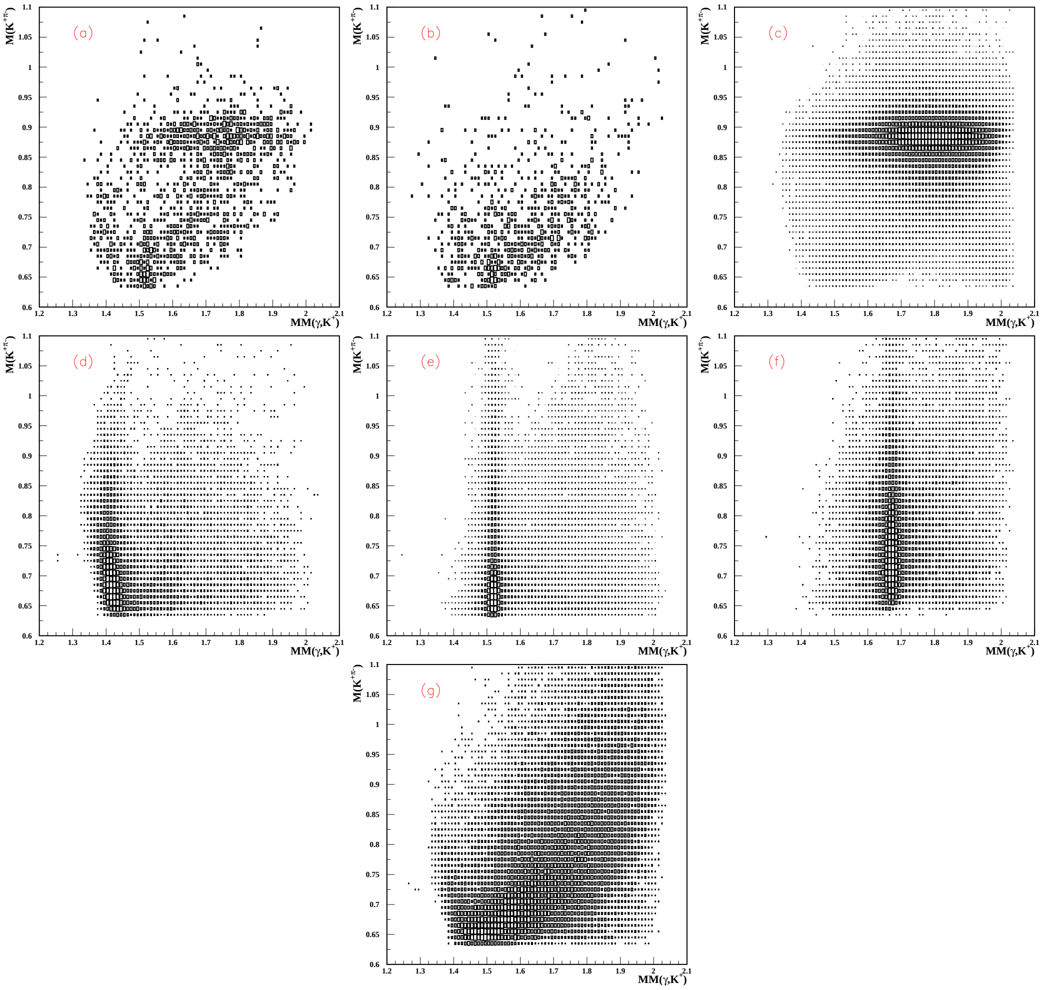

**Figure 4.16:** Missing mass distributions for $p(\gamma, K^+)X$ in terms of the $K^+\pi^-$ invariant mass distributions. The $K^+\pi^-$ events are shown in (a) with a $\Sigma^+$ Selection in the missing mass for $p(\gamma, K^+\pi^-)X$ reaction. Side-band background events are plotted in (b). Monte-Carlo generated event are shown in (c) $\sim$ (g): $K^{*0}$ in (c), $\Lambda(1405)$ in (d), $\Lambda(1520)$ in (e), $\Lambda(1670)$ in (f), and non-resonant $K^+\pi^-$ production processes in (g), respectively.

color histogram: $K^{*0}$ production in green, $\Lambda(1405)$ in blue, $\Lambda(1520)$ in yellow, $\Lambda(1670)$ in pink, and non-resonant process in light blue.

We then selected the $K^{*0}$ events with a constraint on the $K^+\pi^-$ invariant mass by requiring the $|m_{K^+\pi^-} - m_{K^{*0}}| < 0.063$. Figure 4.18 represents the missing mass distributions with the mass cut. The number of event for included background (subtracted background) within $3\sigma$ of the $\Sigma^+$ and $K^{*0}$ peak is $203 \pm 14$ ($179 \pm 15$) for vertical polarization and $523 \pm 23$ ($473.5 \pm 24$) for horizontal polarization. Hyperon background yields in the $K^{*0}$ signal region were estimated to be $39.19 \pm 29.08$ for vertical polarization and $30.13 \pm 6.62$ for horizontal polarization.

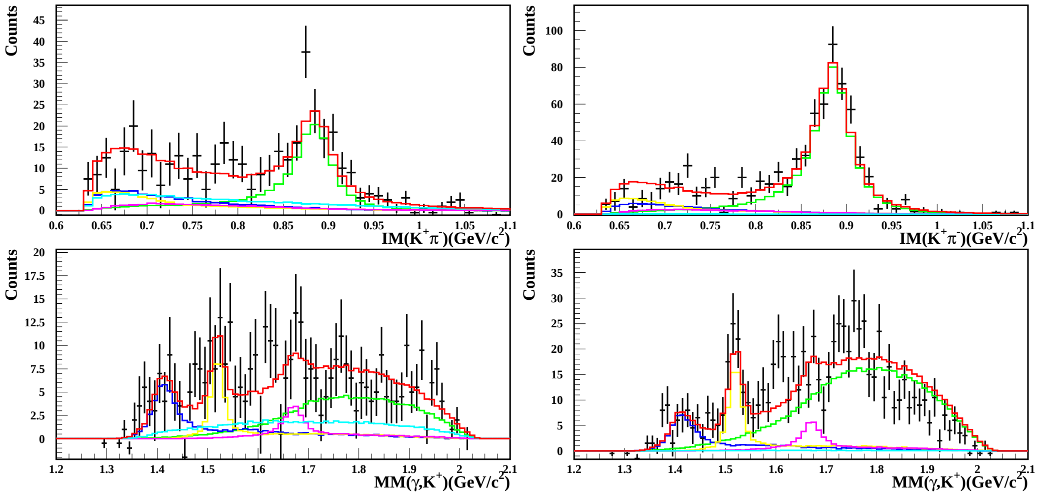

**Figure 4.17:** Template fit results are represented by different color lines in the $K^+\pi^-$ invariant mass (top) and the missing mass for $p(\gamma, K^+)X$ reaction (bottom), respectively. Left figures are for vertical polarization, while right ones for horizontal polarization.

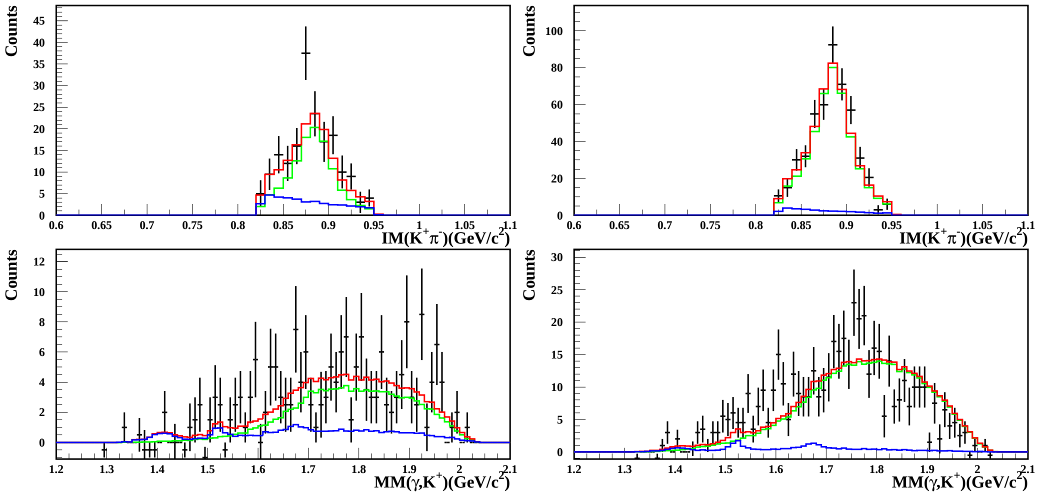

**Figure 4.18:** With the $K^{*0}$ mass cut the template fit results are represented.

## 4.6 Decay angular distribution

Finally 726 $K^{*0}$ events are survived IM cut and MM cut with sideband event. Figure 4.19, 4.20 show one-dimensional decay angular distributions of the $K^{*0}$ events in the GJ frame and the helicity frame, respectively. Overlaid red histograms show the side-band events. We used these angular distribution to measure the spin-density matrix elements.

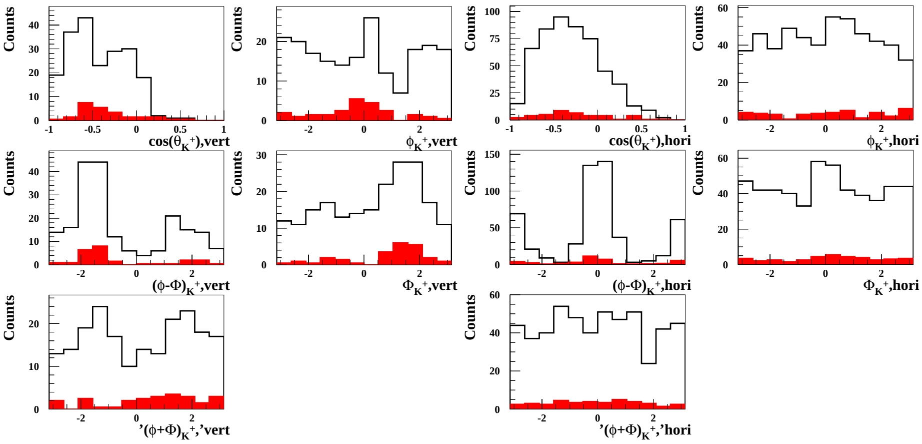

**Figure 4.19:** Decay angular distributions of $\cos\theta_{K^+}$, $\phi_{K^+}$, $(\phi-\Phi)_{K^+}$, $\Phi_{K^+}$ and $(\phi+\Phi)_{K^+}$ in the GJ frame for vertical polarization (left) and horizontal polarization (right), respectively. Overlaid red histograms denote side-band events.

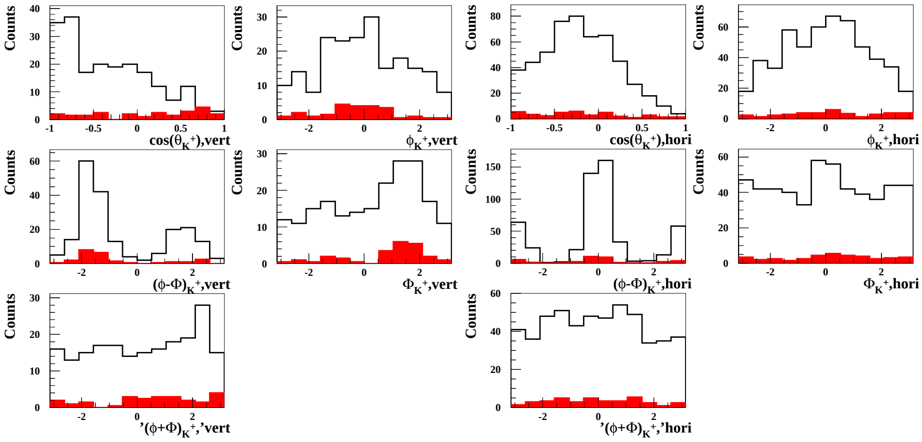

**Figure 4.20:** Decay angular distributions of $\cos\theta_{K^+}$, $\phi_{K^+}$, $(\phi-\Phi)_{K^+}$, $\Phi_{K^+}$ and $(\phi+\Phi)_{K^+}$ in the helicity frame for vertical polarization (left) and horizontal polarization (right), respectively. Overlaid red histograms denote side-band events.

However, the hyperon production couldn't separate out from $K^{*0}\Sigma^+$ events. The evaluated yield of hyperon is 71.30 ± 25.39 from Section 4.5, its amount is about 10% events still sizable.

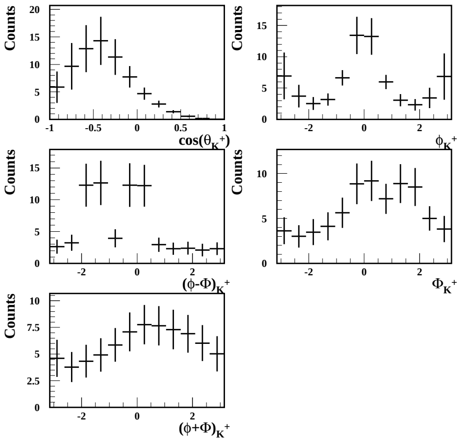

**Figure 4.21:** Decay angular distributions of $\cos\theta_{K^+}$, $\phi_{K^+}$, $(\phi-\Phi)_{K^+}$, $\Phi_{K^+}$ and $(\phi+\Phi)_{K^+}$ for hyperon yield in the GJ frame.

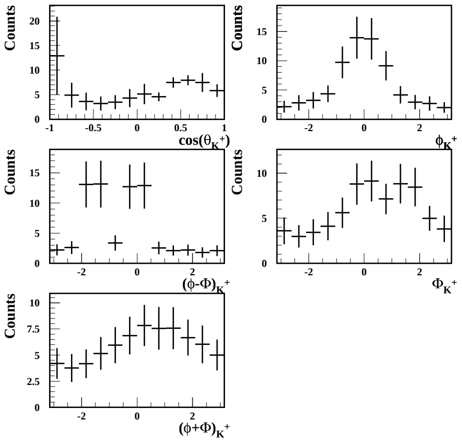

**Figure 4.22:** Decay angular distributions of $\cos\theta_{K^+}$, $\phi_{K^+}$, $(\phi-\Phi)_{K^+}$, $\Phi_{K^+}$ and $(\phi+\Phi)_{K^+}$ for hyperon yieldin the helicity frame.

we estimated the decay angular distribution for $K^+$ from the varying hyperons by using Monte-Carlo semple in $K^+\pi^-$ rest frame. Figure 4.21 (4.22) shows hyperon yield of each decay angular distribution for GJ (helicity) frame.

## 4.7 Unbinned extended maximum likelihood fit

We extracted spin-density matrix elements using the extended maximum likelihood (EML) estimator, was developed by Ref. [54, 55]. In the standard Maximum Likelihood the probability distribution is normalised to 1. But in the Extended Maximum Likelihood you relax this [56, 57]. The integral of the unnormalized probability density function $P$ represents the total number of events predicted $\bar{N}$. The likelihood for the whole dataset that has to include the Poission probability that you actually see $N$ events. The extended likelihood function is

$$\begin{aligned} L &= (\frac{\bar{N}^N e^{-\bar{N}}}{N!}) \cdot \sum_{i=1}^{N} P_i \\ &= (\frac{\bar{N}^N e^{-\bar{N}}}{N!}) \cdot \sum_{i=1}^{N} \frac{YW(\theta, \phi, \Phi; \hat{\rho})}{\int YW(\theta, \phi, \Phi; \hat{\rho}) d\cos\theta d\phi d\Phi} \end{aligned}$$

where, $Y$ is actual yield. The detector efficiency is not perfect at real data tacking. At that case, the probability density function can be modified as follows:

$$\begin{aligned} P_i &= \frac{YW(\theta, \phi, \Phi; \hat{\rho})}{\int YW(\theta, \phi, \Phi; \hat{\rho}) \eta(\theta, \phi) d\cos\theta d\phi d\Phi} \\ \bar{N} &= \int YW(\theta, \phi, \Phi; \hat{\rho}) \eta(\theta, \phi) d\cos\theta d\phi d\Phi = Y \cdot I(\hat{\rho}) \end{aligned}$$

where, $\eta(\theta, \phi)$ is the tacking into account the efficiency, $I(\hat{\rho})$ is normalization factor.

The decay angular distribution can be write as follows:

$$W(\theta, \phi, \Phi; \hat{\rho}) = \sum_{l,m} a_{lm}(\hat{\rho}) O^{lm}(\theta, \phi, \Phi)$$

where, the orthgonal conditions for each base are satisfied:

$$\int O^{*lm} O^{l'm'} d\cos\theta d\phi d\Phi = \delta_{ll'} \delta_{mm'}$$

and the coefficient for each basis $a_{lm}$ is

$$\int O^{*lm} W(\theta, \phi, \Phi; \hat{\rho}) d\cos\theta d\phi d\Phi = \sqrt{\frac{3}{4\pi}} a_{lm}(\hat{\rho})$$

The efficiency $\eta(\theta, \phi)$ is also represented by orthgonal basis as follows:

$$\eta(\theta, \phi) = \sum_{l,m} b_{lm} O^{lm}(\theta, \phi)$$

The $b_{lm}$ is the evalution of angular moments. We generated istropic MC events to extract angular moment, $b_{lm}$ and counting the accepted event.

$$\begin{aligned} b_{lm} &= \sqrt{\frac{3}{4\pi}}\int O_{lm}(\theta,\phi,\Phi)\eta(\theta,\phi)d\cos\theta d\phi d\Phi \\ &= \frac{1}{N_{gen}}\sum_{i=1}^{N_{acc}} O^{lm}(\theta,\phi,\Phi) \end{aligned}$$

The normalization factor $I(\hat{\rho})$ can be written as follows:

$$\begin{aligned} I(\hat{\rho}) &= \int W(\theta,\phi,\Phi;\hat{\rho})d\cos\theta d\phi d\Phi \\ &= \sum_{l,m} a_{lm}(\hat{\rho})b_{lm} \end{aligned}$$

The coefficient,$a_{lm}(\hat{\rho})$, and angular moment ,$b_{lm}$ by orthgonal basis are given in the [54]. $O^{lm}$ is orthogonal basis[1]

Table 4.3 shows the evaluated angular moments, $b_{lm}$.

| GJ frame | | | | | |
|---|---|---|---|---|---|
| $b_{lm}$ | $b_{01}$ | $b_{02}$ | $b_{03}$ | $b_{04}$ | $b_{11}$ |
| | 3.401×$10^{-3}$ | -2.413×$10^{-4}$ | 5.444×$10^{-4}$ | 6.474×$10^{-4}$ | 1.188×$10^{-5}$ |
| $b_{lm}$ | $b_{12}$ | $b_{13}$ | $b_{14}$ | $b_{21}$ | $b_{22}$ |
| | -5.129×$10^{-6}$ | 1.564×$10^{-5}$ | -3.360×$10^{-7}$ | 1.552×$10^{-7}$ | 7.697×$10^{-6}$ |
| **helicity frame** | | | | | |
| $b_{lm}$ | $b_{01}$ | $b_{02}$ | $b_{03}$ | $b_{04}$ | $b_{11}$ |
| | 3.401×$10^{-3}$ | 7.413×$10^{-4}$ | 5.679×$10^{-4}$ | 1.033×$10^{-4}$ | 1.188×$10^{-5}$ |
| $b_{lm}$ | $b_{12}$ | $b_{13}$ | $b_{14}$ | $b_{21}$ | $b_{22}$ |
| | 1.505×$10^{-6}$ | 4.630×$10^{-6}$ | -4.168×$10^{-6}$ | -5.299×$10^{-6}$ | 1.779×$10^{-6}$ |

**Table 4.3:** Angular moments $b_{lm}$ of acceptance of the $K^{*0}$ photoproduction.

Now, we minimized the extended likelihood function by CERNLIB MINUT package. The

---

[1] Evaluated orthogonal basis:

$O^{01} = \frac{1}{\sqrt{8\pi}}$, $O^{02} = \frac{1}{4\pi}\sqrt{\frac{5}{2}}(2-3\sin^2\theta)$,
$O^{03} = \frac{1}{4\pi}\sqrt{\frac{15}{2}}\sin(2\theta)\cos\phi$, $O^{04} = \frac{1}{4\pi}\sqrt{\frac{15}{2}}\sin^2\theta\cos(2\phi)$,
$O^{11} = \frac{1}{2\pi}\cos(2\Phi)$, $O^{12} = \frac{1}{4\pi}\sqrt{5}(2-3\sin^2\theta)\cos(2\Phi)$,
$O^{13} = \frac{1}{4\pi}\sqrt{15}\sin(2\theta)\cos\phi\cos(2\Phi)$, $O^{14} = \frac{1}{4\pi}\sqrt{15}\sin^2\theta\cos(2\phi)\cos(2\Phi)$,
$O^{21} = \frac{1}{4\pi}\sqrt{15}\sin(2\theta)\sin\phi\sin(2\Phi)$, $O^{22} = \frac{-1}{4\pi}\sqrt{15}\sin^2\theta\sin(2\phi)\sin(2\Phi)$

minimized function is as follows:

$$\begin{aligned} -\ln L(\bar{\rho},\bar{N}) &= \sum_{i=1}^{N} \ln YW(\theta,\phi,\Phi;\hat{\rho}) + \bar{N} \\ &= \sum_{i=1}^{N} \ln \bar{N}W(\theta,\phi,\Phi;\hat{\rho})/I(\hat{\rho}) + \bar{N} \end{aligned}$$

In the EML fitting, we use MINOS option to estimate of the error of each fitting parameter.

In the real data, we can see background events in the signal region. And these spin density matrix elements are different signal and background. We defined $R$ parameter for ratio of signal to signal+background. Then we can re-write extended function as follows:

$$\begin{aligned} -\ln L(\bar{\rho}_{\rm s},\bar{\rho}_{\rm b},\bar{N}) &= \sum_{i=1}^{N} \ln \bar{N}\Big\{R\frac{W(\theta,\phi,\Phi;\hat{\rho}_{\rm s})}{I(\hat{\rho}_{\rm s})} \\ &+ (1-R)\frac{W(\theta,\phi,\Phi;\hat{\rho}_{\rm b})}{I(\hat{\rho}_{\rm b})}\Big\} + \bar{N} \end{aligned}$$

We needed to ensure the EML fitting quality. First fitting status can be output by MINUT package. We can see four fitting status by MINUT package. The meaning of 0 is “Not calculated at all”.

1 is ”Diagonal approximation only, not accurate”

2 is ”Full matrix, but forced positive-definite”

3 is ”Full accurate covariance matrix”

We selected that the fitting status must be equal to 3, the meaning is “full accurate covariance matrix” which is the indication of normal convergence. Secondly, we can compared with the input total number of events and fitting parameter of predicted $\bar{N}$. Finally we can get some spin density matrix elements by the one-dimensional decay angular distribution of $\cos\theta_{K^+}$, $\phi_{K^+}$, $(\phi-\Phi)_{K^+}$ and $\Phi_{K^+}$. The fitting parameters are consisted with results of $\hat{\rho}$ by EML fitting.

We studied a reliability of the EML fit with MC data sets. First, we scanned each SDM parameter in a proper range with all zeros for the other parameters, as listed in Table 4.4. We generated 30 sets of MC ntuples, 15 sets for each polarization with 0.25 M $K^{*0}$ events for each set. Of the 0.25 M generated $K^{*0}$ events 750 events survived and were accepted for the EML fit test. Figures 4.23 and 4.24 show the comparison between the input values and the output EML fit results in the GJ frame and helicity frame, respectively. The error bars quoted in the plot are the root-mean-square of the residual distribution from the mean of fit results.The red lines indicate a good agreement of reliability. Commonly, the reliability is good for the boundary of physically physically allowed region. In the near the boundary, the agreement is fine within error bar.

| SDM parameters | Input values of SDM elements |
|---|---|
| $\rho^0_{00}$ | 0.0, 0.1, 0.2, 0.3, 0.4, 0.5 and all the other $\rho = 0$ |
| $Re\rho^0_{10}$ | -0.5, -0.3, -0.1, 0.1, 0.3, 0.5 and all the other $\rho = 0$ |
| $\rho^0_{1-1}$ | -0.5, -0.3, -0.1, 0.1, 0.3, 0.5 and all the other $\rho = 0$ |
| $\rho^1_{11}$ | -1.0, -0.6, -0.2, 0.2, 0.6, 1.0 and all the other $\rho = 0$ |
| $\rho^1_{00}$ | -0.5, -0.3, -0.1, 0.1, 0.3, 0.5 and all the other $\rho = 0$ |
| $Re\rho^1_{10}$ | -0.5, -0.3, -0.1, 0.1, 0.3, 0.5 and all the other $\rho = 0$ |
| $\rho^1_{1-1}$ | -0.5, -0.3, -0.1, 0.1, 0.3, 0.5 and all the other $\rho = 0$ |
| $Im\rho^2_{10}$ | -0.5, -0.3, -0.1, 0.1, 0.3, 0.5 and all the other $\rho = 0$ |
| $Im\rho^2_{1-1}$ | -0.5, -0.3, -0.1, 0.1, 0.3, 0.5 and all the other $\rho = 0$ |

**Table 4.4:** Parameter sets for the Monte-Carlo test.

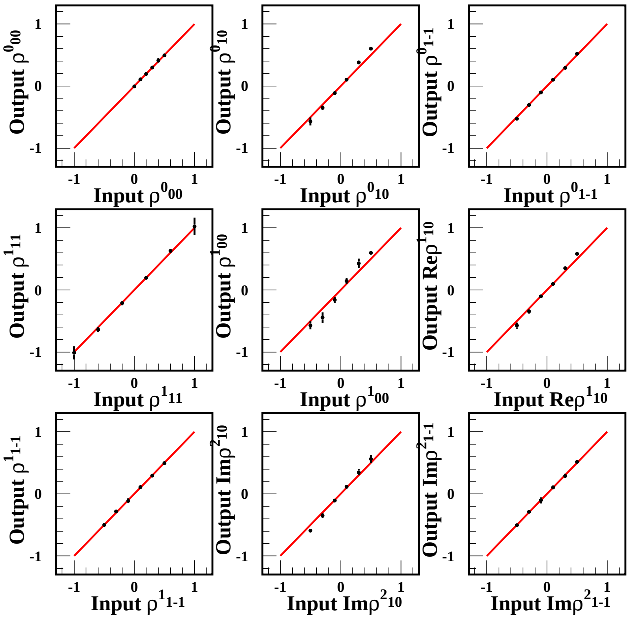

**Figure 4.23:** Comparison between the generated spin-density matrix elements and the fit results with 0.25 M MC events in the GJ frame.

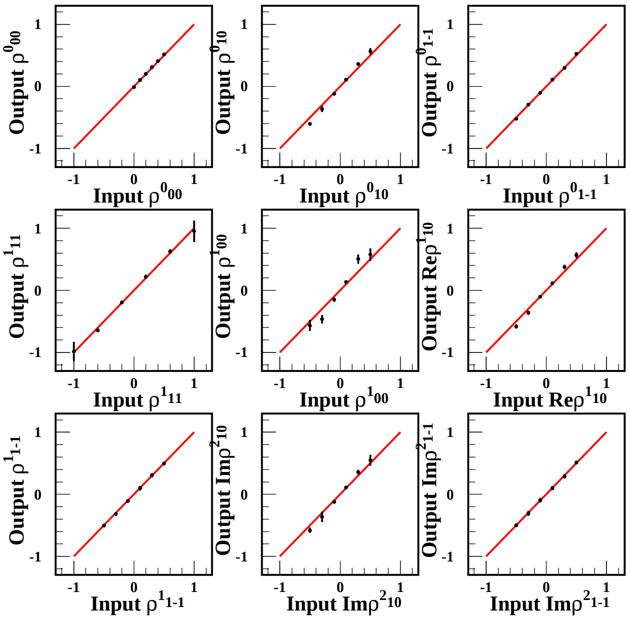

**Figure 4.24:** Comparison between the generated spin-density matrix elements and the fit results with 0.25 M MC events in the helicity frame.

## 4.8 Spin density matrix for $K^{*0}$

We performed the unbinned EML fit to estimate spin-density matrix elements with side-band background subtraction. There are 19 parameters for the EML fit with background subtraction. Both the signal and the side-band background have 9 parameters for the SDM elements, $\hat{\rho}_s and \hat{\rho}_b$, respectively. The remaining one parameter is the number of events in the $K^{*0}$ signal region. We first estimated the ratio of the number of signal events to the sum of signal and background events in the $K^{*0}$ signal region, which was found to be $R = \frac{Signal+BG-(BG1+BG2)/2}{Signal+BG} = 0.913$ with selection $K^{*0}$ peak, where $BG1$ and $BG2$ denote side-band events as shown in Figure 4.3.

We have taken the side-band events to estimate spin-density matrix elements for background in the regions indicated by blue and red arrows in Figure 4.25. The width of both side-band region are 4.5 $\sigma$, which $\sigma$ is the with of the $\Sigma^+$ peak, due to the error of EML estimator is decreased in high statistic.

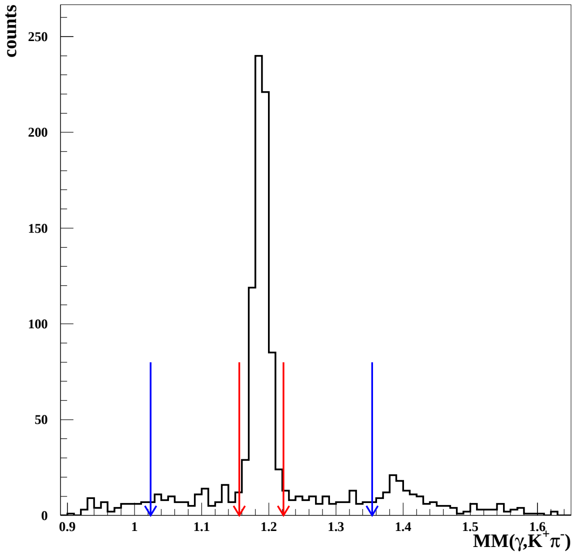

**Figure 4.25:** Event selection for EML fitting with background subtraction. The signal selection is between two red arrows, the background selection is between two blue arrows.

We estimated spin-density matrix elements for background events taken from the side-band regions. Note that we used 10 parameters to estimate the spin-density matrix elements for background by using unbinned EML fit without background subtraction method. The unbinned EML fit results for side-band regions are listed in Table 4.5. Note that we used minos error in the GJ frame, while helicity frame used the parabolic error due to the fit status has been got ”3” by using the above condition.

| GJ frame | | helicity frame | |
|---|---|---|---|
| $\hat{\rho}_\mathrm{b}$ | Unbinned EML fit | $\hat{\rho}_\mathrm{b}$ | Unbinned EML fit |
| $\rho^0_{00}$ | 0.064 $^{+0.065}_{-0.057}$ | $\rho^0_{00}$ | 0.152 $\pm$ 0.052 |
| $\rho^0_{10}$ | 0.148 $^{+0.033}_{-0.034}$ | $\rho^0_{10}$ | -0.141 $\pm$ 0.033 |
| $\rho^0_{1-1}$ | -0.027 $^{+0.063}_{-0.063}$ | $\rho^0_{1-1}$ | 0.008 $\pm$ 0.069 |
| $\rho^1_{11}$ | 0.084 $^{+0.083}_{-0.084}$ | $\rho^1_{11}$ | -0.019 $\pm$ 0.082 |
| $\rho^1_{00}$ | -0.043 $^{+0.088}_{-0.086}$ | $\rho^1_{00}$ | 0.127 $\pm$ 0.076 |
| $\rho^1_{10}$ | -0.134 $^{+0.059}_{-0.057}$ | $\rho^1_{10}$ | -0.057 $\pm$ 0.052 |
| $\rho^1_{1-1}$ | 0.055 $^{+0.090}_{-0.094}$ | $\rho^1_{1-1}$ | 0.170 $\pm$ 0.106 |
| $\rho^2_{10}$ | 0.142 $^{+0.067}_{-0.070}$ | $\rho^2_{10}$ | 0.052 $\pm$ 0.080 |
| $\rho^2_{1-1}$ | -0.030 $^{+0.102}_{-0.102}$ | $\rho^2_{1-1}$ | -0.196 $\pm$ 0.101 |
| $\bar{N}$ | 228.99 $^{+20.09}_{-20.73}$ | $\bar{N}$ | 229.00 $\pm$ 21.40 |

**Table 4.5:** Spin-density matrix elements from the EML fit for side-band background events.

We used two different method to estimate the spin-density matrix elements. First, we performed the unbinned EML fit to the $K^{*0}$ events in the signal region with the signal-to-background ratio fixed. It should be noted that the boundaries of fit parameters for the background events are set to $\pm$ 1 $\sigma$ error from the mean value of the fit with side-band background events only (Fixed fit boundaries). Second, we estimated the spin-density matrix by only using mean value for background spin-density matrix. Therefore, we only got ten parameters, nine parameters are spin-density matrix and other one parameter is the estimated events, by unbinned EML fit (Fixed mean of BG). The fit results are summarized in Table 4.6. In the case of the fixed fit boundaries for BG and the fixed mean of BG have a simal value for the both decay angle. In the case of helicity conservation, the decay asymmetry $\rho^1_{1-1}$ reflects the relative contributions of natural parity ($\rho^1_{1-1}$ = 0.5) and unnatural parity ($\rho^1_{1-1}$ = -0.5) processes. The $\rho^1_{1-1}$ has similar value for both frame and closes to 0.5, it shows natural parity exchange dominent. The parity spin asymmetry, $P_\sigma$, is defined as

$$P_\sigma \quad = \quad 2\rho^1_{1-1} - \rho^1_{00}.$$

The parity spin asymmetry was estimated to be 0.78 $\pm$ 0.15 in GJ frame and 0.76 $\pm$ 0.12 in helicity frame for the fixed fit range of BG. In the case of fixed mean of BG, the parity asymmetry was estimated to be 0.71 $\pm$ 0.11 in GJ frame and 0.77 $\pm$ 0.12 in helicity frame, respectively. Such a large positive value supports that a natural-parity exchange is dominant in forward angles for $K^{*0}\Sigma^+$ photoproduction. This value is in a good agreement with the value obtained from the fit without background subtraction in Appendix H. With the 19 SDM elements obtained from the fit, we generated high-statistics simulation data to test how well the EML fit results reproduce real data.

| GJ frame | | | | | |
|---|---|---|---|---|---|
| Fixed fit boundaries for BG | | | | Fixed mean of BG | |
| $\hat{\rho}_{\mathrm{s}}$ | Unbinned EML fit | $\hat{\rho}_{\mathrm{b}}$ | Unbinned EML fit | $\hat{\rho}_{\mathrm{s}}$ | Unbinned EML fit |
| $\rho^0_{00}$ | 0.155 ± 0.051 | $\rho^0_{00}$ | 0.128 ± 0.095 | $\rho^0_{00}$ | 0.153 ± 0.034 |
| $\rho^0_{10}$ | 0.108 ± 0.068 | $\rho^0_{10}$ | 0.180 ± 0.049 | $\rho^0_{10}$ | 0.114 ± 0.018 |
| $\rho^0_{1-1}$ | 0.090 ± 0.191 | $\rho^0_{1-1}$ | -0.090 ± 0.089 | $\rho^0_{1-1}$ | 0.075 ± 0.032 |
| $\rho^1_{11}$ | 0.031 ± 0.052 | $\rho^1_{11}$ | 0.167 ± 0.120 | $\rho^1_{11}$ | 0.043 ± 0.44 |
| $\rho^1_{00}$ | -0.140 ± 0.074 | $\rho^1_{00}$ | 0.045 ± 0.148 | $\rho^1_{00}$ | -0.124 ± 0.058 |
| $\rho^1_{10}$ | -0.088 ± 0.039 | $\rho^1_{10}$ | -0.191 ± 0.080 | $\rho^1_{10}$ | -0.097 ± 0.030 |
| $\rho^1_{1-1}$ | 0.322 ± 0.068 | $\rho^1_{1-1}$ | -0.038 ± 0.135 | $\rho^1_{1-1}$ | 0.291 ± 0.049 |
| $\rho^2_{10}$ | 0.127 ± 0.051 | $\rho^2_{10}$ | 0.072 ± 0.097 | $\rho^2_{10}$ | 0.123 ± 0.034 |
| $\rho^2_{1-1}$ | -0.357 ± 0.063 | $\rho^2_{1-1}$ | 0.073± 0.143 | $\rho^2_{1-1}$ | -0.321± 0.046 |
| $\bar{N}$ | 726.00 ± 38.10 | | | $\bar{N}$ | 726.00 ± 38.06 |
| $P_\sigma$ | 0.784 ± 0.154 | | | $P_\sigma$ | 0.707 ± 0.113 |

| Helicity frame | | | | | |
|---|---|---|---|---|---|
| Fixed fit boundaries for BG | | | | Fixed mean of BG | |
| $\hat{\rho}_{\mathrm{s}}$ | Unbinned EML fit | $\hat{\rho}_{\mathrm{b}}$ | Unbinned EML fit | $\hat{\rho}_{\mathrm{s}}$ | Unbinned EML fit |
| $\rho^0_{00}$ | 0.082 ± 0.025 | $\rho^0_{00}$ | 0.204 ± 0.074 | $\rho^0_{00}$ | 0.086 ± 0.025 |
| $\rho^0_{10}$ | -0.023 ± 0.021 | $\rho^0_{10}$ | -0.174 ± 0.048 | $\rho^0_{10}$ | -0.026 ± 0.021 |
| $\rho^0_{1-1}$ | 0.037 ± 0.040 | $\rho^0_{1-1}$ | 0.036 ± 0.090 | $\rho^0_{1-1}$ | 0.039 ± 0.040 |
| $\rho^1_{11}$ | -0.016 ± 0.049 | $\rho^1_{11}$ | 0.064 ± 0.117 | $\rho^1_{11}$ | -0.008 ± 0.49 |
| $\rho^1_{00}$ | -0.049 ± 0.044 | $\rho^1_{00}$ | 0.203 ± 0.107 | $\rho^1_{00}$ | -0.042 ± 0.044 |
| $\rho^1_{10}$ | 0.000 ± 0.034 | $\rho^1_{10}$ | -0.005 ± 0.074 | $\rho^1_{10}$ | 0.004 ± 0.034 |
| $\rho^1_{1-1}$ | 0.355 ± 0.057 | $\rho^1_{1-1}$ | 0.275 ± 0.154 | $\rho^1_{1-1}$ | 0.355 ± 0.057 |
| $\rho^2_{10}$ | -0.038 ± 0.035 | $\rho^2_{10}$ | 0.113 ± 0.081 | $\rho^2_{10}$ | -0.038 ± 0.034 |
| $\rho^2_{1-1}$ | -0.395 ± 0.051 | $\rho^2_{1-1}$ | -0.094 ± 0.144 | $\rho^2_{1-1}$ | -0.395± 0.051 |
| $\bar{N}$ | 726.00 ± 38.02 | | | $\bar{N}$ | 726.02 ± 38.06 |
| $P_\sigma$ | 0.758 ± 0.123 | | | $P_\sigma$ | 0.772 ± 0.124 |

**Table 4.6:** Spin-density matrix elements for signal and background events from the EML fit by using the fixed fit boundaries for BG method and the fixed mean of BG. Top parts show results in GJ frame, while bottom parts show results in helicity frame, respectively.

We checked the reliability of the measured spin-density matrix elements. First, we just compared with the kinematic variables with the Monte-Carlo and the real data. We generated each ntuple set with 50 M events, 25 M events are the vertical polarization and 25 M events are the horizontal polarization. Figure 4.26 shows distributions for various kinematic variables such as momentum transfer squared $t$, incident photon energy $E_\gamma$, and momentum distributions for $K^{*0}$, $K^+$ and $\pi^-$ by using the measured spin-density matrix elements for the fixed fit boundaries for BG in GJ frame. These spectra were normalized by the sum of total area to be 1. Left ones are for vertical polarization and right ones for horizontal polarization, respectively. The kinematic variables show a good agreement.

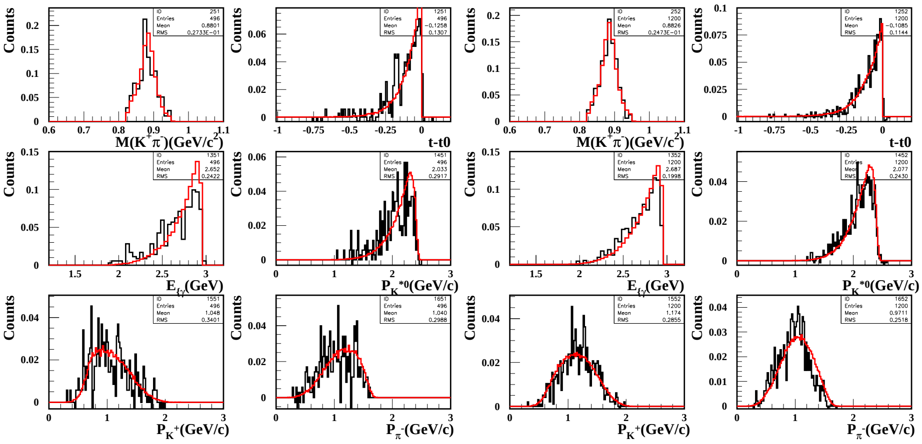

**Figure 4.26:** Distributions of kinematic variables compared with Monte-Carlo simulation results as overlaid lines. Left and right panels indicate the vertical and the horizontal polarization cases.

And also, We can measure these spin-density matrix elements, $\rho^0_{00}$, $Re\rho^0_{1-1}$, $\rho^1_{1-1} - Im\rho^2_{1-1}$, $2\rho^1_{11} + \rho^1_{00}$, and $\rho^1_{1-1} + Im\rho^2_{1-1}$, by using one-dimensional decay angular distribution in Section 1.5. We compared with the unbinned EML fit results and the one-dimensional distribution. First, we measured the acceptance for five decay angular distribution by using Monte-Carlo simulation with the measured spin-density matrix elements for the fixed fit bounndaries for BG and the fixed meas of BG in GJ frame and helicity frame.

Acceptance for five decay angular distributions show in Figure 4.27 for GJ frame and Figure 4.28 for helicity frame, respectively. Figure 4.29 and 4.30 shows decay angular distribution after acceptance correction. The normalized decay angular distributions are fitted with the functions as represented in Section 1.5. Normalization factors are given by

$$A(x) = \sum_{i=1}^{N_{bin}} n_i(x)/N_{bin},$$

where $x$ are the angle variables such as $\cos\theta_{K^+}$, $\phi_{K^+}$, $(\phi-\Phi)_{K^+}$, $\Phi_{K^+}$ and $(\phi+\Phi)_{K^+}$. $n_i$ denotes the number of events in the $i^{th}$ bin. We estimated the SDM elements with bin sizes yielding 12 bins for each distribution. The normalized decay angular distributions in terms of $\cos\theta_{K^+}$, $\phi_{K^+}$,

$(\phi - \Phi)_{K^+}$, $\Phi_{K^+}$, and $(\phi + \Phi)_{K^+}$ with SDM elements for fixed fit boundaries for BG (a) and fixed mean of BG (b) in GJ frame as shown in Figure 4.31 (top). Figure 4.31 (bottom) shows 1-dimensional distributions with SDM elements for fixed fit boundaries for BG (c) and fixed mean of BG (d) in helicity frame, respectively. Overlaid red-color lines show the fit results and the fit results are listed in Table 4.7. The difference with the results of unbinned EML fit and the results $\chi^2$ fit has almost agreement within error bar.

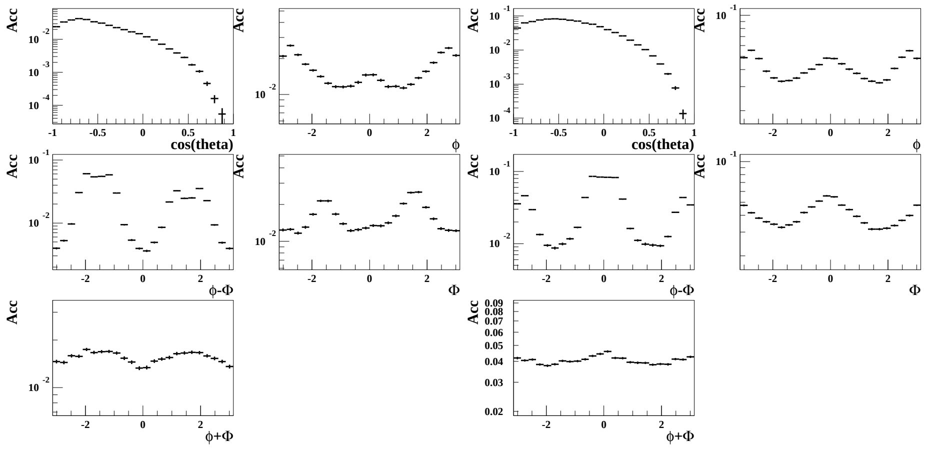

(a) Fixed fit boundaries, Vert.

(b) Fixed fit boundaries, Hori.

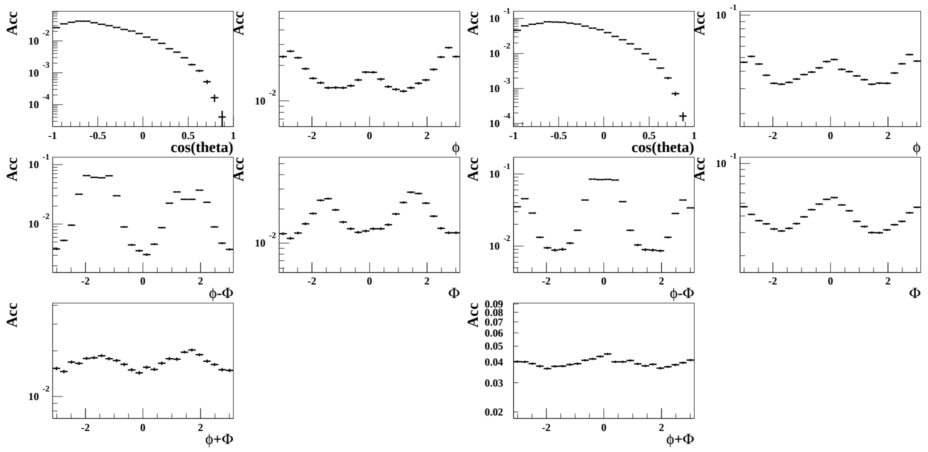

(c) Fixed mean, Vert.

(d) Fixed mean, Hori.

**Figure 4.27:** Acceptance functions for detecting $K^{*0}\Sigma^+$ events with SDM elements for fixed fit boundaries for BG (top) and fixed mean of BG (bottom) in GJ frame. Left panels are vertical polarization and right panels are horizontal polarization, respectively.

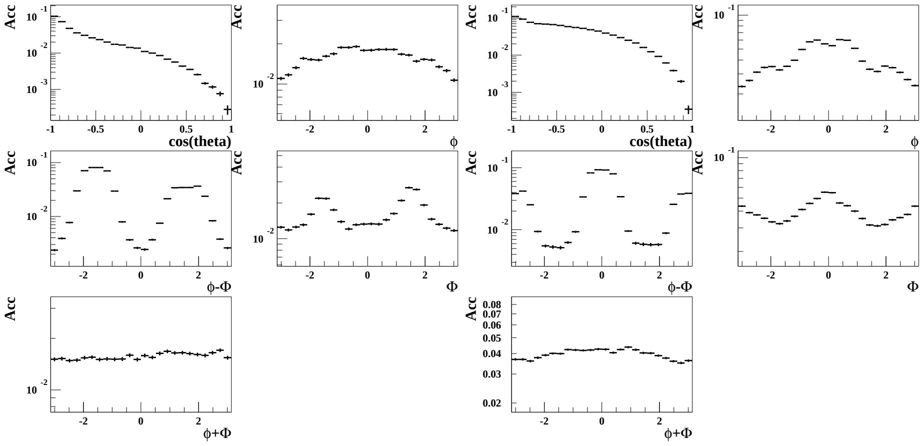

(a) Fixed fit boundaries, Vert. (b) Fixed fit boundaries, Hori.

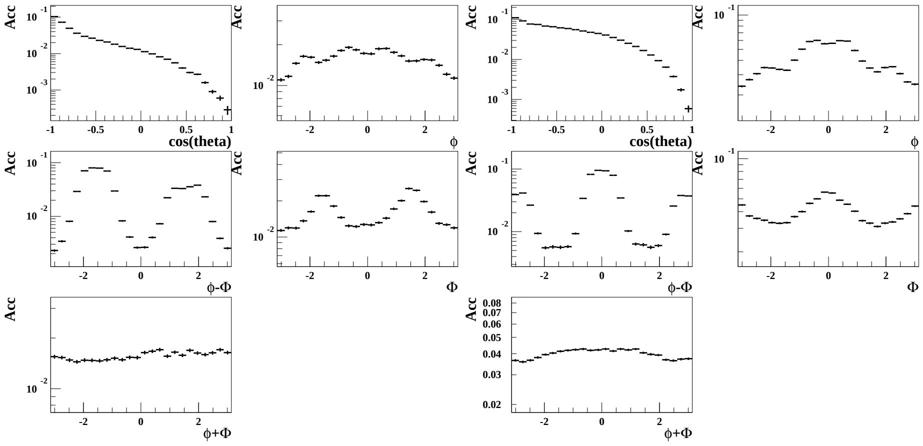

(c) Fixed mean, Vert. (d) Fixed mean, Hori.

**Figure 4.28:** Acceptance functions for detecting $K^{*0}\Sigma^{+}$ events with SDM elements for fixed fit boundaries for BG (top) and fixed mean of BG (bottom) in helicity frame. Left panels are vertical polarization and right panels are horizontal polarization, respectively.

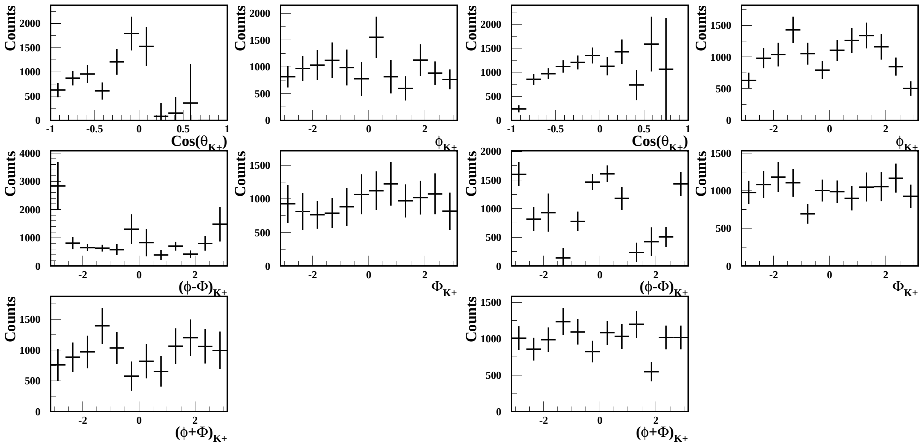

(a) Fixed fit boundaries, Vert.

(b) Fixed fit boundaries, Hori.

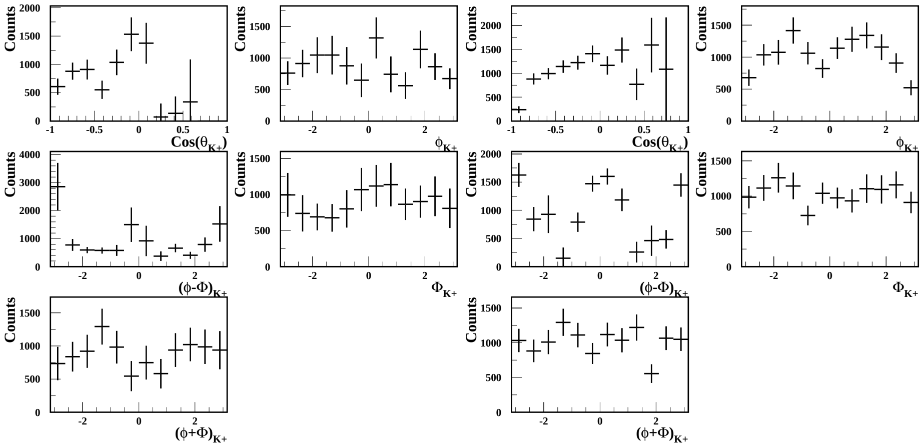

(c) Fixed mean, Vert.

(d) Fixed mean, Hori.

**Figure 4.29:** The decay angular distributions in terms of $\cos\theta_{K^+}$, $\phi_{K^+}$, $(\phi-\Phi)_{K^+}$, $\Phi_{K^+}$, and $(\phi+\Phi)_{K^+}$ after acceptance correction with different SDM elements for fixed fit boundaries for BG and fixed mean of BG in GJ frame. The vertical and the horizontal polarization data are represented in left and right panels, respectively.

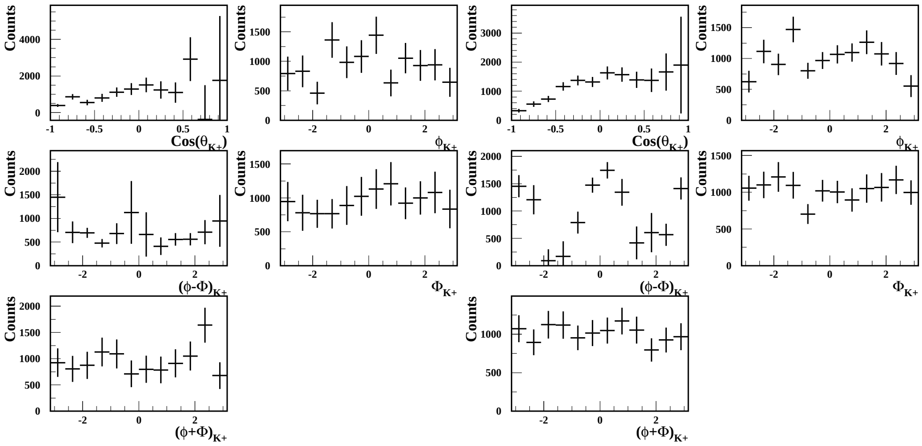

(a) Fixed fit boundaries, Vert.

(b) Fixed fit boundaries, Hori.

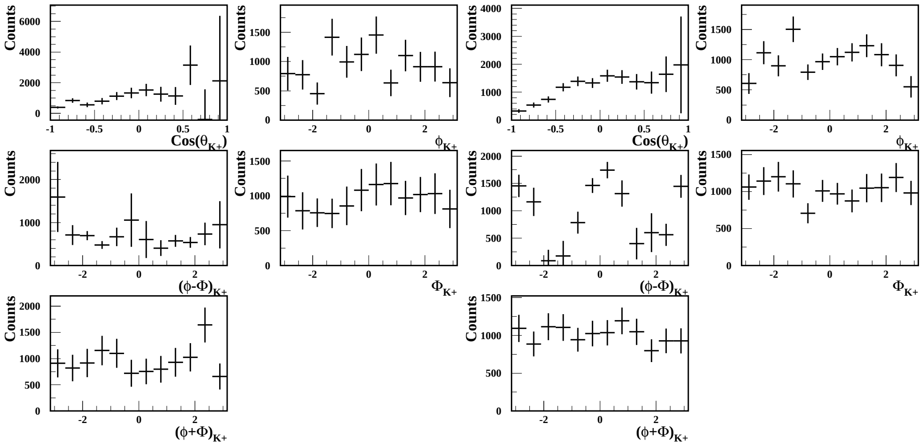

(c) Fixed mean, Vert.

(d) Fixed mean, Hori.

**Figure 4.30:** The decay angular distributions in terms of $\cos\theta_{K^+}$, $\phi_{K^+}$, $(\phi-\Phi)_{K^+}$, $\Phi_{K^+}$, and $(\phi+\Phi)_{K^+}$ after acceptance correction with different SDM elements for fixed fit boundaries for BG and fixed mean of BG in helicity frame. The vertical and the horizontal polarization data are represented in left and right panels, respectively.

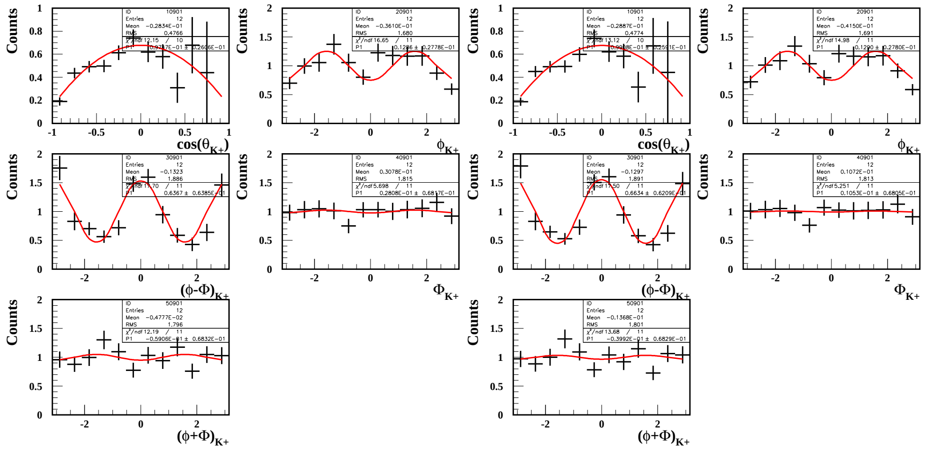

(a) Fixed fit boundaries in GJ frame (b) Fixed mean in GJ frame

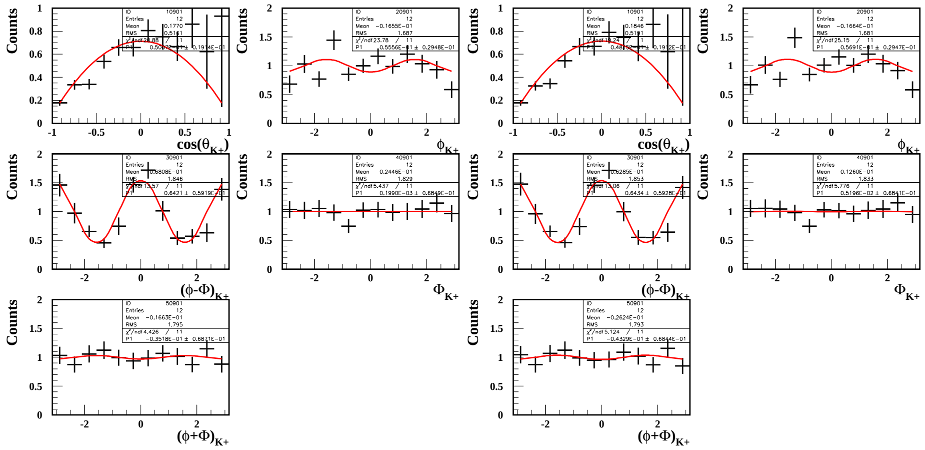

(c) Fixed fit boundaries in helicity frame (d) Fixed mean in helicity frame

**Figure 4.31:** The normalized decay angular distributions in terms of $\cos\theta_{K+}$, $\phi_{K+}$, $(\phi-\Phi)_{K+}$, $\Phi_{K+}$, and $(\phi+\Phi)_{K+}$ with SDM elements for fixed fit boundaries for BG (a) and fixed mean of BG (b) in GJ frame. (C) and (d) denote 1-dimensional distributions with SDM elements for fixed fit boundaries for BG and fixed mean of BG in helicity frame, respectively. Fit results are represented as overlaid red curves.

<table>
<tr><th colspan="4">Fixed fit boundaries for BG in GJ frame</th></tr>
<tr><th>$\hat{\rho}_s$</th><th>Unbinned EML fit</th><th>$\chi^2$-fit</th><th>$\chi^2/ndf$</th></tr>
<tr><td>$\rho^0_{00}$</td><td>0.156 ± 0.051</td><td>0.097 ± 0.026</td><td>12.15/10</td></tr>
<tr><td>$Re\rho^0_{1-1}$</td><td>0.090 ± 0.191</td><td>0.129 ± 0.028</td><td>16.65/11</td></tr>
<tr><td>$\rho^1_{1-1} - Im\rho^2_{1-1}$</td><td>0.679 ± 0.092</td><td>0.637 ± 0.064</td><td>17.70/11</td></tr>
<tr><td>$2\rho^1_{11} + \rho^1_{00}$</td><td>-0.078 ± 0.128</td><td>0.028 ± 0.068</td><td>5.70/11</td></tr>
<tr><td>$\rho^1_{1-1} + Im\rho^2_{1-1}$</td><td>-0.036 ± 0.092</td><td>-0.059 ± -0.068</td><td>12.19/11</td></tr>
<tr><th colspan="4">Fixed mean of BG in GJ frame</th></tr>
<tr><th>$\hat{\rho}_s$</th><th>Unbinned EML fit</th><th>$\chi^2$-fit</th><th>$\chi^2/ndf$</th></tr>
<tr><td>$\rho^0_{00}$</td><td>0.153 ± 0.034</td><td>0.099 ± 0.026</td><td>13.12/10</td></tr>
<tr><td>$Re\rho^0_{1-1}$</td><td>0.075 ± 0.032</td><td>0.129 ± 0.028</td><td>14.98/11</td></tr>
<tr><td>$\rho^1_{1-1} - Im\rho^2_{1-1}$</td><td>0.612 ± 0.067</td><td>0.663 ± 0.062</td><td>17.50/11</td></tr>
<tr><td>$2\rho^1_{11} + \rho^1_{00}$</td><td>-0.39 ± 0.105</td><td>0.011 ± 0.068</td><td>5.25/11</td></tr>
<tr><td>$\rho^1_{1-1} + Im\rho^2_{1-1}$</td><td>-0.029 ± 0.067</td><td>-0.040 ± 0.068</td><td>13.68/11</td></tr>
<tr><th colspan="4">Fixed fit boundaries for BG in helicity frame</th></tr>
<tr><th>$\hat{\rho}_s$</th><th>Unbinned EML fit</th><th>$\chi^2$-fit</th><th>$\chi^2/ndf$</th></tr>
<tr><td>$\rho^0_{00}$</td><td>0.082 ± 0.026</td><td>0.050 ± 0.019</td><td>20.88/11</td></tr>
<tr><td>$Re\rho^0_{1-1}$</td><td>0.037 ± 0.040</td><td>0.056 ± 0.029</td><td>23.78/11</td></tr>
<tr><td>$\rho^1_{1-1} - Im\rho^2_{1-1}$</td><td>0.750 ± 0.077</td><td>0.642 ± 0.059</td><td>13.57/11</td></tr>
<tr><td>$2\rho^1_{11} + \rho^1_{00}$</td><td>-0.080 ± 0.108</td><td>0.020 ± 0.068</td><td>5.44/11</td></tr>
<tr><td>$\rho^1_{1-1} + Im\rho^2_{1-1}$</td><td>-0.041 ± 0.077</td><td>-0.035 ± 0.069</td><td>4.43/11</td></tr>
<tr><th colspan="4">Fixed mean of BG in helicity frame</th></tr>
<tr><th>$\hat{\rho}_s$</th><th>Unbinned EML fit</th><th>$\chi^2$-fit</th><th>$\chi^2/ndf$</th></tr>
<tr><td>$\rho^0_{00}$</td><td>0.086 ± 0.026</td><td>0.048 ± 0.019</td><td>19.24/11</td></tr>
<tr><td>$Re\rho^0_{1-1}$</td><td>0.039 ± 0.040</td><td>0.057 ± 0.029</td><td>25.15/11</td></tr>
<tr><td>$\rho^1_{1-1} - Im\rho^2_{1-1}$</td><td>0.752 ± 0.077</td><td>0.643 ± 0.059</td><td>13.06/11</td></tr>
<tr><td>$2\rho^1_{11} + \rho^1_{00}$</td><td>-0.059 ± 0.108</td><td>0.052 ± 0.068</td><td>5.78/11</td></tr>
<tr><td>$\rho^1_{1-1} + Im\rho^2_{1-1}$</td><td>-0.022 ± 0.077</td><td>-0.043 ± 0.068</td><td>5.12/11</td></tr>
</table>

**Table 4.7:** Comparison between spin density matrix elements estimated from the unbinned EML fit and from the $\chi^2$ fit with side-band subtraction.

## 4.9 Uncertainties from the EML fit

We are now in a position to test if the EML estimator is consistent and also unbiased. We first tested a convergence of the parameters for the EML fit. We implemented the estimated SDM elements in the simulation. We then re-estimated the SDM elements from the MC data with varying statistics.

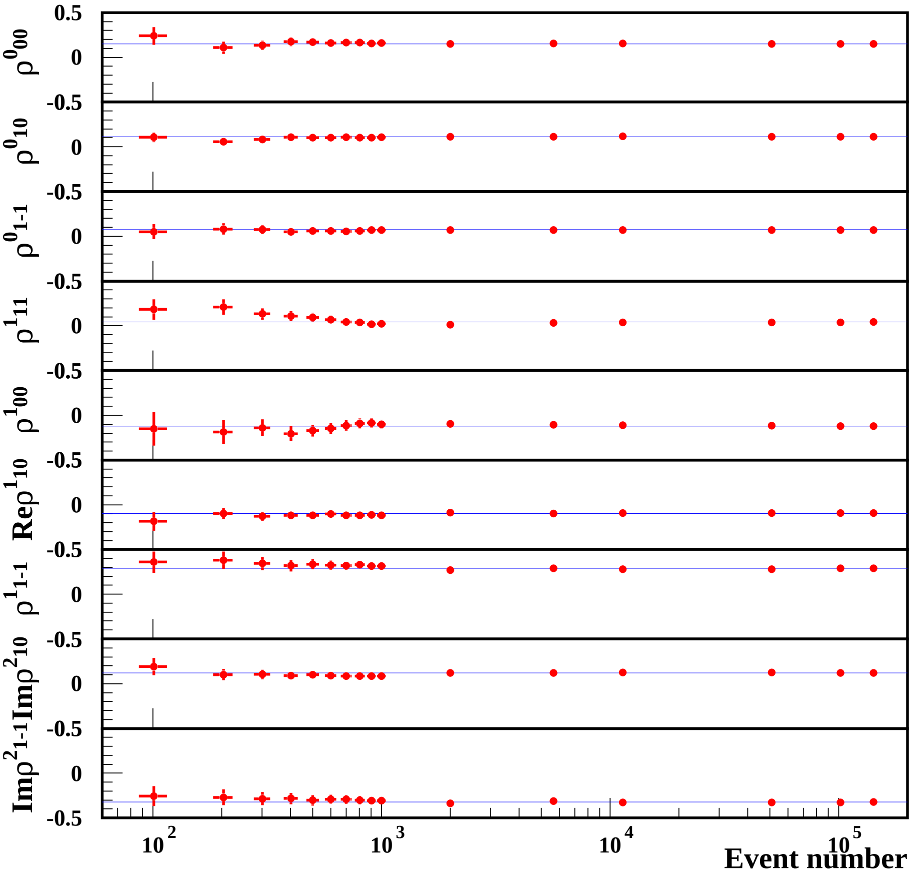

**Figure 4.32:** Results of EML fit depends on the input number of events. Blue lines show the input SDM elements.

Figure 4.32 shows a variation of each parameter in terms of the number of MC events. The blue lines indicate input SDM elements. The estimated the SDM elements converge on the input SDM elements to increase the statistic. More over, if the statistic was more than 700 events, the estimator is almost consistent. It turns out that the EML fit estimator is consistent

$$\lim_{N\to\infty} \hat{\rho} = \rho.$$

We also re-estimated the SDM elements from the MC data with the same statistics as the real data as shown in Figure 4.34. We performed this test with tens of MC data sets. We then compared the mean value of the SDM elements with the one from the fit with high-statistics MC data as listed in Table 4.8. The difference between the input SDM elements and the output SDM elements by EML fit is small. It proves that $<\hat{\rho}> = \rho$, say, the EML estimator is unbiased.

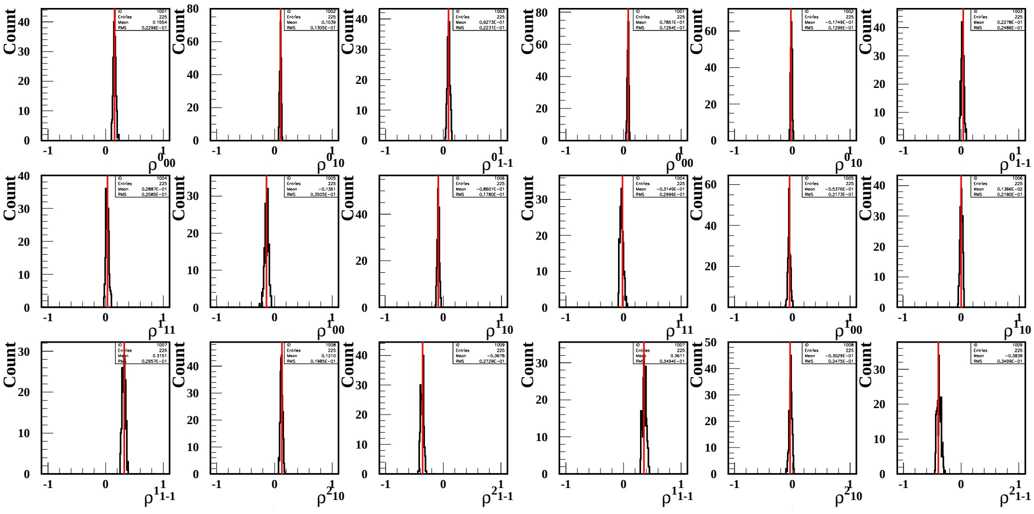

(a) GJ frame (b) helicity frame

**Figure 4.33:** Unbinned EML fit result with MC netuple set by using the measured spin-density matrix elements.

| | GJ frame | | | helicity frame | | |
|---|---|---|---|---|---|---|
| $\hat{\rho}$ | Input $\hat{\rho}$ | Mean(MC) | RMS(MC) | Input | Mean(MC) | RMS(MC) |
| $\rho^0_{00}$ | 0.155 | 0.155 | 0.023 | 0.082 | 0.079 | 0.013 |
| $\rho^0_{10}$ | 0.108 | 0.104 | 0.013 | -0.023 | -0.017 | 0.013 |
| $\rho^0_{1-1}$ | 0.090 | 0.093 | 0.022 | 0.037 | 0.023 | 0.025 |
| $\rho^1_{11}$ | 0.031 | 0.029 | 0.026 | -0.016 | -0.031 | 0.030 |
| $\rho^1_{00}$ | -0.140 | -0.136 | 0.035 | -0.049 | -0.054 | 0.022 |
| $\rho^1_{10}$ | -0.088 | -0.086 | 0.018 | 0.000 | 0.001 | 0.022 |
| $\rho^1_{1-1}$ | 0.322 | 0.315 | 0.030 | 0.355 | 0.361 | 0.035 |
| $\rho^2_{10}$ | 0.127 | 0.121 | 0.020 | -0.038 | -0.030 | 0.025 |
| $\rho^2_{1-1}$ | -0.357 | -0.368 | 0.027 | -0.395 | -0.384 | 0.035 |

**Table 4.8:** The evaluated spin density matrix elements by EML fit results with MC sets.

The measured error of parity spin asymmetry has a small value in the helicity frame. The resion though to be the decay frame dependence. Figure 4.34 shows error distribution from unbinned EML result with MC set in the GJ frame and helicity frame. We can find that the error of $\rho^1_{00}$ for helicity frame is smaller than GJ frame, it is consistent with our results.

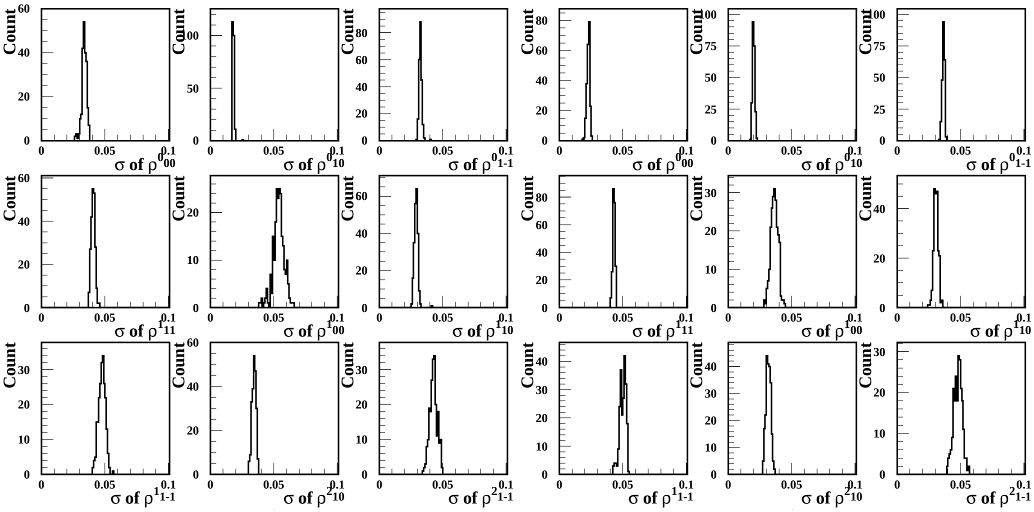

(a) GJ frame

(b) helicity frame

**Figure 4.34:** Error distribution from unbinned EML fit result with MC netuple set by using the measured spin-density matrix elements in the GJ frame (a) and helicity frame (b).

## 4.10 Differential Cross Section $K^{*0}\Sigma^+$ Photoproduction

We obtained differential cross sections for the $K^{*0}\Sigma^+$ photoproduction in 6 photon-energy bins from 2.4 to 2.95 GeV.

The differential cross section was obtained by the following equation:

$$\frac{d\sigma}{d\cos\theta} = \frac{1}{N_\gamma \cdot N_t}\frac{dN_{K^{*0}}}{d\cos\theta},$$

where $N_{K^{*0}}$ is the acceptance-corrected number of $K^{*0}$ events. $N_t$ is the number of target protons in the 16-$\mathrm{cm}$ long LH2 target, which can be estimated to be $6.822 \times 10^{23}$ protons per unit area ($\mathrm{cm}^2$). The number of photons were calculated by the formula,

$$N_\gamma = N'_\gamma \cdot P_{ntag=1} \cdot T,$$

where $N'_\gamma$ is the number of measured photons by a tagger, $4.048 \times 10^{11}$ photons for this measurement, $2.038 \times 10^{11}$ and $2.010 \times 10^{11}$ photons for horizontal and vertical polarizations, respectively. $P_{ntag=1}$ denotes a probability for having fntag=1,which was found to be 98%. $T$ represents a transmission probability of photon beam, which was estimated to be 0.526.

The number of photons for each energy bin $E_i$ is then given by $N_\gamma \cdot f(E_i)$, where $f(E_i)$ is a fraction of the number of photons for a given energy bin as listed in Table 4.9.

| $E_\gamma$ bin | $E_\gamma$ (GeV) | $f(E_i)$ |
|---|---|---|
| E1 | 2.4 – 2.5 | 0.0686 |
| E2 | 2.5 – 2.6 | 0.0734 |
| E3 | 2.6 – 2.7 | 0.0801 |
| E4 | 2.7 – 2.8 | 0.0874 |
| E5 | 2.8 – 2.9 | 0.0970 |
| E6 | 2.9 – 2.95 | 0.0522 |

**Table 4.9:** Photon energy bin and its fraction of the numbe of photons for each bin.

Figure 4.35 shows invariant mass spectra according to photon energy range and production angle bin with side-band subtraction. Only two angular bins contain the events, one being +0.8 $< \cos\theta_{K^{*0}} <$ +0.9 (COS1) and the other from +0.9 to +1.0 (COS2). To estimate the yield of $K^{*0}$, we made a templete fit to the invariant mass distribution (IM) with shape function for $K^{*0}$ production and four background processes as given by

$$\sum_{i=1}^{m} IM_i = \sum_{j=1}^{5}\sum_{j=1}^{m} a_j MC(j)_i,$$

where $m$ is the number of bins for the $K + \pi^-$ invariant mass, $i$ is $i^{th}$ bin, and $MC$ denotes the invariant mass distribution from Monte-Carlo sample. $a_j$ is a yield of $K^{*0}$ ($j$ = 1) and backgrounds

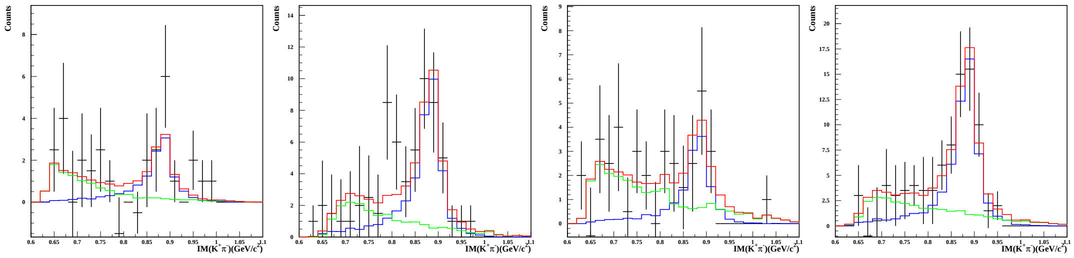

(a) E1, COS1 (b) E1, COS2 (c) E2, COS1 (d) E2, COS2

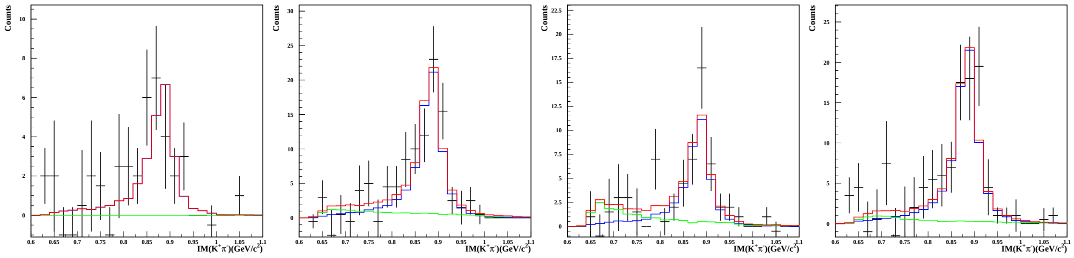

(e) E3, COS1 (f) E3, COS2 (g) E4, COS1 (h) E4, COS2

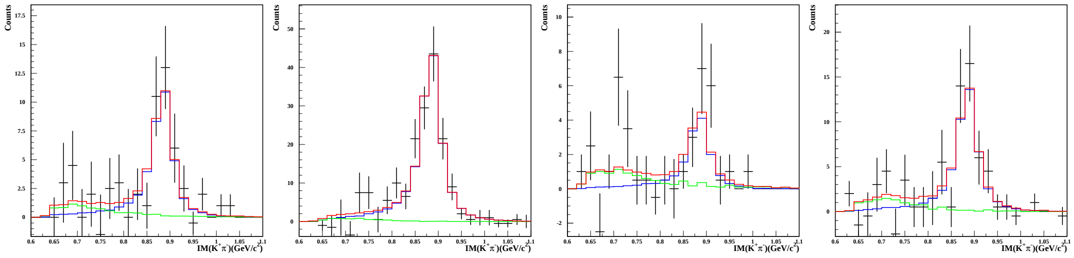

(i) E5, COS1 (j) E5, COS2 (k) E6, COS1 (l) E6, COS2

**Figure 4.35:** $K^{+}\pi^{-}$ invariant mass distributions in terms of photon energy and $K^{*0}$ production angle. Blue lines indicate $K^{*0}$ production, while green lines indicate hypreson-production background contributions. Red lines show a sum of the two contributions.

($j$ = 2,3,4,5). The templet fit didn't consern about missing mass of $K^{+}$ because of it is not only small events for the each angular and energy bins, but also hyperon distribution of the invariant mass of $K^{+}\pi^{-}$ is similar. By minimizing the $\chi^2$, we have a yield of $K^{*0}$. The $\chi^2$ is given by

$$\chi^2 = \sum_{i=1}^{m} \left[ \frac{IM_i - \sum_{j=1}^{5} MC(j)_i}{\sigma_i^2} \right],$$

where $\sigma_i$ is statistical error of real data for $i^{th}$ bin. We estimated the number of the $K^{*0}$ events from the fit results of the $K^{+}\pi^{-}$ invariant mass spectra as indicated by blue histograms in Figure 4.35. The green line indicates the background yield and the red line is sum of the $K^{*0}$ and backgrounds.

We calculated the $K^{*0}$ acceptance over production angles in the CM system of $\gamma p \to K^{*0}\Sigma^{+}$ reaction, based on a Monte-Carlo simulation as shown in Figure 4.36. We generated 50 M events with $t$ slope fixed and the measured SDM elements for the GJ frame and helicity frame, respectively.

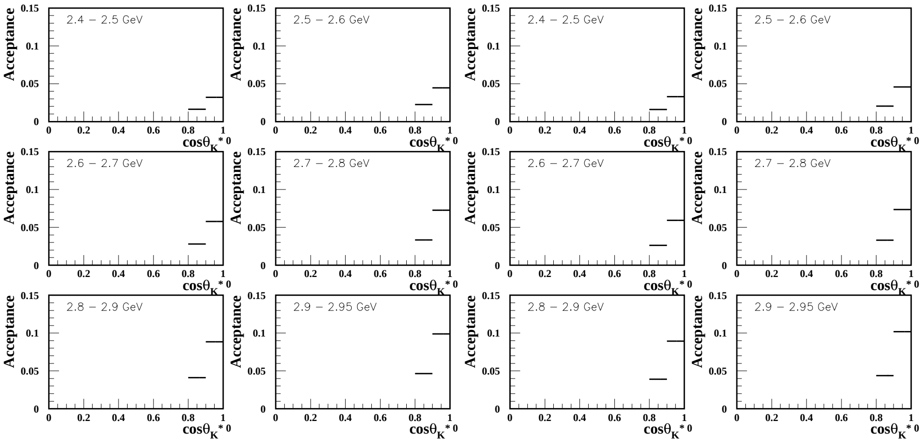

(a) GJ frame (b) helicity frame

**Figure 4.36:** The $K^{*0}$ acceptance distributions for 6 energy bins from 2.4 to 2.95 GeV, which were obtained by a Monte-Carlo simulation with measured SDM elements and $t$-slope fixed in the GJ frame (left panel) and helicity frame (right panel), respectively.

The differential cross sections for $K^{*0}\Sigma^{+}$ photoproduction from 2.5 to 2.95 GeV are largely increased at forward angles, as shown in Figure 4.37. Our measurement results are represented by black crosses, while red cross points indicate the CLAS results by Ref. [5] and green ones for data from the CBELSA/TAPS collaboration by Ref. [6], respectively.

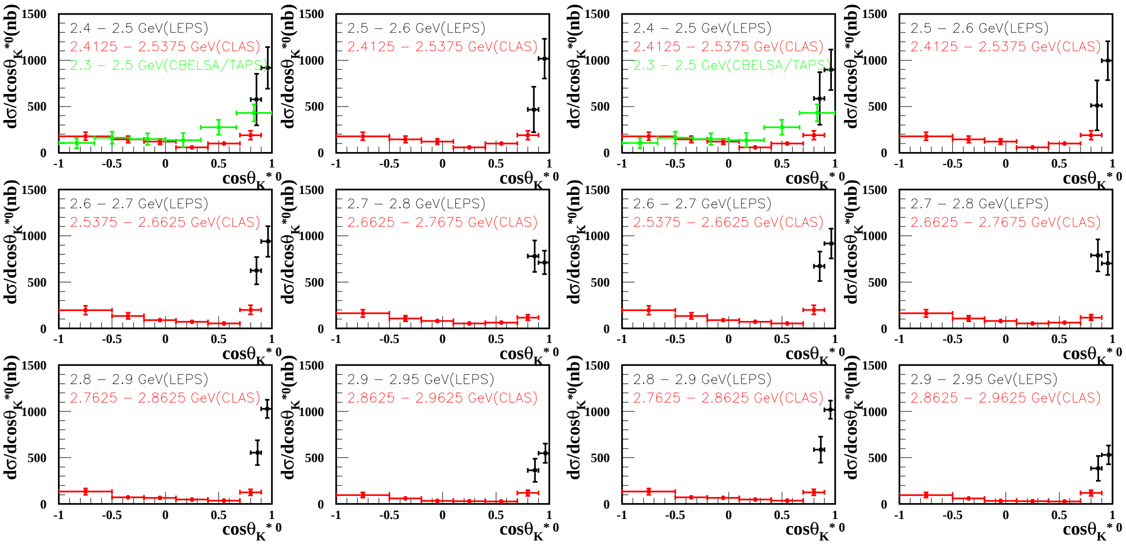

(a) GJ frame (b) helicity frame

**Figure 4.37:** The differential cross section for $K^{*0}\Sigma^{+}$ production from 2.5 to 2.95 GeV.

# Chapter 5

# Conclusions

The photoproduction of $\gamma p \to K^{*0}\Sigma^+$ reaction was measured at the LEPS detector in the in the very forward production angle at the energy from threshold to 3.0 GeV by using a linearly polarized photon beam at SPring-8. We measured the parity spin asymmetry and differential cross section for $\gamma p \to K^{*0}\Sigma^+$ reaction, and found forward peaking behavior. In particular, the parity spin asymmetry experiment can be outstanding probes to separate the $\kappa$ meson exchange in $K^{*0}\Sigma^+$ production.

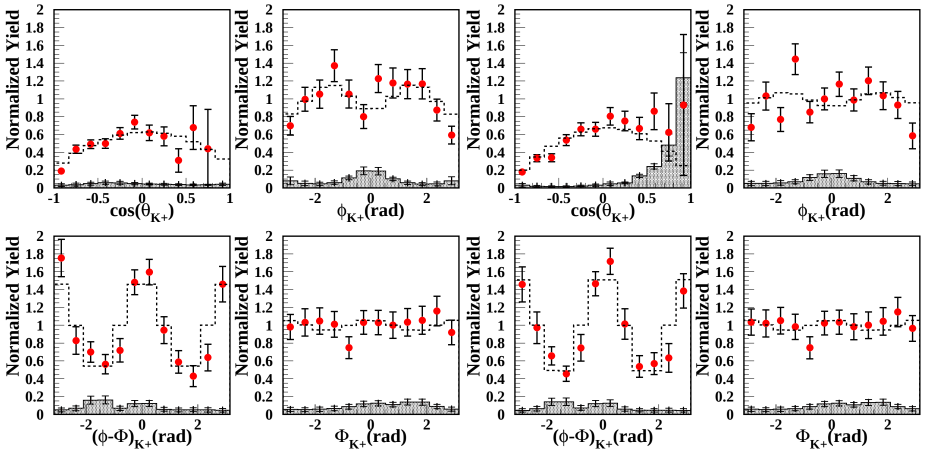

(a) GJ frame

(b) helicity frame

**Figure 5.1:** Decay angular distributions of $\cos\theta_{K^+}$, $\phi_{K^+}$, $(\phi-\Phi)_{K^+}$, and $\Phi_{K^+}$ in the GJ frame(a) and helicity frame(b) for the sum of vertical polarization and horizontal polarization after acceptance correction, respectively. The dotted line shows Monte-Carlo data using the measured spin-density matrix elements, while the overlaid black histogram indicates the $Y^*$ background yield from a Monte-Carlo simulation.

We presented spin-density matrix elements using unbinned extended maximum likelihood fit in the GJ frame and helicity frame. Figure 5.1 show decay angular distributions for a sum of horizontal and vertical beam polarizations with only a single variable, $\cos\theta_{K+}$, $\phi_{K+}$, $(\phi - \Phi)_{K+}$ and $\Phi_{K+}$, in the GJ frame(a) and helicity frame(b), respectively. The data have been corrected for detector acceptance by a Monte-Carlo simulation.The dotted lines indicate Monte-Carlo distributions with the measured spin-density matrix elements in the GJ frame and helicity frame. Black histograms indicate the estimated $Y^*$ background in the reconstructed Monte-Carlo distribution. In the helicity frame, the $\cos(\theta_{K+})$ distribution is enhanced at forward angles due to the $Y^*$ production. However, the $Y^*$ background there is actually quite small; the apparent enhancement near $\cos\theta_{K+} \simeq 1$ is because the spectra are corrected for the $K^{*0}$ acceptance, which is very small in that angular region. The few counts of $Y^*$ background there has little effect on the extraction of the spin-density matrix elements, which is heavily weighted by events with $\cos\theta_{K+} < 0.5$.

The parity spin asymmetry ($P_\sigma = 2\rho^1_{1-1} - \rho^1_{00}$) is estimated to be $0.784 \pm 0.154$ in the GJ frame and $0.758 \pm 0.123$ in the helicity frame over the angular range shown by the horizontal error bar in Figure 5.2. The good agreement between the parity spin asymmetry extracted in both frames is expected; the variation of these two results is a good indication of the systematic uncertainty, as the $Y^*$ background has a different distribution in the two frames. The large positive asymmetry shows that natural parity exchange is the dominant process at forward angles. The dashed (solid) line in Figure 5.2 is the result with (without) $\kappa$-exchange in the model of Ref. [38] at $E_\gamma = 2.5$ GeV. The data clearly favors the $\kappa$-exchange calculation.

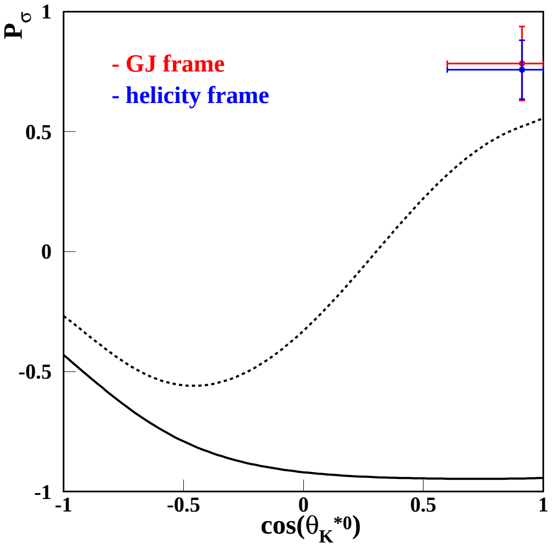

**Figure 5.2:** Efficiencies and spatial resolutions of the drift chamber planes with run numbers. The dashed (solid) line is the result with (with-out) $\kappa$-exchange in the model of Ref. [38] at $E_\gamma$ = 2.5 GeV.

This supports that a natural-parity exchange is dominant in foward angles for $K^{*0}\Sigma^+$ photoproduction. A natural explanation for the natural-parity exchange would be t-channel of a scalar meson with strangeness, which is consistent with the $\kappa$ meson. The results of this experiment support the existence of this meson, which would complete the lowest-mass scalar meson octet.

# References

[1] J. W. C. McNabb *et al.* (CLAS Collaboration), Phys. Rev. C **69**, 042201(R)(2004)

[2] R. Bradford et al.(CLAS Collaboration), Phys. Rev. C **73**, 035202(2006)

[3] L. Guo and D. P. Weygand (CLAS Ccollaboration), arXiv:hep-ex/0601010 (2006).

[4] I. Hleiqawi, Ph.D thesis, Ohio University (2006).

[5] I. Hleiqawi *et al.*(CLAS collaboration), Phys. Rev. C **75**, 042201 (2007)

[6] M. Nanova *et al.*(The CBELSA/TAPS collaboration), Eur. Phys. J. A **35**, 333-342 (2008)

[7] M. Gell-Mann and Y. Ne'eman, *The Eightfold Way*, (W.A. Benjamin, New York, 1964).

[8] K. Nakamura *et al.*, (Particle Data Group), J. Phys. G **37**, 075021 (2010).

[9] Keniji Igi and Ken-ichi Hikasa, Phys. Rev. D **59**, 034005 (1999).

[10] I. Caprini *et al.*, Phys.Rev.Lett. **96** 132001 (2006)

[11] E. M. Aitala *et al.* (Fermilab E791 Collaboration), Phys.Rev.Lett. **86** 770 (2001)

[12] H. Muramatsu *et al.* (CELO Collaboration), Phys.Rev.Lett. **89** 251802 (2002)

[13] R. Jaffe, Phys. Rev. D **15**, 267 (1977).

[14] M. Alford and R.L. Jaffe, Nucl. Phys. **B578**, 367 (2000).

[15] C. Amsler and N. Tornqvist, Phys. Rep. **389**, 61 (2004).

[16] M. Ablikim *et al.*(BES Collaboration), Phys. Lett. B **633**, 681 (2006).

[17] M. Ablikim *et al.*(BES Collaboration), Phys. Lett. B **693**, 88–94 (2010).

[18] S. Descotes-Genon and B. Moussallam, Eur. Phys. J. C **48**, 553-560 (2006)

[19] E. M. Aitala *et al.*, Phys. Rev. Lett. **89**, 121801 (2002).

[20] D.V. Bugg, Phys. Rev. D **81** 014002 (2010)

[21] G. Bonvicini *et al.* (CELO Collaboration), Phys. REV. **D 78** 052001 (2008)

[22] J.M. Link *et al.* (FOCUS Collaboration), Phys. Lett. **B535**, 430 (2007)

[23] D.V. Bugg, Phys. Lett. **B632**, 471-474 (2006)

[24] C. Cawlfield, *et al.* (CELO Collaboration), Phys. Rev. **D 74**, 052001 (2006)

[25] Z.Y. Zhou and H.Q. Zheng, Nucl. Phys. **A775** 212-223 (2006)

[26] J. R. Pelaéz, Phys. Rev. Lett. **92** 102001 (2004)

[27] S. Ishida *et al.*, Prog. Theor. Phys. **98**, 621 (1997)

[28] B. Aubert *et al.* (BABAR Collaboration), Phys. Rev. **D 76**, 011102R (2007)

[29] M.J. Jamin *et al.*, Nucl. Phys. **B 587**, 331 (2000).

[30] Z.Xio, H.Q.Zheng, Nucl. Phys. **A 695**, 273 (2001).

[31] D.V. Bugg, Phys. Lett. **B572**, 1 (2003).

[32] H.Q.Zheng *et al.*, Nucl. Phys. **A 733**, 235 (2004)

[33] S. Anderson *et al.* Phys. Rev. D **63**, 09001 (2001).

[34] S.N. Cherry and M.R. Pennington, Nucl. Phys. **A 688**, 823-841 (2001).

[35] T. Mart and C. Bennhold, Phys. Rev. C **61**, 012201 (1999).

[36] Q. Zhao, J.S. Al-Khalili, and C. Bennhold, Phys. Rev. C **64**, 052201 (2001).

[37] Q. Zhao, *Numerical fit by the quakr model of Ref. 37 to the CBELSA/TAPS data*, private communication.

[38] Y. Oh, H. Kim, Phys. Rev. C **74**, 015208 (2006).

[39] Y. Oh, H. Kim, Phys. Rev. C **73**, 065202 (2006).

[40] K. Schilling, P. Seyboth, and G. Wolf, Nucl. Phys. **B15**, 397 (1970).

[41] W.C. Chang *et al.* (LEPS Collaboration), Phys. Rev. C 82, 015205 (2010).

[42] T. Mibe, Ph.D. thesis. Osaka University, (2004).

[43] T. Mibe *et al.* (LEPS Collaboration), Phys. Rev. Lett. **95**, (2005).

[44] M. Miyabe, Ph.D. thesis. Kyoto University, (2010).

[45] CERN Application Software Group, GEANT3.2, CERN Program Library writeup Report No. W5013, (1994).

[46] K. Tsumaki, SPring-8 annual report, 132 (1998)

[47] Preinstallation Manual, The coherent INNOVA, Sabre FRED$^{TM}$ Ion Laser

[48] S. Mandelstam, Phys. Rev. **112**, 1344 (1958)

[49] M. Sumihama *et al.* (LEPS Collaboration), Phys. Rev. C**73**, 035214 (2006).

[50] Y. Kato and M. Sumihama, Internal LEPS Technical note No. 44.

[51] M. Sumihama, PhD thesis (2003).

[52] Y. Kato, Internal LEPS Technical note No. 30.

[53] M. Sumihama, Internal LEPS Technical note No. 61.

[54] W.C. Chang, Internal LEPS Technical note No. 60.

[55] W.C. Chang *et al.* (LEPS Collaboration), Phys. Rev. C **82**, 015205 (2010)

[56] W. M. Allison and J. P. Comellas, Nucl. Instrum. Methods **A245**, 530 (1986)

[57] R. Barlow, Nucl. Instrum. Methods **A297**, 496 (1990)

# Appendix A

# : Number of photon

In this chapter, we lists the fraction and the number of photons in each energy bin as listed in Table A.1. The fraction and the number of photons was measured Ref. [53]. Total numbers of photons integrating the whole energy range are

$2.038 \times 10^{11}$ for horizontal polarization,

$2.010 \times 10^{11}$ for vertical polarization.

The ratio of photon energy is

$N_\gamma^{Hori.}/N_\gamma^{Vert.} = 1.0138.$

| $E_\gamma$ (GeV) | fraction | $N_\gamma$(Vert.) | $N_\gamma$(Hori.) |
|---|---|---|---|
| 1.45 – 1.50 | 0.0282 | .5678E+10 | .5756E+10 |
| 1.50 – 1.55 | 0.0279 | .5617E+10 | .5694E+10 |
| 1.55 – 1.60 | 0.0276 | .5554E+10 | .5630E+10 |
| 1.60 – 1.65 | 0.0274 | .5507E+10 | .5583E+10 |
| 1.65 – 1.70 | 0.0273 | .5487E+10 | .5562E+10 |
| 1.70 – 1.75 | 0.0272 | .5459E+10 | .5535E+10 |
| 1.75 – 1.80 | 0.0271 | .5452E+10 | .5527E+10 |
| 1.80 – 1.85 | 0.0272 | .5460E+10 | .5535E+10 |
| 1.85 – 1.90 | 0.0273 | .5483E+10 | .5558E+10 |
| 1.90 – 1.95 | 0.0273 | .5481E+10 | .5557E+10 |
| 1.95 – 2.00 | 0.0275 | .5534E+10 | .5610E+10 |
| 2.00 – 2.05 | 0.028 | .5626E+10 | .5703E+10 |
| 2.05 – 2.10 | 0.0283 | .5686E+10 | .5765E+10 |
| 2.10 – 2.15 | 0.0286 | .5750E+10 | .5830E+10 |
| 2.15 – 2.20 | 0.0293 | .5890E+10 | .5971E+10 |
| 2.20 – 2.25 | 0.03 | .6028E+10 | .6111E+10 |
| 2.25 – 2.30 | 0.0307 | .6171E+10 | .6256E+10 |
| 2.30 – 2.35 | 0.0317 | .6376E+10 | .6463E+10 |
| 2.35 – 2.40 | 0.0327 | .6566E+10 | .6657E+10 |
| 2.40 – 2.45 | 0.0337 | .6776E+10 | .6870E+10 |
| 2.45 – 2.50 | 0.0349 | .7024E+10 | .7121E+10 |
| 2.50 – 2.55 | 0.0359 | .7224E+10 | .7324E+10 |
| 2.55 – 2.60 | 0.0375 | .7532E+10 | .7636E+10 |
| 2.60 – 2.65 | 0.0394 | .7913E+10 | .8022E+10 |
| 2.65 – 2.70 | 0.0407 | .8176E+10 | .8289E+10 |
| 2.70 – 2.75 | 0.0424 | .8524E+10 | .8641E+10 |
| 2.75 – 2.80 | 0.045 | .9055E+10 | .9179E+10 |
| 2.80 – 2.85 | 0.0473 | .9498E+10 | .9629E+10 |
| 2.85 – 2.90 | 0.0497 | .9981E+10 | .1012E+11 |
| 2.90 – 2.95 | 0.0522 | .1050E+11 | .1065E+11 |
| 2.95 – 3.00 | 0.047 | .9438E+10 | .9568E+10 |
| 3.00 – 3.05 | 0.0008 | .1534E+09 | .1556E+09 |

**Table A.1:** Fraction and the number of photons in each energy bin.

# Appendix B

# : DC and ToF Calibration

The efficiencies of 16 chamber planes are shown in the left of Figure B.1 requiring that `ntrk=1, ntoul=0, prbchi2>0.02`, and `|ybar|<30mm`. The most upstream plane DC1X3 appears at the top left corner. Different colors indicated different filling patterns during the $K^*$ runs. Spatial resolution in each chamber plane is displayed in the right panel.

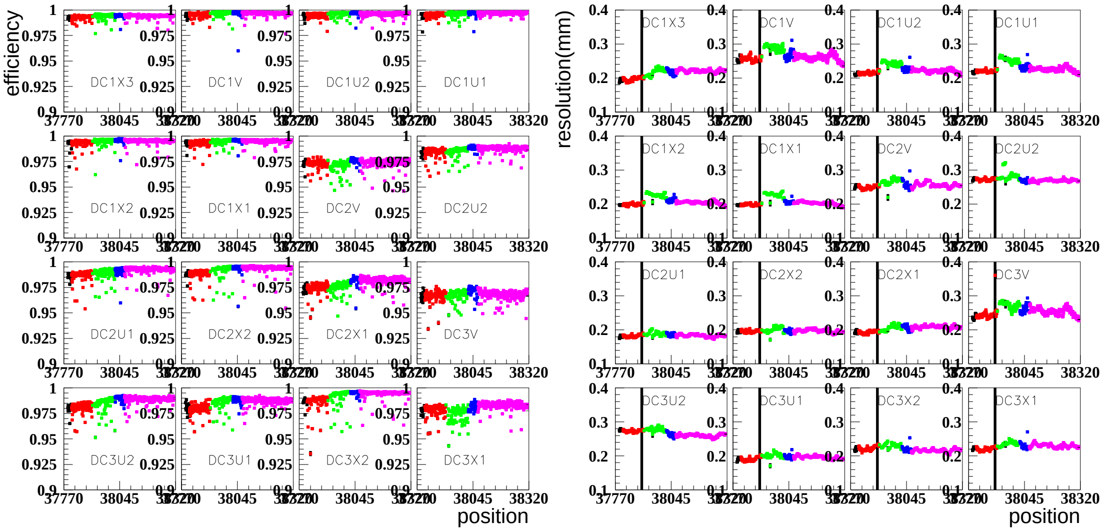

**Figure B.1:** Efficiencies and spatial resolutions of the drift chamber planes with run numbers.

The chamber efficiency for each wire is also studied in the left panel of Figure B.2. Two dip structures in some planes are due to the $e^+e^-$ blocker. Mean values of the $\chi^2$ probability distributions are shown in the right panel. Figure B.3 shows the mean value and standard deviation of the difference ($y_{trk}$-$y_{tdc}$) between y coordinates of reconstructed tracks measured from tracking and timing at the ToF. The mean values are fluctuated within 2 mm with run numbers.

The standard deviations are plotted in terms of ToF slat numbers in Figure B.4

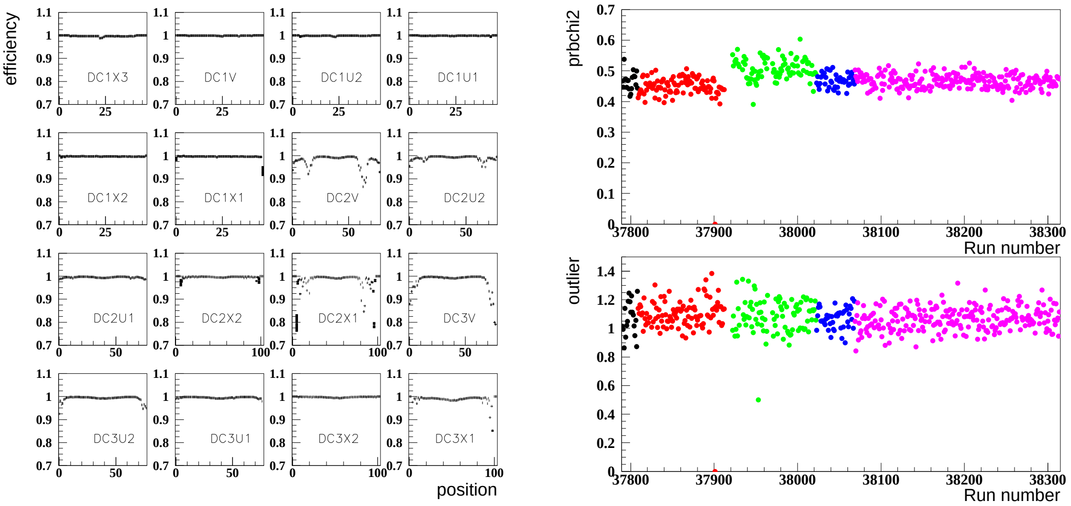

**Figure B.2:** Efficiencies of the wires for each chamber plane(left). The mean value of the $\chi^2$ probability distributions(right-top) and the number of outliers(right-bottom),noutl, are represented in terms of run number.

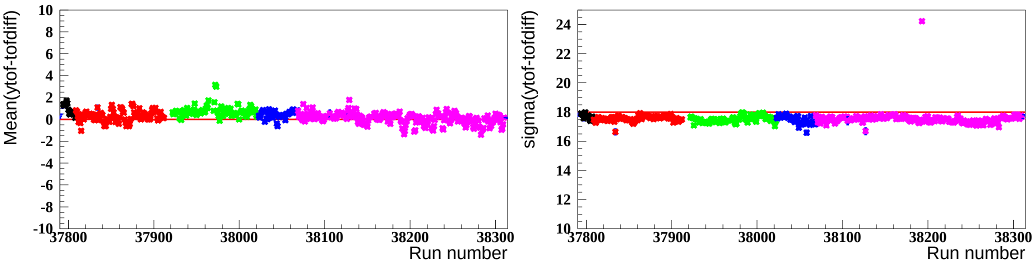

**Figure B.3:** Mean values and standard deviations for the $y_{trk}$-$y_{tdc}$ distributions in terms of run number.

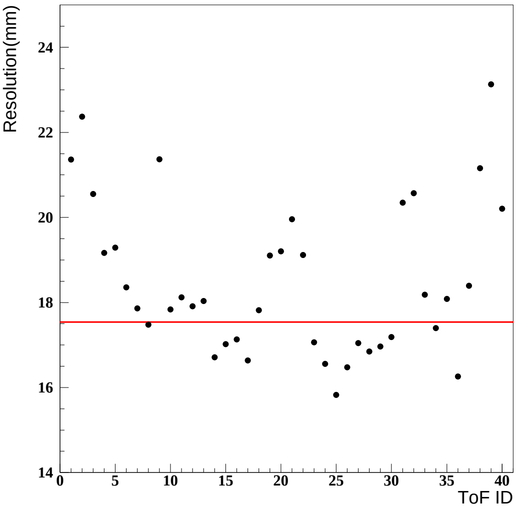

**Figure B.4:** Standard deviation of the y$_{trk}$-y$_{tdc}$ distribution for each ToF slat.

# Appendix C

# : Photon-Energy Calibration

We selected $K^+$ single-track events for $E_\gamma$ calibration. The following selection criteria were imposed:

- Reconstructed masses should be within $4\sigma$ tolerance window.
- Misidentified $K^+$ events were rejected by requiring that missing mass for ($\gamma$,$\pi^+$) be larger than 1.037 GeV assuming $K^+$ as $\pi^+$.
- $-1042$ mm $<$ `vtz` $< -860$ mm
- `prbchi2` $> 0.02$
- `|ytof - tofdiff|` $< 80$ mm
- `|itof - tofid|` $< 2$
- `fntag` = 1
- $e^+e^-$ events hitting the $e^+e^-$bar were rejected by requiring that `yebar` $<$ -30 mm and `yebar` $>$ 16 mm.

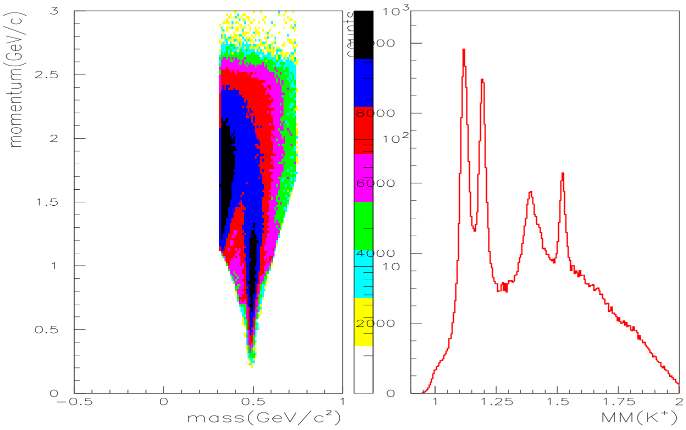

**Figure C.1:** Two-dimensional plot for the reconstructed masses of $K^+$ particles in terms of the respective momentum(left) and a missing mass distribution for $p(\gamma,K^+)X$ reaction.

Figure C.1 shows a scatter plot of the reconstructed mass distribution of charged particles with a primary $K^+$ mass cut in terms of the respective momentum (left), and a missing mass distribution for $p(\gamma, K^+)X$ reaction. Hight-momentum $\pi^+$ particles within the $K^+$ mass cut make a large background in the missing mass distribution.

Misidentified $K^+$ events within a 2-$\sigma$ boundary for the $\pi^+$ were rejected. Figure C.2 shows a new set of the $K^+$ events. Background contribution from particle misidentification was found to be largely suppressed in the missing mass distribution. The bottom figure shows the distributions for rejected events.

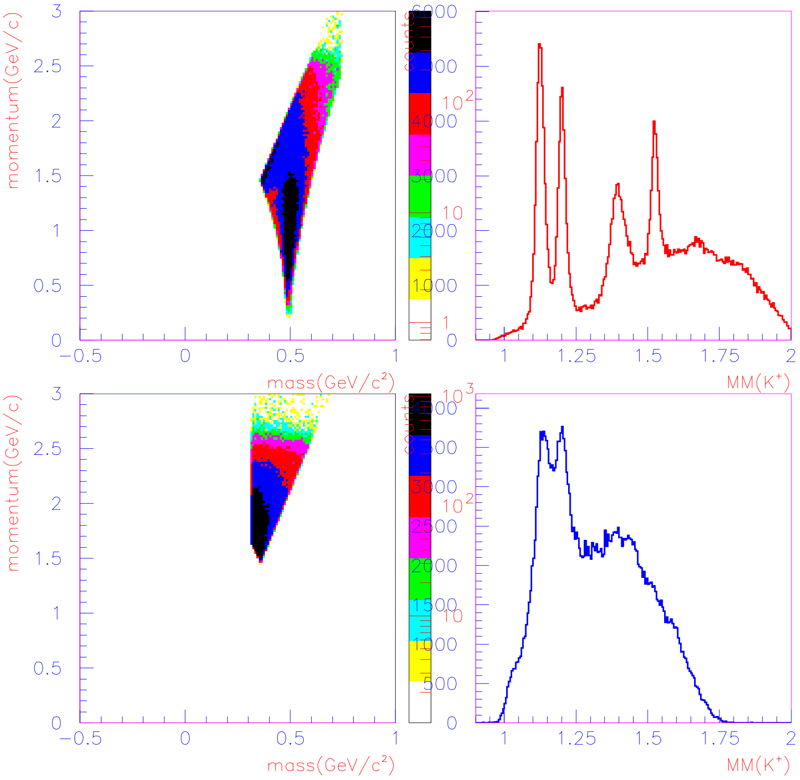

**Figure C.2:** Recontructed mass distributions in terms of the momentum(left) and the missing mass distributions for $p(\gamma, K^+)X$ reaction(right). Top figures indicate the distributions for a new set of $K^+$ events, and bottom figures represent the rejected events with a 2-$\sigma$ boundary cut for the $\pi^+$.

We obtained photon energy by fitting the missing mass distributions based on the relation:

$$p_\Lambda^2 = m_\Lambda^2 = (p_\gamma + p_p - p_{K^+})^2 = (E_\gamma + m_p - E_{K^+})^2 - (\vec{p}_\gamma - \vec{p}_{K^+})^2$$

where $p$ denotes a four-momentum of particle. We then fitted the photon energy in terms of the channel number of the fiber tagger with a third-order polynomial. Figure C.3, C.4 shows the fit results in terms of fiber number in the front and the rear planes of the tagger, respectively.

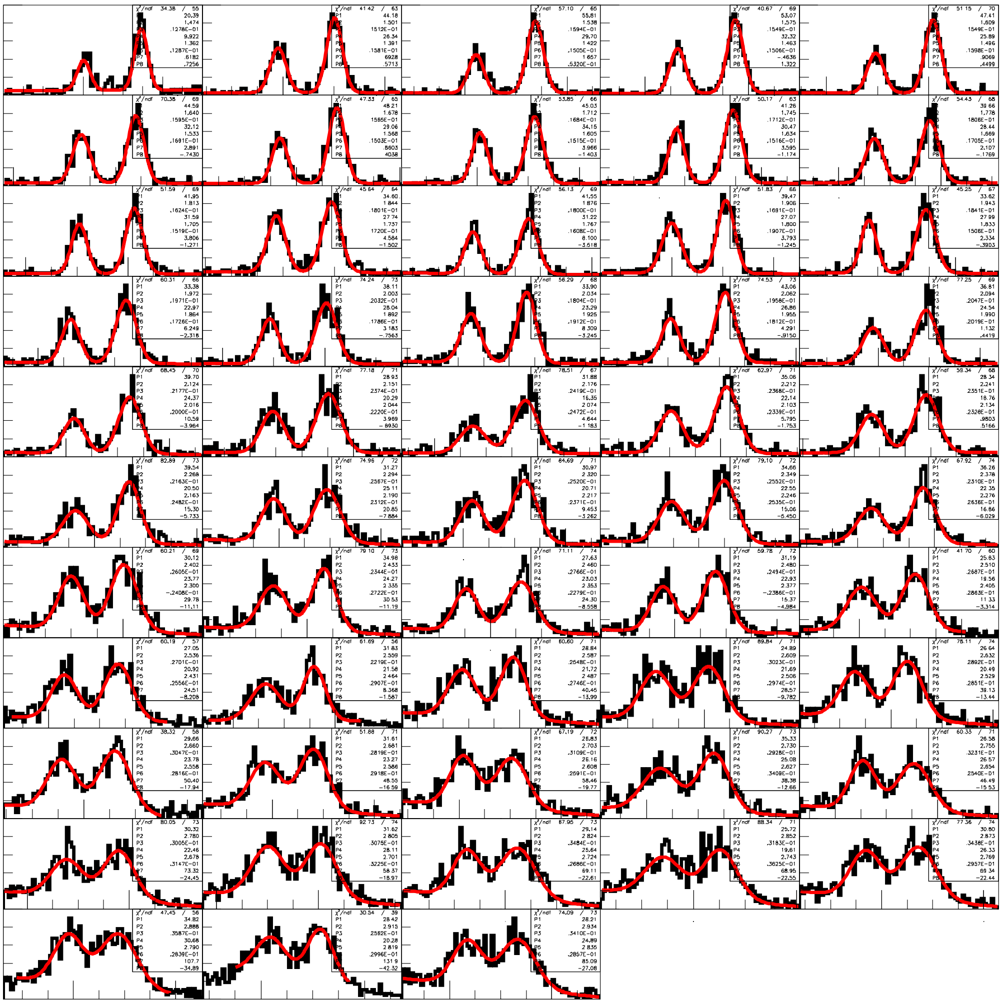

**Figure C.3:** Required photon-energy distribution in terms of fiber number of the front tagger plane.

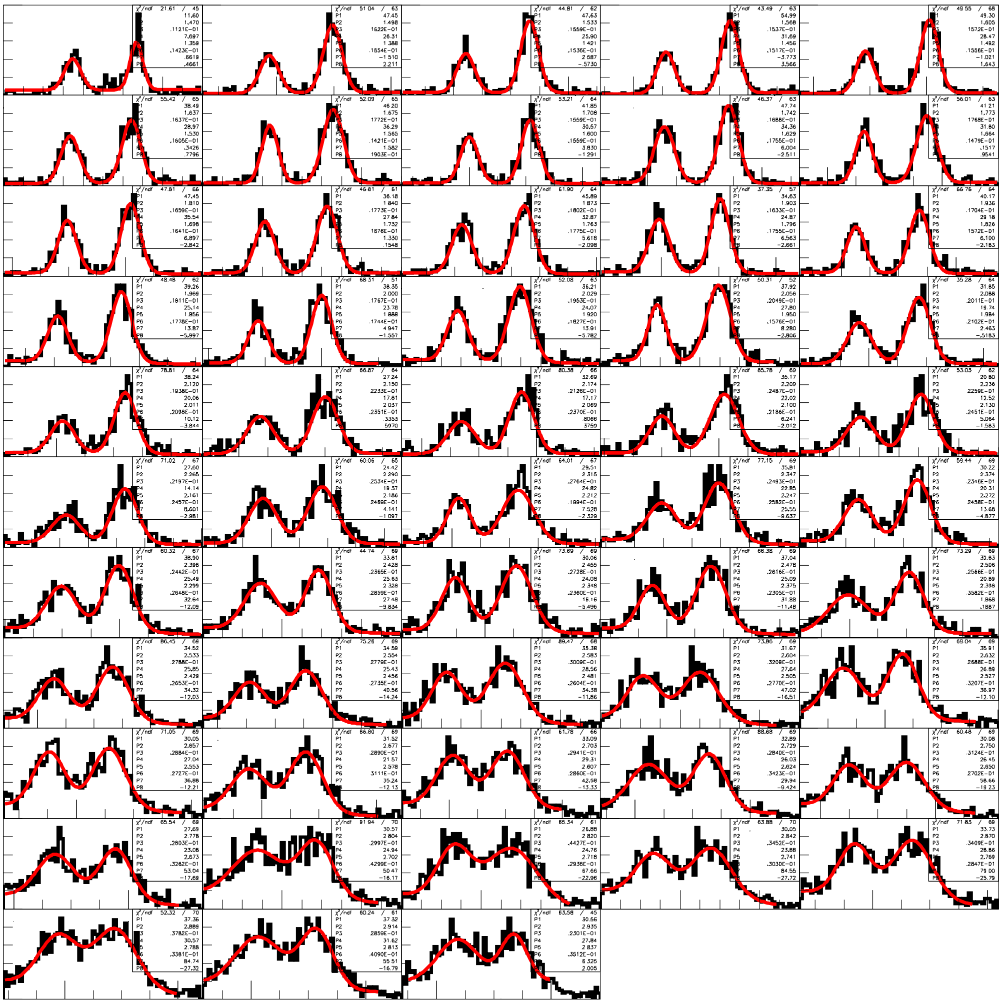

Figure C.4: Required photon-energy distribution in terms of fiber number of the rear tagger plane.

# Appendix D

# : Alignment Calibration

We reinstalled a vertex SSD for the $K^{*0}$ experiment in October, 2007. We first used a previous position coordinate of the vertex SSD to obtain DC parameters and photon beam positions. We then tuned the position coordinate of the vertex SSD by iterating the calibration procedures for DC parameters and photon beam positions. We finally found the best fit parameters for the position coordinate of the vertex SSD to probe that the missing mass peaks for $p(\gamma, K^+\Lambda$, $p(\gamma, K^+)\Sigma$, $p(\gamma, K^+)\Lambda(1520)$ and $p(\gamma, \pi^+)n$ reactions are consistent with the known values. The vertex SSD was found to be located at 0.05 mm from the center. Figure D.1 shows the energy dependence of missing mass for $p(\gamma, K^+\Lambda$, $p(\gamma, K^+)\Sigma$, $p(\gamma, K^+)\Lambda(1520)$ and $p(\gamma, \pi^+)n$ reactions, respectively. Horizontal lines indicate the world averages of particle masses with 1 MeV/$c^2$ window. Figure D.2 shows $1\sigma$ values from the Gaussian fit to the missing mass particle peaks for $p(\gamma, K^+\Lambda$, $p(\gamma, K^+)\Sigma$, $p(\gamma, K^+)\Lambda(1520)$ and $p(\gamma, \pi^+)n$ reactions, respectively. The overlaid red open circles indicate the values from the 2.4 GeV data set reported in the technical note No.44.

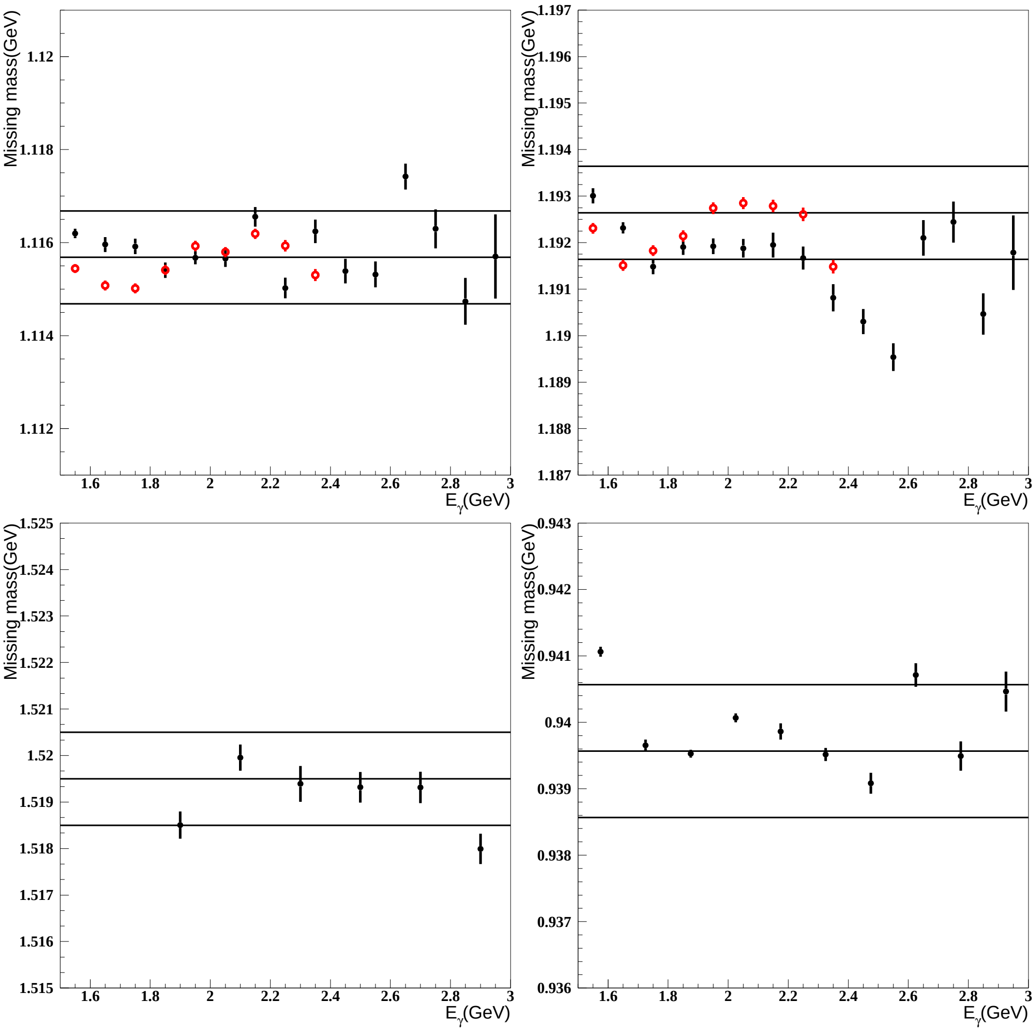

**Figure D.1:** Missing mass centroids for Lambda, Sigma, and Lambda(1520) in $p(\gamma, K^+)X$ reaction, and neutron in $p(\gamma, \pi^+)X$ reaction in terms of photon energy from 1.5 to 3 GeV

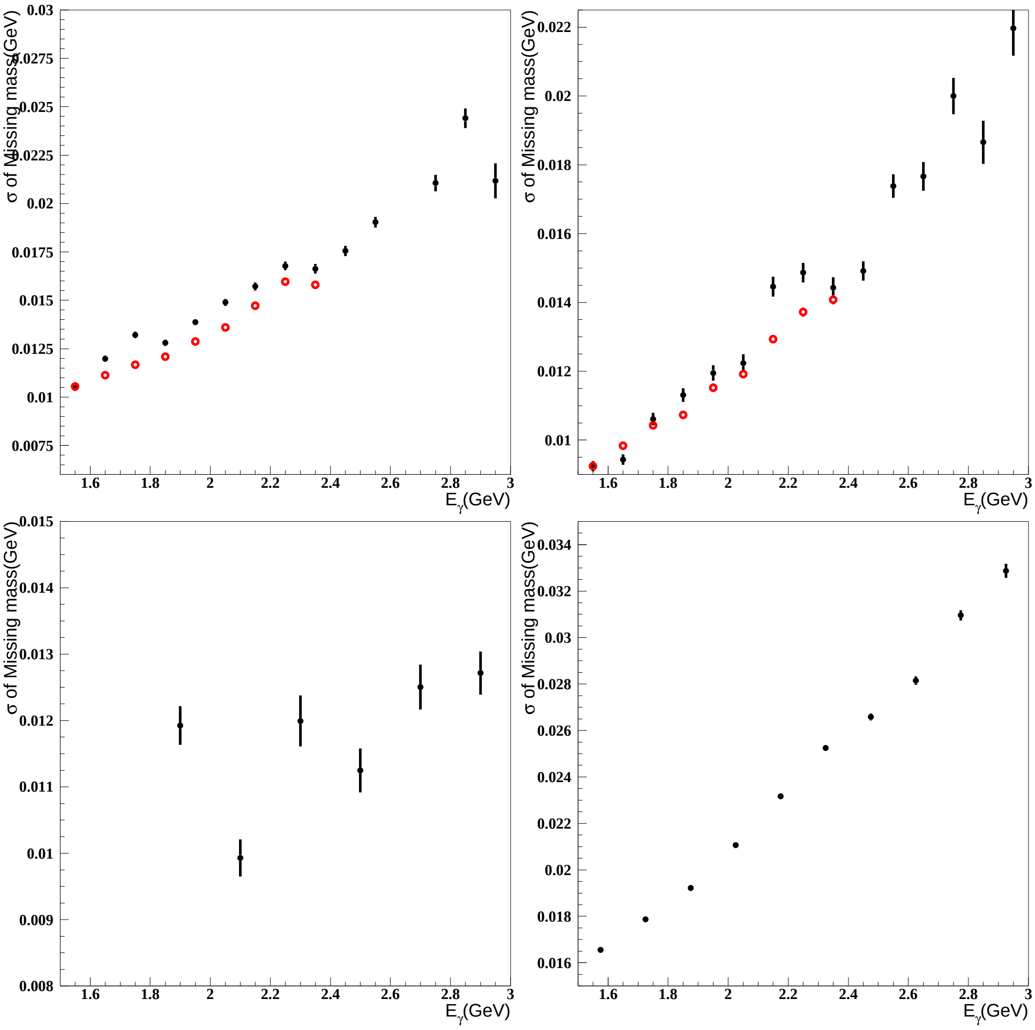

**Figure D.2:** $1\sigma$ standard deviations of the Gaussian fit to the missing masses for $p(\gamma,\,K^{+})\Lambda$(top-left), $p(\gamma,\,K^{+})\Sigma$(top-right), $p(\gamma,\,K^{+})\Lambda(1520)$(bottom-left) and $p(\gamma,\,\pi^{+})n$(bottom-right) reactions.

Energy dependence of the missing mass and the 1-$\sigma$ standard deviations of the Gaussian fit results for the proton and the $K^+$ peaks in the missing mass distributions for $p(\gamma,\, \pi^+\pi^-)p$, $p(\gamma,\, K^+K^-)p$ and $p(\gamma,\, K^-p)K^+$ reactions, respectively, in Figure D.3 and D.4.

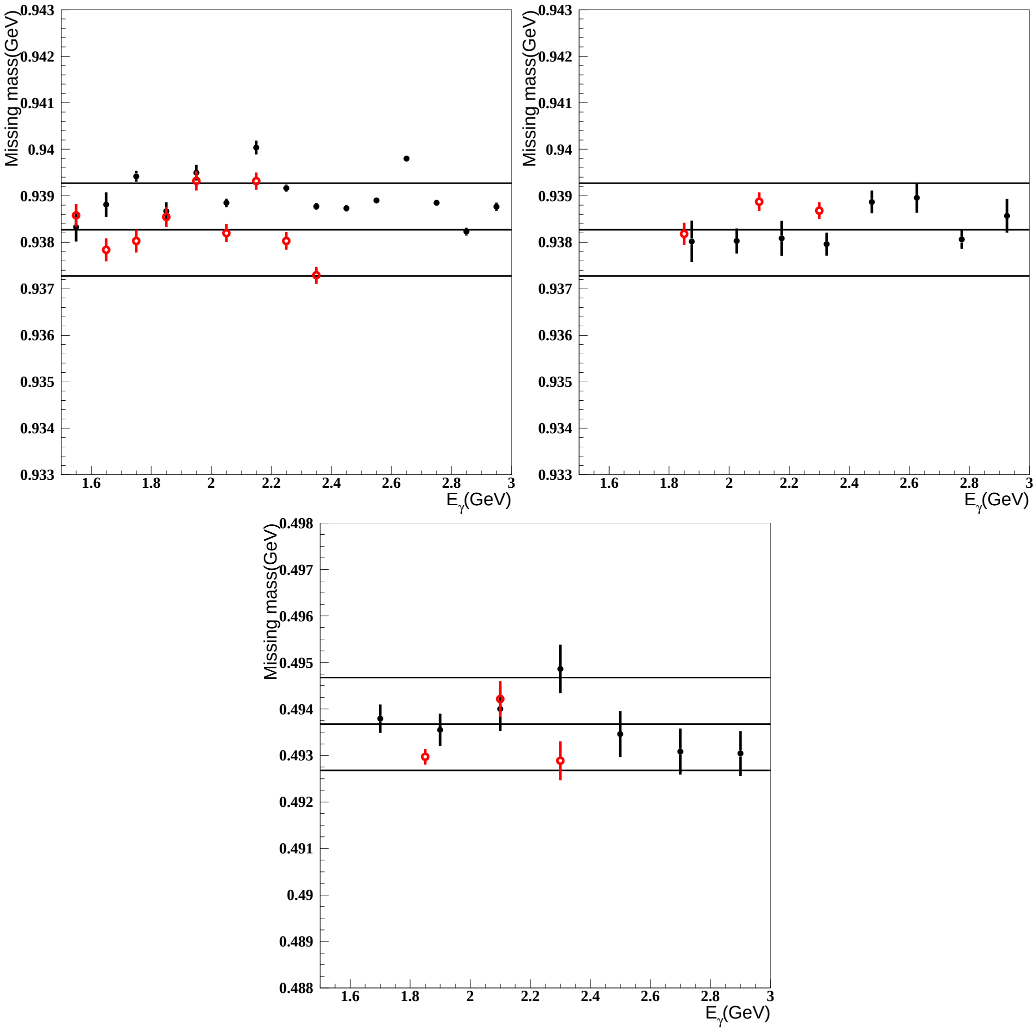

**Figure D.3:** Energy dependence of missing mass for $p(\gamma,\, \pi^+\pi^-)p$(top-left), $p(\gamma,\, K^+K^-)p$(top-right) and $p(\gamma,\, K^-p)K^+$(bottom) reactions.

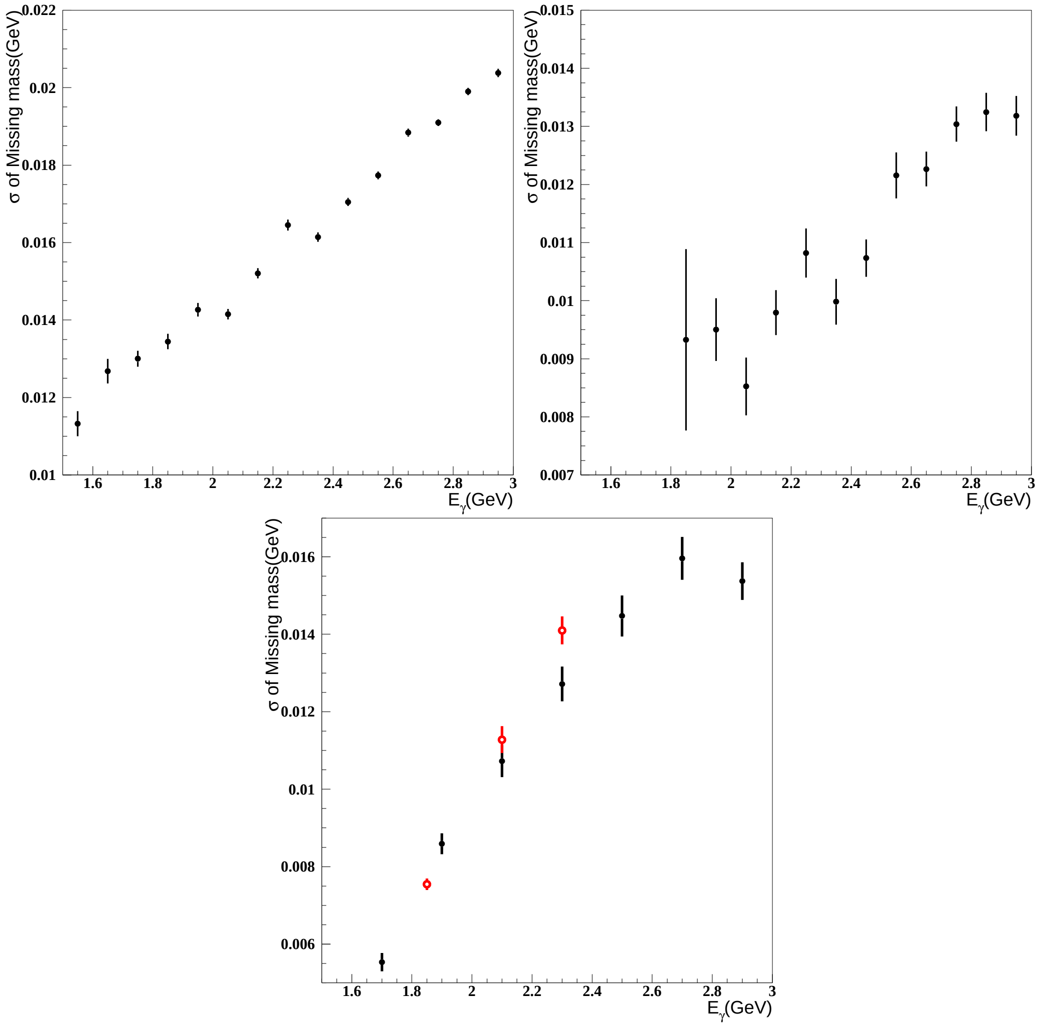

**Figure D.4:** 1$\sigma$ standard deviations of Gaussian fitted to the proton peaks for $p(\gamma, \pi^+\pi^-)X$ reaction(top-left), and $p(\gamma, K^+K^-)X$ reaction(top-right) and the $K^+$ peak for $p(\gamma, K^-p)X^+$ reaction(bottom).

# Appendix E

# : Calibration of PID Parameters

We first selected a good sample of particles for the PID parameter calibration with the selection criteria: 1.8 $< p_p <$ 2.0GeV/$c$ for protons, $p_\pi <$ 1.5GeV/$c$ and $|$`ybar`$| \geq$ 60 mm for pions, $p_{K+}$ $<$ 1.5GeV/$c$ for kaons. Figure E.1 shows the mean and standard deviation values of reconstructed mass squared for $p$, $K^+$ ,$\pi^+$, and $\pi^-$ from the top left corner. The reconstructed mass/charge versus momentum is shown in Figure E.2. Reconstructed $K^+$ mass should be within 3$\sigma$ tolerance window and should not fall into the $\pi^+$ PID boundary with 2$\sigma$ tolerance. Reconstructed $\pi^-$ mass should be within 3$\sigma$ tolerance window and should be within 2$\sigma$ tolerance in the region of the reconstructed mass larger than 0.33 MeV.

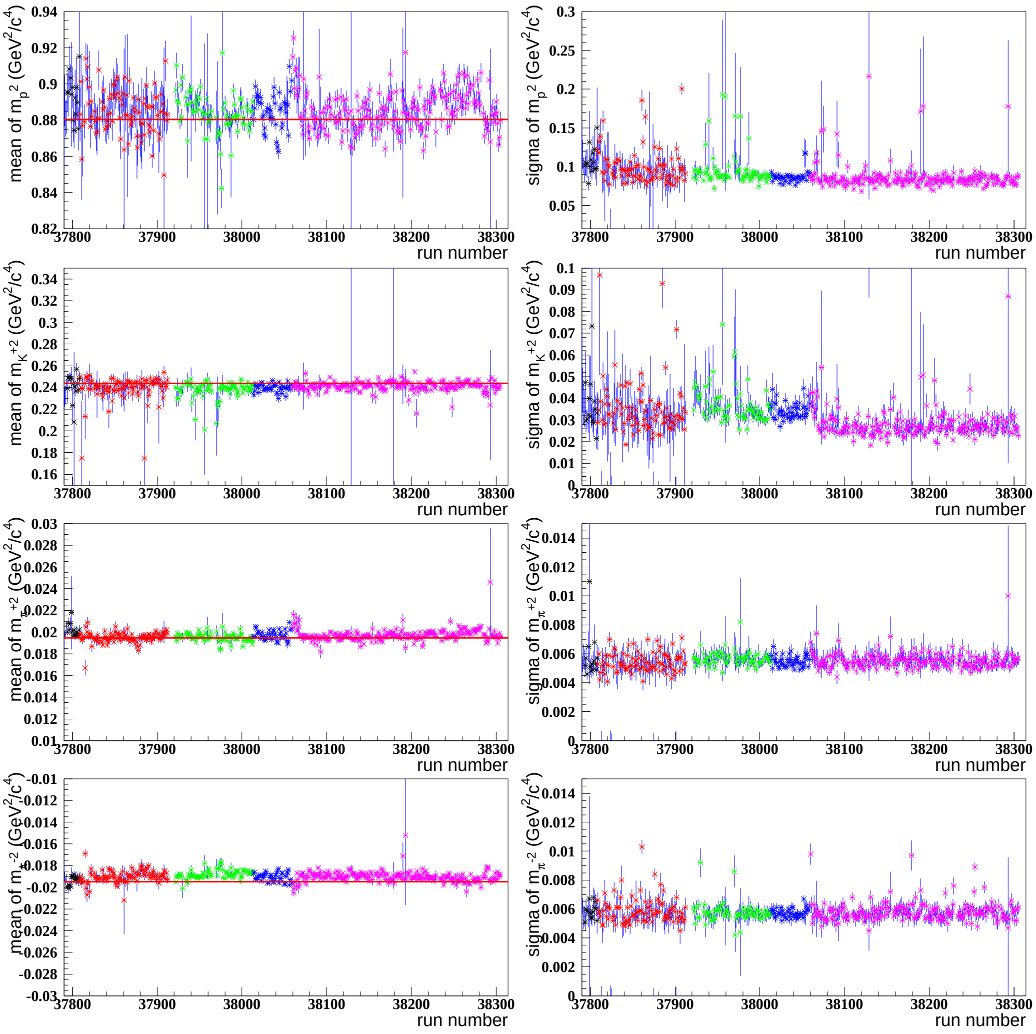

**Figure E.1:** Mean and standard deviation values of reconstructed mass squared for $p$, $K^+$ ,$\pi^+$, and $\pi^-$.

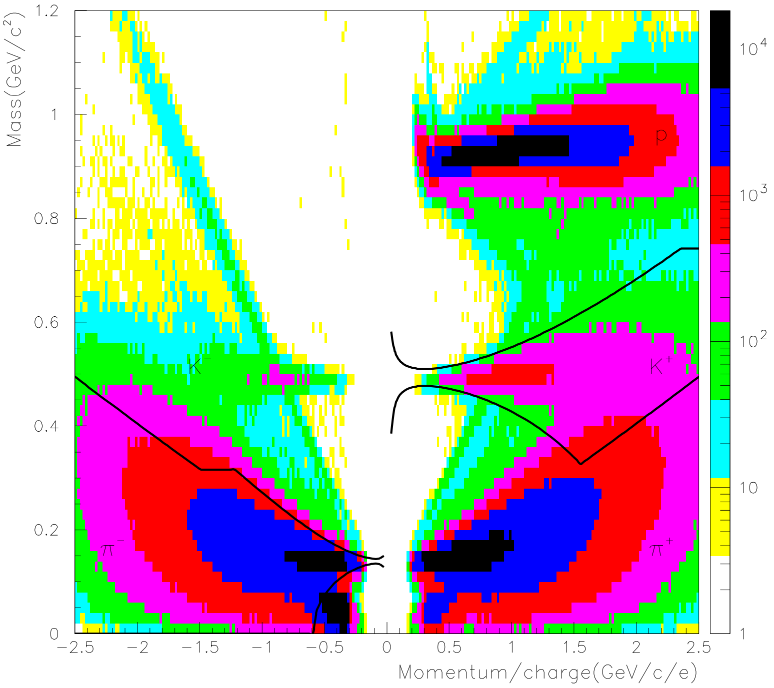

**Figure E.2:** Two-dimensional scatter plot of $K^+$ and $\pi^-$ events selection as a function of reconstructed mass versus momentum/charge.

# Appendix F

# : Photon Beam Asymmetry for $\Lambda$ photoproduction

We first tested a reliability of the calibrations for 3-GeV data with a Lambda beam asymmetry. To select $\Lambda$ events, the following selection criteria were imposed:

- Reconstructed $K^+$ mass should be within $3\sigma$ tolerance window and should not fall in to the $\pi^+$ PID boundary with $2\sigma$ mass tolerance.
- Misidentified $K^+$ events were rejected by requiring that missing mass for ($\gamma$,$\pi^+$) be out of the range between 0.875 GeV and 1.037 GeV.
- $-1042$ mm $<$ `vtz` $< -860$ mm
- `prbchi2` $> 0.02$
- `|ytof - tofdiff|` $< 80$ mm
- `|itof - tofid|` $< 2$
- `noutl` $< 6$
- `fntag` = 1
- `ybar` $<$ -30 mm and `ybar` $>$ 16 mm.
- `yebar` $<$ -30 mm and `yebar` $>$ 16 mm.
- Misidentified $K^+$ rejected by assuming $K^+$ as $\pi^+$(replacing $m_{K^+}$ with $m_{\pi^+}$) for the reaction $p(\gamma,\pi^+)n$, and $p(\gamma,\pi^+\pi^-)p$.

- $\phi$ photoproduction rejected for the reaction of $p(\gamma, K^+K^-)p$.

Figure F.1 shows the missing mass for $p(\gamma, K^+)X$ reaction. We fitted the $\Lambda$ and $\Sigma^0$ peaks with two Gaussian functions plus a straight line. The mean and the width values are shown in Figure F.2 as a function of $K^+$ momentum.

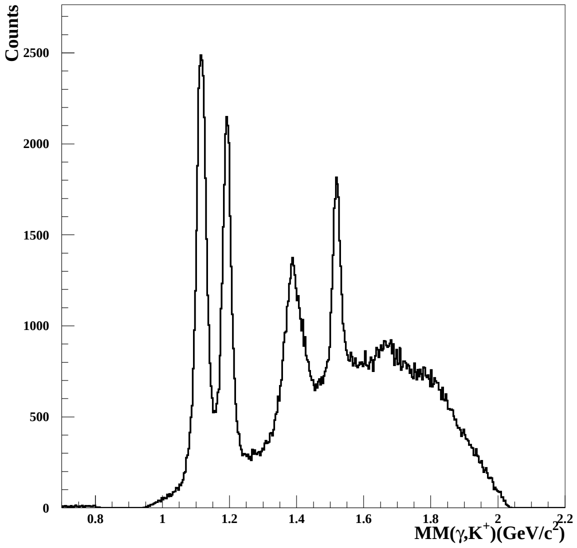

**Figure F.1:** The missing mass of $p(\gamma, K^+)X$

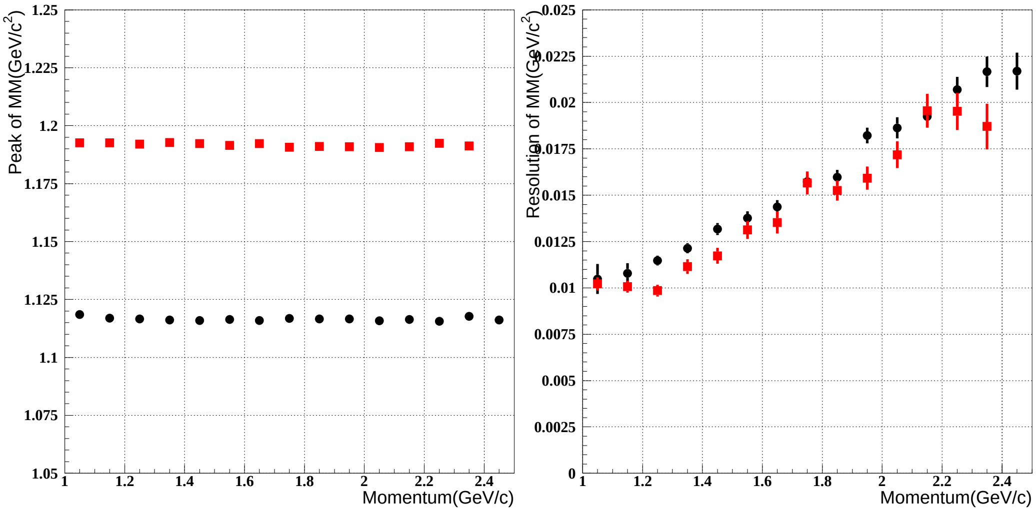

(a)

(b)

**Figure F.2:** (a) is the peak position as a function of the $K^+$ momentum and (b) is its resolution($\sigma$) of the missing mass for the $K^+$ events. The black dots are for $\Lambda$ and the red dots are for $\Sigma^0$.

Figure F.3 displays the scatter plot of missing mass for $p(\gamma, K^+)\Lambda, \Sigma^0$ in terms of $K^+$ momentum. The overlaid lines indicate the missing mass windows as a function of $K^+$ momentum with $1\sigma$, $1.5\sigma$, and $2\sigma$ tolerance, respectively. We selected $\Lambda$ events, which is missing mass for $p(\gamma, K^+)X$ as a function of the $K^+$ momentum should lie within $1.5\sigma$ tolerance window.

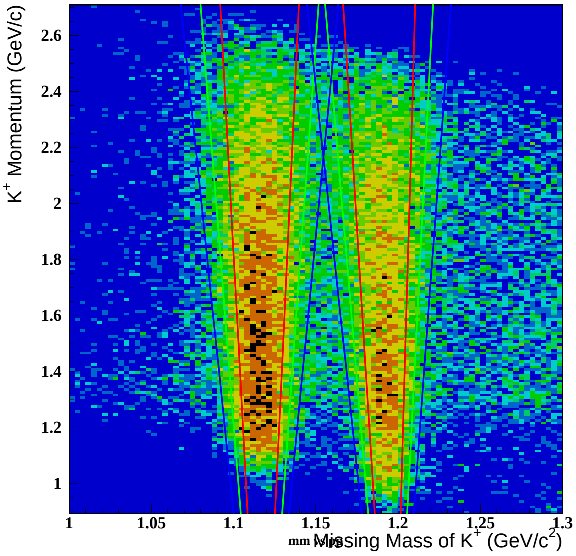

**Figure F.3:** Scatter plot of missing mass distributions for $p(\gamma,K^+)\Lambda^0, \Sigma^0$ versus $K^+$ momentum.

The photon beam asymmetry, $\Sigma$, is given by

$$\frac{n \cdot N_v - N_h}{n \cdot N_v + N_h} = P\Sigma\cos(2\phi_{K^+})$$

where $N_v(N_h)$ is the $K^+$ photoproduction yield with vertical(horizontal) polarized photon and $n$ is the normalization factor defined by number of photon yield($n = n_h/n_v = 1.0138$). The details of the fit procedure are presented in Appendix E. Figure F.4 is shown the beam asymmetry as a function of beam energy.

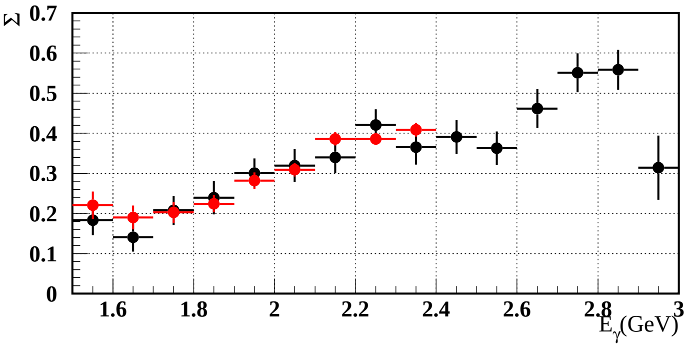

**Figure F.4:** Beam asymmetry of $K^+\Lambda$ photoproduction as a function of $E_\gamma$. The overlaid red dots indicate the values from the 2.4 GeV data set reported in Ref. [51] by M. Sumihama.

Figure F.5 and F.6 show the angular distributions for $\frac{n \cdot N_v - N_h}{n \cdot N_v + N_h}$ overlaid with fit results.

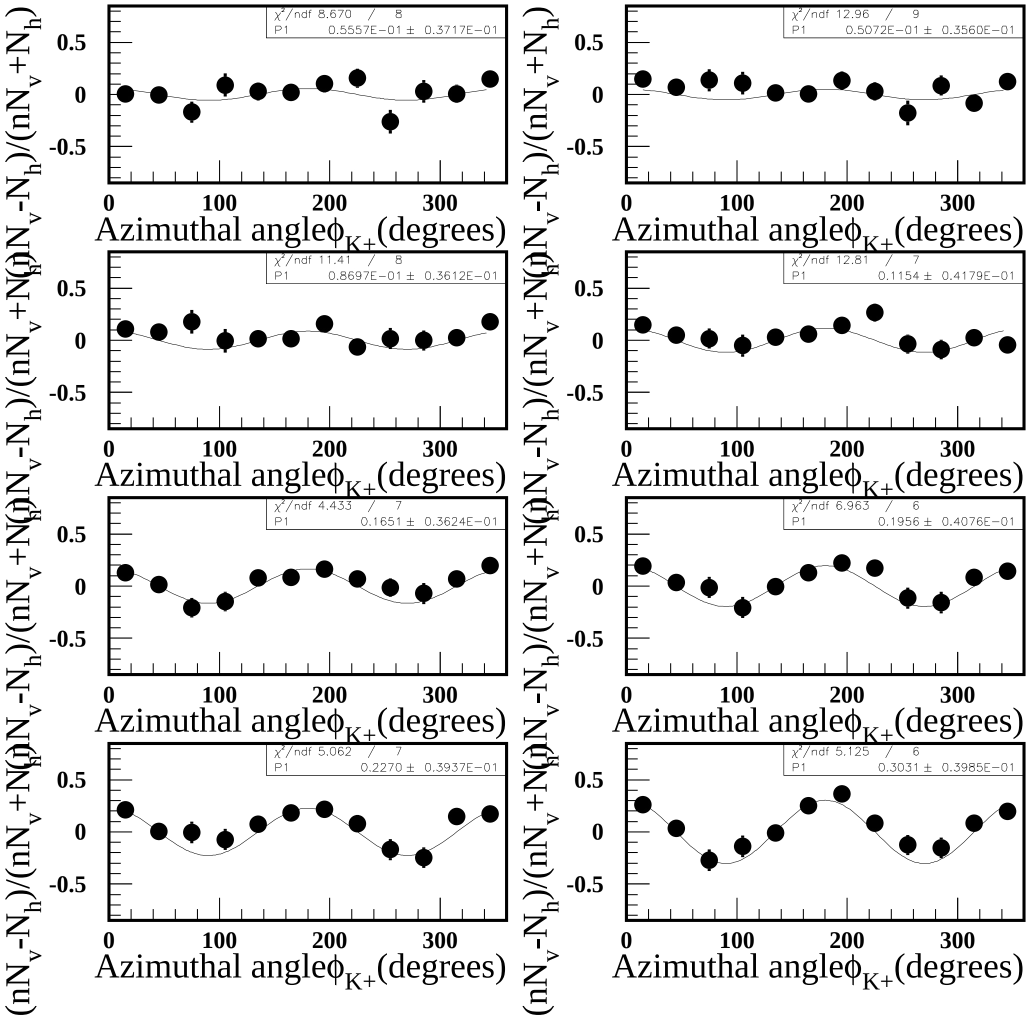

**Figure F.5:** The fitting distribution to the beam asymmetry as a function $E_\gamma$

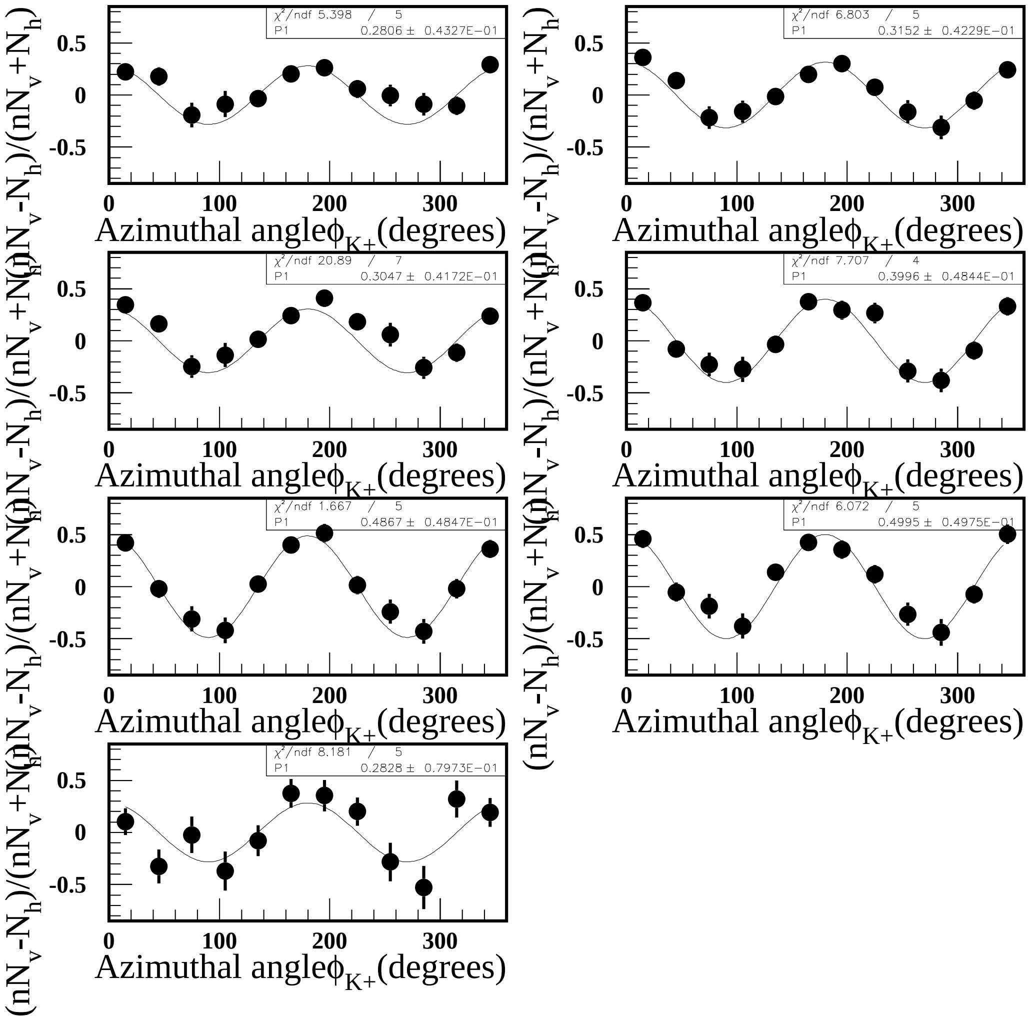

**Figure F.6:** The fitting distribution to the beam asymmetry as a function $E_\gamma$

# Appendix G

# : MC test for SDM

We stuidied a reliability of the EML fit with MC data sets in Chapter 4. We scanned 6 points for each SDM paremeters in a proper range with all zeros for other parameters as listed in Table 4.4. In this chapter is shown SDM elements distributions depend on various SDM elements. From Figures G.1 to G.9 show the comparision between the input values and the output EML fit results in the GJ frame. From Figures G.10 to G.18 show the distributions in the helicity frame. The overlaid red lines show the exptected output value by EML fits. The reliability of the EML fit works well.

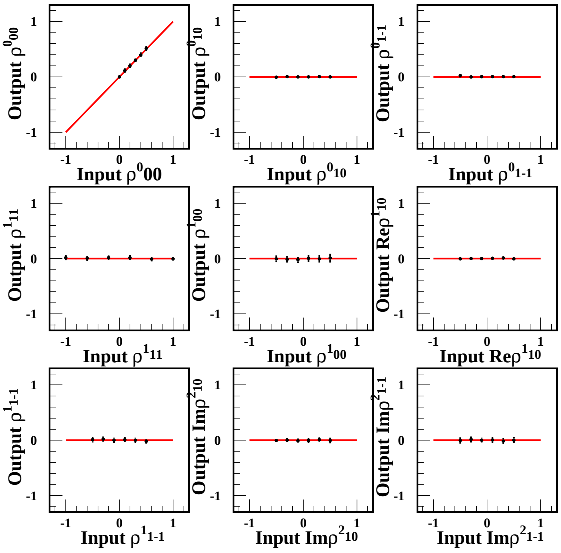

**Figure G.1:** Comparison with output SDM by EML fit and input SDM for the various $rho^0_{00}$ in GJ frame.

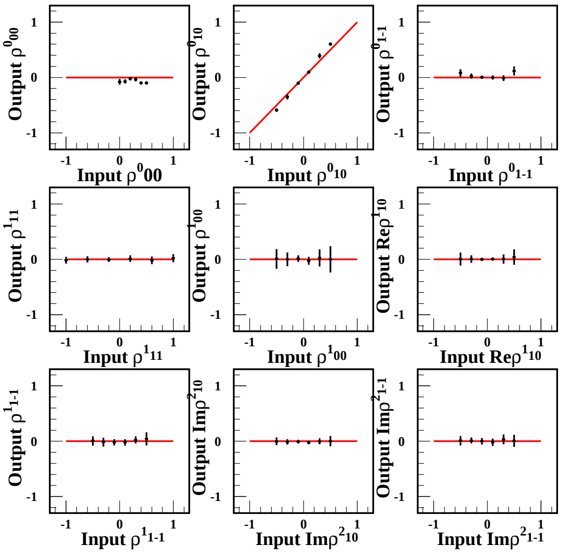

**Figure G.2:** Comparison with output SDM by EML fit and input SDM for the various $rho^0_{10}$ in GJ frame.

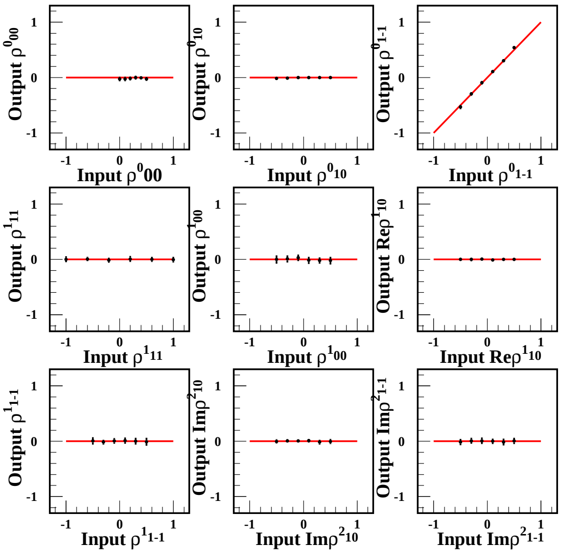

**Figure G.3:** Comparison with output SDM by EML fit and input SDM for the various $rho^0_{1-1}$ in GJ frame.

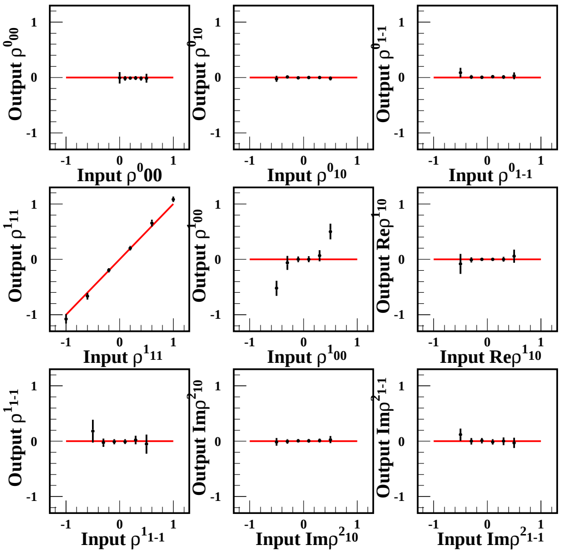

**Figure G.4:** Comparison with output SDM by EML fit and input SDM for the various $rho^1_{11}$ in GJ frame.

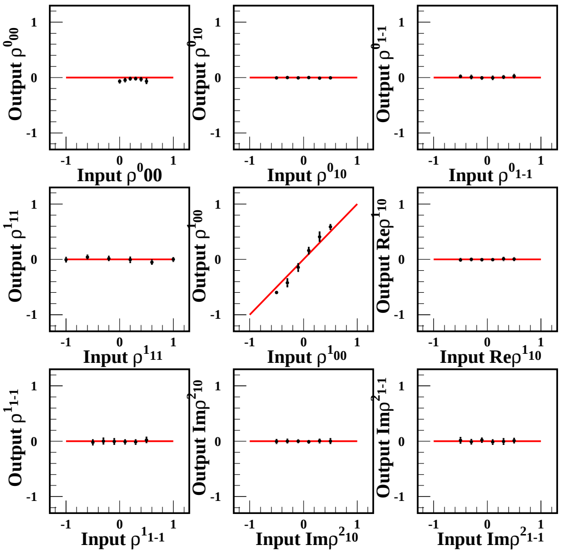

**Figure G.5:** Comparison with output SDM by EML fit and input SDM for the various $rho^1_{00}$ in GJ frame.

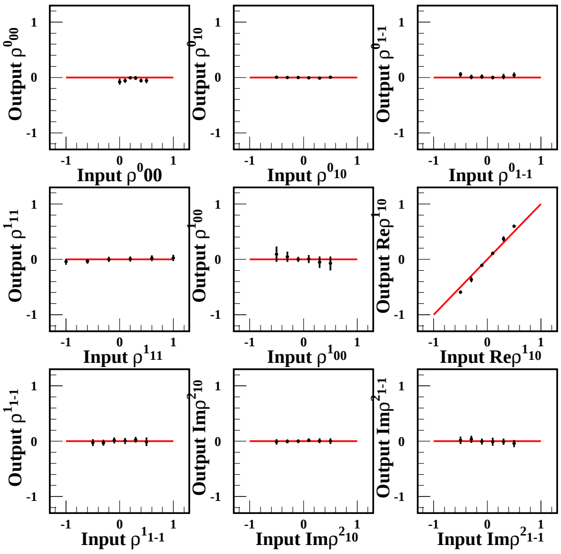

**Figure G.6:** Comparison with output SDM by EML fit and input SDM for the various $rho^1_{10}$ in GJ frame.

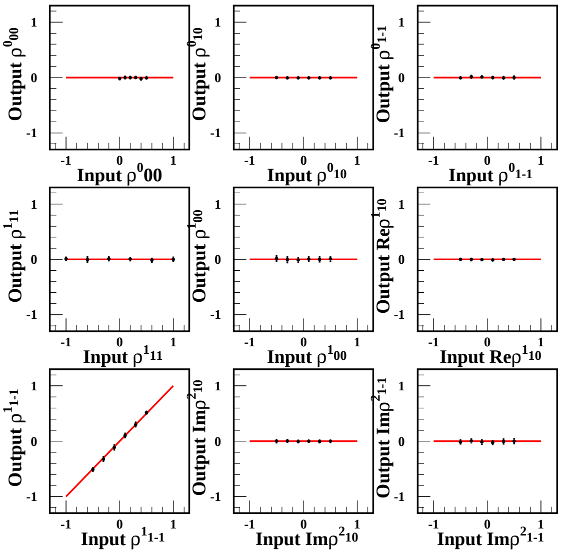

**Figure G.7:** Comparison with output SDM by EML fit and input SDM for the various $rho^1_{1-1}$ in GJ frame.

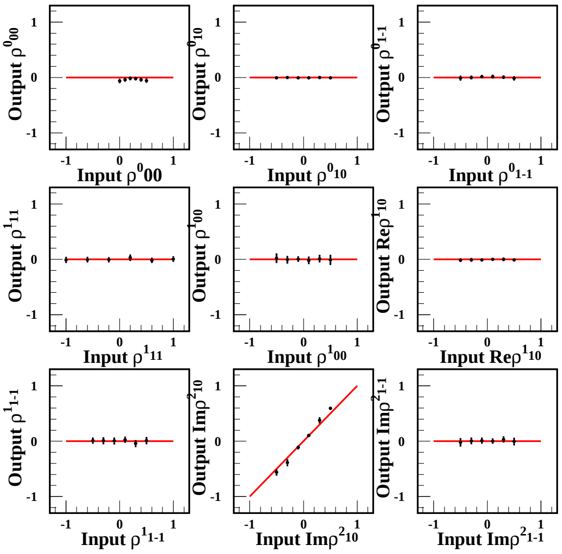

**Figure G.8:** Comparison with output SDM by EML fit and input SDM for the various $rho^2_{10}$ in GJ frame.

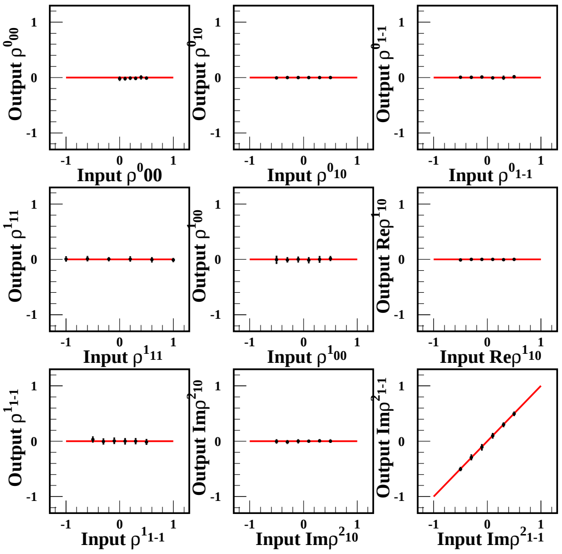

**Figure G.9:** Comparison with output SDM by EML fit and input SDM for the various $rho^2_{1-1}$ in GJ frame.

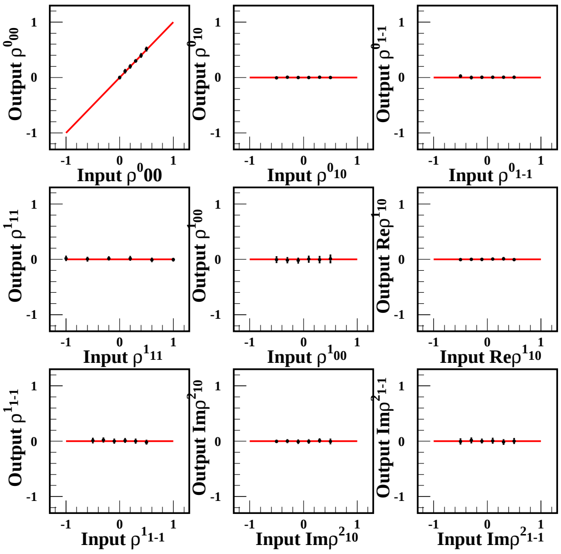

**Figure G.10:** Comparison with output SDM by EML fit and input SDM for the various $rho^0_{00}$ in helicity frame.

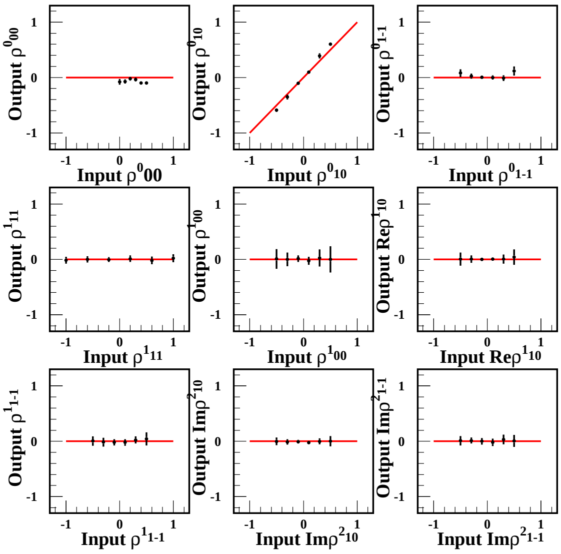

**Figure G.11:** Comparison with output SDM by EML fit and input SDM for the various $rho^0_{10}$ in helicity frame.

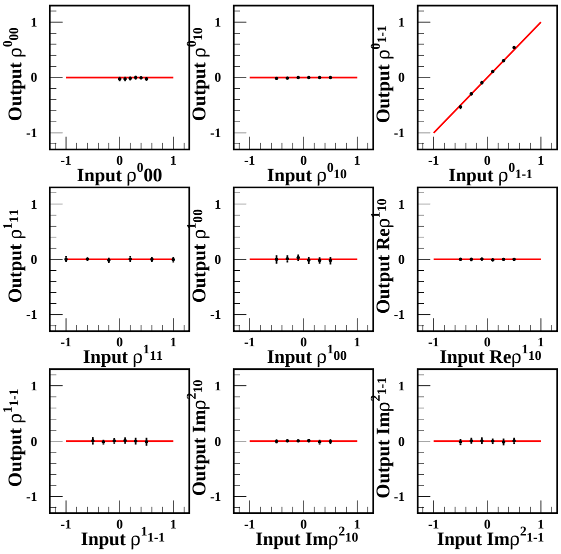

**Figure G.12:** Comparison with output SDM by EML fit and input SDM for the various $rho^{0}_{1-1}$ in helicity frame.

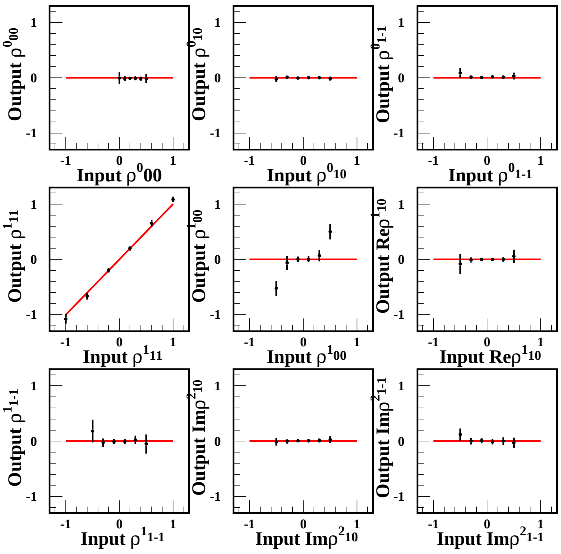

**Figure G.13:** Comparison with output SDM by EML fit and input SDM for the various $rho^{1}_{11}$ in helicity frame.

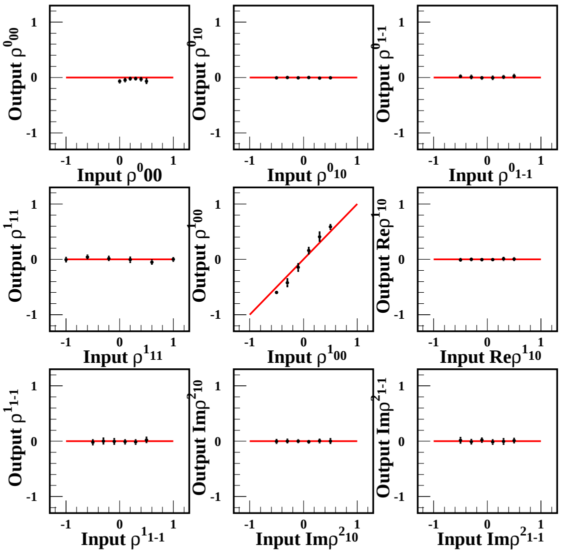

**Figure G.14:** Comparison with output SDM by EML fit and input SDM for the various $rho^1_{00}$ in helicity frame.

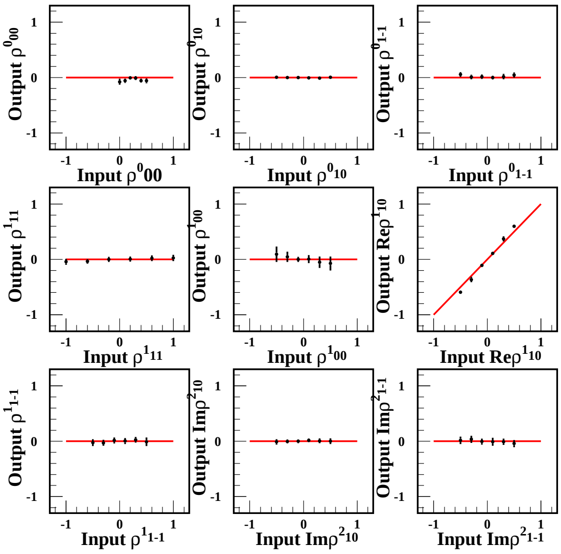

**Figure G.15:** Comparison with output SDM by EML fit and input SDM for the various $rho^1_{10}$ in helicity frame.

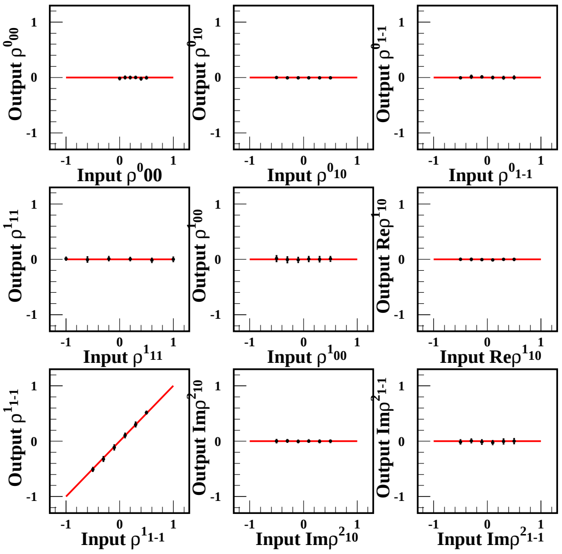

**Figure G.16:** Comparison with output SDM by EML fit and input SDM for the various $rho^1_{1-1}$ in helicity frame.

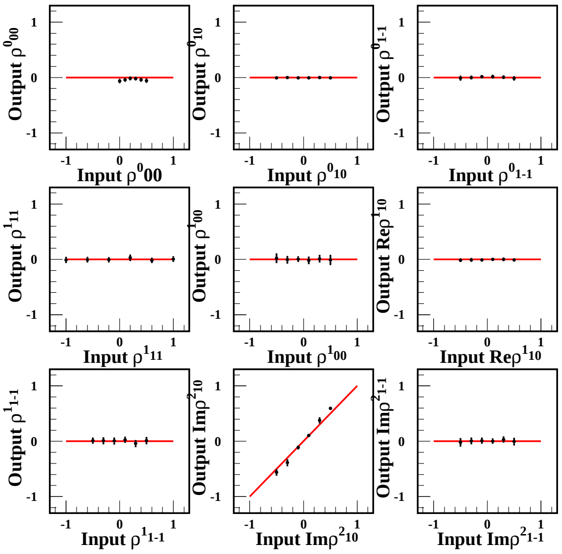

**Figure G.17:** Comparison with output SDM by EML fit and input SDM for the various $rho^2_{10}$ in helicity frame.

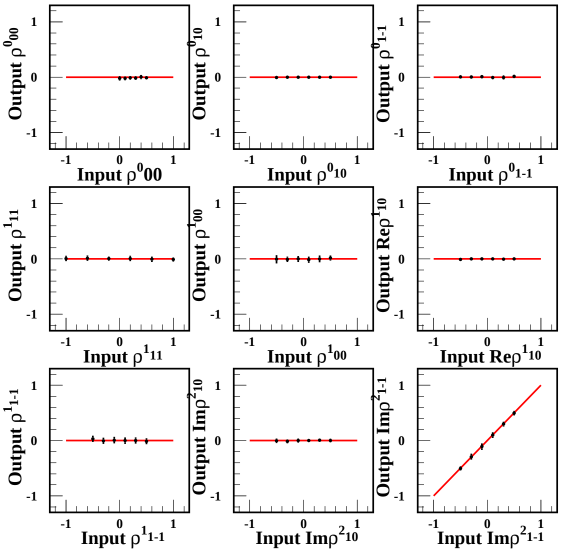

**Figure G.18:** Comparison with output SDM by EML fit and input SDM for the various $rho^2_{1-1}$ in helicity frame.

# Appendix H

# : Unbinned EML Fit Results without Side-Band Background Subtraction

We first extracted spin-density matrix elements using the unbinned EML fit without background subtraction as listed in Table H.1. A total of 726 $K^{*0}$ events are used for the EML fit, and the number of events from the fit $\bar{N}$ is found to be 725.99 ± 38.11, which is consistent with each other.

| $\hat{\rho}$ | Fitting results(GJ) | Fitting results(HE) |
|---|---|---|
| $\rho^0_{00}$ | 0.151± 0.034 | 0.091± 0.023 |
| $\rho^0_{10}$ | 0.114± 0.018 | -0.035± 0.020 |
| $\rho^0_{1-1}$ | 0.075± 0.032 | 0.037± 0.036 |
| $\rho^1_{11}$ | 0.043± 0.044 | -0.009± 0.045 |
| $\rho^1_{00}$ | -0.124± 0.057 | -0.028± 0.041 |
| $\rho^1_{10}$ | -0.097± 0.030 | -0.001± 0.031 |
| $\rho^1_{1-1}$ | 0.292± 0.049 | 0.349± 0.053 |
| $\rho^2_{10}$ | 0.122± 0.034 | -0.026± 0.031 |
| $\rho^2_{1-1}$ | -0.321± 0.046 | -0.371± 0.047 |
| $\bar{N}$ | 725.99± 38.11 | 726.01± 38.11 |
| $P_\sigma$ | 0.707 ± 0.113 | 0.725 ± 0.114 |

**Table H.1:** Spin density matrix elements by fitting results for Gottfried-Jackson frame and helicity frame.

The parity spin asymmetry is defined as

$$P_\sigma \quad = \quad 2\rho^1_{1-1} - \rho^1_{00}.$$

Given $\rho^1_{1-1}$=0.292 $\pm$ 0.049 (0.349 $\pm$ 0.053) and $\rho^1_{00}$=$-$0.124 $\pm$ 0.057 ($-$0.028 $\pm$ 0.041), the parity spin asymmetry $P_\sigma$ is estimated to be 0.71 $\pm$ 0.11 (0.73 $\pm$ 0.11) in GJ frame(helicity frame). Such a large positive value supports that a natural-parity exchange is dominant in forward angles for $K^{*0}\Sigma^+$ photoproduction from threshold to 3 GeV.

With estimated SDM elements we generated high-statistics simulation data to test if the EML fit results reproduce real data well. Figure H.1 shows a bunch of distributions for various kinematic variables such as momentum transfer squared $t$, incident photon energy $E_\gamma$, and momentum distributions for $K^*0$, $K^+$ and $\pi^-$. Left ones are for vertical polarization and right ones for horizontal polarization, respectively.

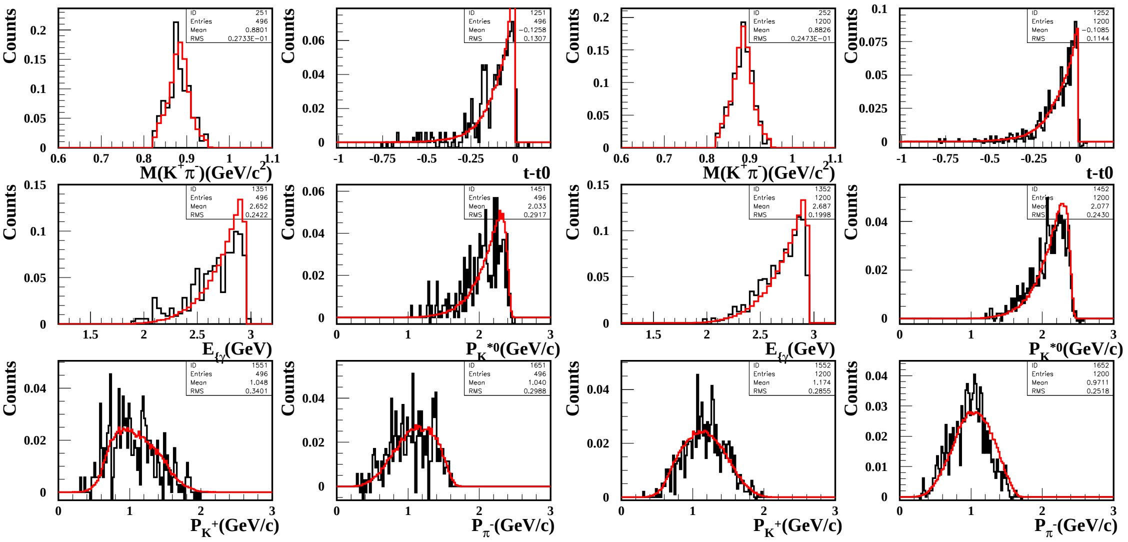

**Figure H.1:** Comparison of kinematic variable with Monte-Carlo(read) and real data(black). Left is vertical polarization and right is horizontal polarization, respectively.

We also estimated the SDM elements by a $\chi^2$-method with decay angular distributions for $\cos\theta$, $\phi_{K^+}$,$(\phi-\Phi)_{K^+}$, $\Phi_{K^+}$, $(\phi+\Phi)_{K^+}$, and $(\phi+\Phi)_{K^+}$ after acceptance correction. Figure H.2 shows acceptance distribution for five decay angular distributions by EML fitting result.After acceptance correction for five angular distribution are shown in Figure H.3.

The normalized decay angular distributions are fitted with the functions as represented in Section 6. Normalization factors are given by

$$A(x) = \sum_{i=1}^{N_{bin}} n_i(x)/N_{bin},$$

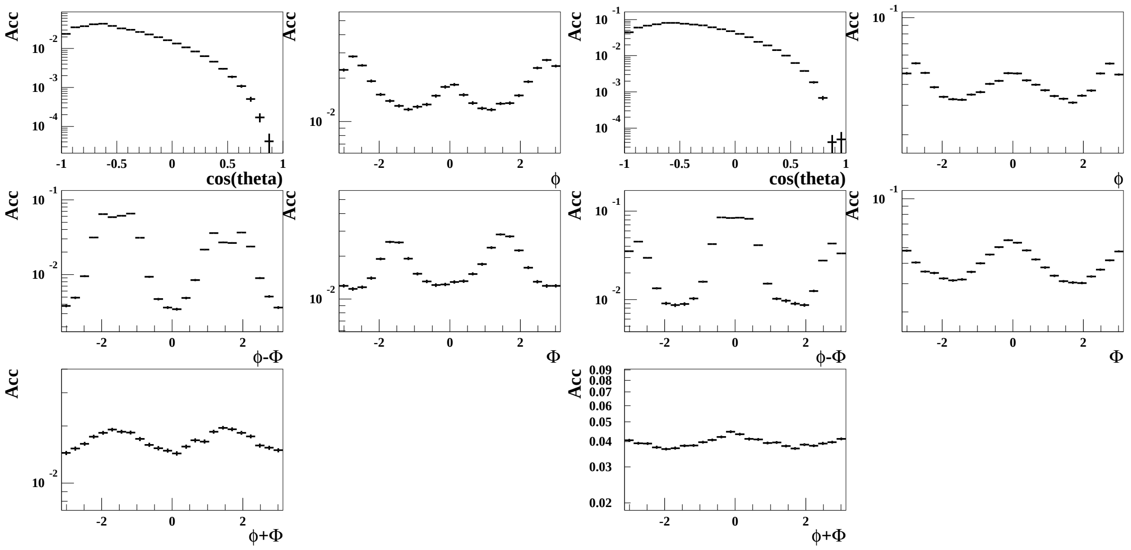

**Figure H.2:** Acceptance distribution for vertical polarization(left) and horizontal polarization(right).

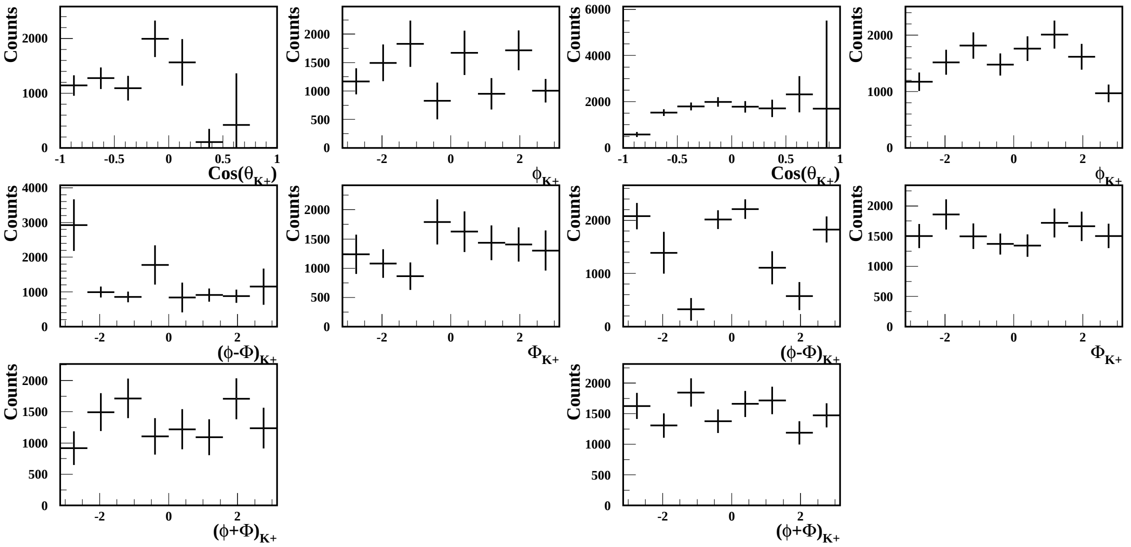

**Figure H.3:** The decay angular distribution of $\cos\theta_{K+}$, $\phi_{K+}$, $(\phi-\Phi)_{K+}$, $\Phi_{K+}$ and $(\phi+\Phi)_{K+}$ with acceptance correction. Left figure shows vertical polarization and right figure shows horizontal polarization, respectively.

where $x$ are the angle variables such as $\cos\theta_{K+}$, $\phi_{K+}$, $(\phi-\Phi)_{K+}$, $\Phi_{K+}$ and $(\phi+\Phi)_{K+}$. $n_i$ denotes the number of events in the $i^{th}$ bin. We estimated the SDM elements with different bin sizes yielding 6, 8, and 12 angular bins for each distribution. Figure H.4 shows the normalized decay angular distributions for horizontal and vertical polarization. Overlaid red-color lines show the fit results and the fit results are summarized in Table H.2.

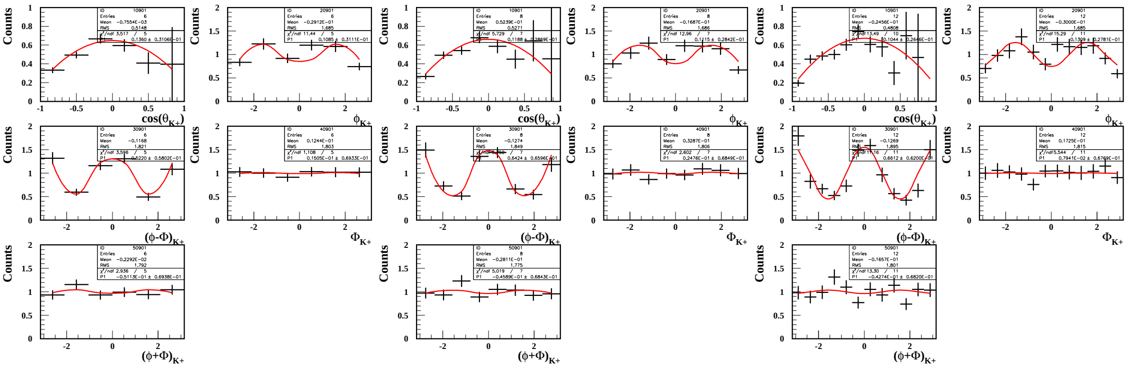

**Figure H.4:** The normalized decay angular distributions $\cos\theta_{K+}$, $\phi_{K+}$, $(\phi - \Phi)_{K+}$, $\Phi_{K+}$, and $(\phi + \Phi)_{K+}$ with 6 binning(left), 8 binning(middle) and 12 binning(right). Overlaid red lines show the fit results.

| $\hat{\rho}_{\mathrm{s}}$ | Unbinned EML fit | $\chi^2$-fit(6bin) | $\chi^2/ndf$ |
|---|---|---|---|
| $\rho^0_{00}$ | 0.151 ± 0.034 | 0.136 ± 0.31 | 3.52/5 |
| $Re\rho^0_{1-1}$ | 0.075 ± 0.032 | 0.109 ± 0.031 | 11.44/5 |
| $\rho^1_{1-1} - Im\rho^2_{1-1}$ | 0.613 ± 0.067 | 0.622 ± 0.058 | 3.60/5 |
| $2\rho^1_{11} + \rho^1_{00}$ | -0.038 ± 0.105 | 0.015 ± 0.069 | 1.11/5 |
| $\rho^1_{1-1} + Im\rho^2_{1-1}$ | -0.030 ± 0.067 | -0.051 ± 0.069 | 2.94/5 |
|  |  | $\chi^2$-fit(8bin) | $\chi^2/ndf$ |
| $\rho^0_{00}$ |  | 0.119 ± 0.029 | 5.73/7 |
| $Re\rho^0_{1-1}$ |  | 0.112 ± 0.028 | 12.96/7 |
| $\rho^1_{1-1} - Im\rho^2_{1-1}$ |  | 0.642 ± 0.066 | 5.75/7 |
| $2\rho^1_{11} + \rho^1_{00}$ |  | 0.025 ± 0.068 | 2.60/7 |
| $\rho^1_{1-1} + Im\rho^2_{1-1}$ |  | -0.046 ± 0.068 | 5.02/7 |
|  |  | $\chi^2$-fit(12bin) | $\chi^2/ndf$ |
| $\rho^0_{00}$ |  | 0.104 ± 0.026 | 13.49/10 |
| $Re\rho^0_{1-1}$ |  | 0.140 ± 0.028 | 15.29/11 |
| $\rho^1_{1-1} - Im\rho^2_{1-1}$ |  | 0.661 ± 0.062 | 17.16/11 |
| $2\rho^1_{11} + \rho^1_{00}$ |  | 0.008 ± 0.068 | 5.54/11 |
| $\rho^1_{1-1} + Im\rho^2_{1-1}$ |  | -0.043 ± 0.068 | 13.30/11 |

**Table H.2:** Comparison between spin density matrix elements estimated from the unbinned EML fit and from the $\chi^2$ fit without side-band subtraction.

# List of Figures

# List of Tables

# 선형 편광된 $E_\gamma$ = 1.85 - 3.0 GeV 을 이용한 전방 산란된 $K^{*0}\Sigma^+$ 광생성 연구

황상훈

부산대학교 대학원, 물리학과

## 요약문

쿼크 모델에서 meson은 SU(3) group(octet + singlet)로 잘 알려져 있다. 가벼운 meson의 경우 strange quark가 없는 4개와 strange quark를 가지는 4개의 쿼크로 구성되어 있다. 그러나 높은 질량의 meson은 quantum number의 정의가 잘 되어 있지 않다. 이중 scalar meson은 PDG(Particle Data Group)에서 “a long-standing puzzle”을 이야기 하며 아직까지 그 존재는 예측되지만 확인되지 않았다. 특히 scalar meson의 구성요소인 kappa(κ)는 질량이 800 MeV이고 반치폭은 질량의 절반으로 아직까지 그 존재가 확실치 않다. 최근 CLAS와 CBELSA/TAPS 그룹에서 K*0Σ+ 광생성에 대한 total cross section과 differential cross section data를 보고하였다. 두 그룹의 데이터는 전방방향으로 산란이 주로 일어나는 t-채널 생성이 높은 것으로 보고되었다. t-채널에서 교환 가능한 입자는 unnatural parity exchange인 슈도스칼라메존 Kaon과 natural parity exchange인 스칼라메존 κ이다. 이론 계산에서는 parity spin asymmetry()을 계산하였다. 특히 전방방향의 parity spin asymmetry를 측정에서 κ이 교환입자일 경우 +의 값을 가지고 Kaon이 교환입자일 경우 (-) 값을 가지게 된다. 본 연구에서는 SPring-8 가속기의 LEPS 검출기를 이용하여 최대 3.0 GeV의 선형 편광된 감마선을 이용하여 K*0Σ+광생성을 연구하였다. spin-density matrix elements를 unbinned Extended Maximum likelihood fit으로 Gottfried-Jackson 좌표계와 helicity 좌표계에서 구하였다. 이를 이용해서 구한 parity spin asymmetry 값은 (+)값을 보인다. 이는 natural parity exchange가 전방방향 산란에 대해서 주된 반응임을 나타낸다. 이 결과는 κ-meson의 존재를 확인할 수 있는 최초의 실험이며 낮은 질량의 scalar meson octet을 완성할 수 있는 중요한 결과이다.

# Acknowledgment

Thank you